

**Assessing linkages between ice sheet calving,
subpolar gyre hydrography and deep water
ventilation during the last glaciation**

by

Sunniva Rutledal



Master thesis in geology

Department of Earth Science

University of Bergen

June 2017

ABSTRACT

It is commonly postulated that ice sheet dynamics and freshwater perturbations in the North Atlantic were linked to disruptions in deep water circulation and North Atlantic cooling in the past. However, the exact nature of climate-ocean-ice sheet coupling remains unclear and increased iceberg activity and freshwater pulses have been hypothesized as both the trigger for, and response to, reduced Atlantic Meridional Overturning Circulation (AMOC). Differentiating between these hypotheses requires high-resolution records constraining the relative timing of ice sheet calving, freshwater perturbations and ocean circulation changes.

Here I assess the relative timing and linkages between iceberg discharge, subpolar gyre hydrography, and deep water ventilation in the North Atlantic using proxy records co-registered in the same sediment sequence. High-resolution ice rafted debris (IRD) and stable isotope ($\delta^{18}\text{O}$ and $\delta^{13}\text{C}$) records of planktonic (*N. pachyderma* (s)) and benthonic (*C. wuellerstorfi*) foraminifera were generated in sediment core GS15-196-02GC from the Irminger basin (59°37.1 N, 40°44.25 W, 2468 m water depth). The records document a clear coupling between increasing iceberg influence (IRD), decreasing deep water ventilation (benthonic $\delta^{13}\text{C}$), and temperature and salinity changes in the subpolar gyre surface waters (planktonic $\delta^{18}\text{O}$). The largest IRD peaks are coincident with low planktonic $\delta^{18}\text{O}$ anomalies and are associated in time with Heinrich events 1-3. However, low magnetic susceptibility, low Ca/Sr (detrital carbonate), and increases in Si/Sr (detrital silicate) indicate that the IRD layers associated with H1-H3 do not have the properties of typical Hudson Strait/Laurentide Ice sheet (LIS) sourced material; implying that other ice sheets were also active at these times. The proximity of the core to southeast Greenland and the East Greenland Current (EGC) points towards an IRD origin from east Greenland or other circum-Nordic Seas sources.

The benthonic (*C. wuellerstorfi*) $\delta^{13}\text{C}$ record documents high magnitude variability in deep ocean ventilation throughout the last glacial and deglacial periods. Intervals of peak subpolar gyre freshening (planktonic $\delta^{18}\text{O}$ minima) were preceded by 'precursor' increases in iceberg discharge and decreases in deep water ventilation (benthonic $\delta^{13}\text{C}$). These 'precursors' were initiated 500-2000 years prior to the H2 and H3 related freshening, supporting the hypothesis that reduced AMOC was important for triggering ice shelf melting/collapse during Heinrich events. However, the periods of weakest ventilation (low benthonic $\delta^{13}\text{C}$) still coincide with the largest IRD peaks and planktonic $\delta^{18}\text{O}$ decreases, consistent with a feedback of ice sheet collapse and subpolar freshening on deep water circulation. Finally, there is preliminary evidence that circum-Nordic Seas iceberg calving may also have increased during smaller (non-Heinrich) Dansgaard-Oeschger stadials. Taken together, the results point toward a two-way coupling between ocean circulation and ice sheets during millennial scale climate changes and highlight the systematic involvement, and potential sensitivity, of the circum-Nordic Seas cryosphere-ocean system.

Acknowledgements

First I would like to thank my supervisor Dr. Ulysses S. Ninnemann for his excellent guidance and for giving me the opportunity to work on such an inspiring project. I would also like to thank my co-supervisors, Dr. Helga (Kikki) F. Kleiven for her guidance and very useful comments during the writing process and Dr. Nil Irvani for her assistance and patience with me during the sediment and foraminifera sampling process. I also want to thank Rune Sørås at FARLAB, UoB, for assistance in using the mass spectrometer, and Dr. Haflidi Haflidason and Dr. Eivind W. N. Støren at EARTHLAB, UoB, for guidance in using the MST and ITRAX core scanner.

I am grateful to my supervisors for giving me the opportunity to travel to Vienna and attend the EGU2017 conference in April, where I got to present my work and receive feedback from a broad scientific audience. Thank you to Frida for making the stay in Vienna the best it could be.

I would also like to thank my fellow students at the Department of Earth Science for five amazing years. To my friends at “Hovedkvarteret”, Tone, Hege and Helene, thank you for all the cheerful lunch breaks and much more. Thank you to Marie, Cecilie and Annette for being supportive friends, and especially to Sunniva Samdal for proofreading and commenting on parts of this thesis.

Special thanks to my parents for emotional and economical support, and to my father for commenting and giving feedback on parts of this thesis.

Finally, the greatest thank you to Herman, for filling my life with joy and happiness, and for supporting me during stressful times.

We made it!

June 2017
Sunniva Rutledal

TABLE OF CONTENTS

Abstract	
Acknowledgements	
1. INTRODUCTION	1
1.1 The SNACS Project	1
1.2 Objective	1
2. BACKGROUND	4
2.1 The Climate System	5
2.2 Climate variability	5
2.3 The Thermohaline Circulation	9
2.3.1 Past ocean circulation changes	11
2.3.2 Future projections	13
3. STUDY AREA	15
3.1 Bathymetry	16
3.2 Oceanography	17
3.2.1 Surface circulation	18
3.2.2 Deep ocean circulation	22
3.3 Contourites	27
3.3.1 The Eirik Sediment Drift	27
4. MATERIAL AND METHODS	29
4.1 Core GS15-196-02GC	29
4.2 Laboratory methods	29
4.2.1 Multi-sensor-track (MST)	29
4.2.2 X-Ray Fluorescence (XRF) analysis	30
4.2.3 Sampling	31
4.2.4 Smear slides	31
4.2.5 Picking foraminifera and counting Ice rafted debris (IRD)	32
4.2.6 Preparation for stable isotope analysis	32
4.3 Mass spectrometry	33
4.3.1 Standards	35
4.4 Climate proxies	36
4.4.1 Stable isotopes	36

4.4.2 Ice rafted debris.....	42
4.5 Foraminifera.....	44
4.5.1 Planktonic foraminifera.....	45
4.5.2 Benthonic foraminifera	47
5. CHRONOLOGY	50
5.1 Dating method.....	50
5.1.1 AMS Radiocarbon ¹⁴ C dating	50
5.2 Age model.....	52
5.2.1 Reservoir ages in the North Atlantic.....	53
6. RESULTS	55
6.1 Core description, magnetic susceptibility and XRF-results.....	55
6.2 Ice Rafted Debris (IRD).....	57
6.3 Oxygen isotope results.....	59
6.3.1 Near-surface water (planktonics)	60
6.3.2 Deep water (benthonic).....	62
6.3.3 Planktonic $\delta^{18}\text{O}$ vs. Benthonic $\delta^{18}\text{O}$	65
6.4 Carbon isotope results.....	66
6.4.1 Near-surface water (planktonic).....	66
6.4.2 Deep water (benthonic).....	68
7. DISCUSSION	71
7.1 Near-surface water properties.....	72
7.1.1 Ice rafted debris events	72
7.1.2 Low planktonic $\delta^{18}\text{O}$ anomalies.....	76
7.2 Deep water mass geometry in the North Atlantic during the last glaciation	80
7.3 Timing of ice sheet calving, freshwater perturbations and ocean circulation.....	84
7.3.1 Perspective on North Atlantic climate oscillations during the last glaciation	88
7.4 Summary of conclusions.....	90
REFERENCES	92
Appendix	

1. INTRODUCTION

This thesis has been supervised by Professor Dr. Ulysses S. Ninnemann, Associate Professor Dr. Helga (Kikki) F. Kleiven and Researcher Dr. Nil Irvah from the Department of Earth Science and Bjerknes Centre for Climate Research (BCCR) at the University of Bergen (UoB).

1.1 The SNACS Project

This thesis is a contribution to the SNACS (Subpolar North Atlantic Climate States) project. The SNACS project is funded by the Norwegian Research Council and led by Associate Professor Dr. Are Olsen, UoB and BCCR. The project aims to determine the impacts of climate on the hydrography, biogeochemistry and carbon cycling on multiple timescales (from the last glacial to the present) in the Subpolar North Atlantic (SPNA). The primary focus is on the ocean basins southwest of Iceland; the Irminger and Labrador basins, as well as the subpolar gyre. This is an area where Nordic Sea overflows join deep water from the Labrador Sea and continue as the Deep Western Boundary Current (DWBC), forming the deeper limb of the Thermohaline Circulation (THC). Hence, variability in this area will affect several processes, such as heat – and carbon fluxes and the strength of overturning.

Using high-resolution sediment archives that provide information about the near-surface and deep water properties, the project aims to establish the variability of the SPNA region spanning from the last glacial to the present. Obtaining the past behaviour of this important region will generate increased knowledge about the effect of future climate change induced by increased CO₂ emissions.

1.2 Objective

The objective of this thesis is to test the hypothesis that climate and ocean circulation are coupled to variability in ice sheet dynamics (e.g. Greenland Ice Sheet (GIS)) and freshwater fluxes. This is achieved with a multi-proxy approach, comparing benthonic and planktonic stable oxygen ($\delta^{18}\text{O}$) and carbon ($\delta^{13}\text{C}$) records to ice rafted debris records from the same sediment sequence.

In addition, the original objective was to characterize the natural variability of climate, ocean circulation and ice sheet behaviour through the Holocene to provide a baseline of natural variability against which current trends could be evaluated (e.g. to test if recent changes are

comparable to those periods in the past when North Atlantic Deep Water (NADW) was strongly reduced). However, after radiocarbon dating, the core turned out to be substantially older than the Holocene epoch (11.7ka - today (Cohen et al., 2013)), extending into the last glaciation and subsequent deglaciation (approximately 5 ka-35 ka). Hence, the focus had to be shifted from an interglacial climate state to a glacial climate state. This provided an opportunity to investigate how large freshwater perturbations in the past (e.g. Heinrich events) are coupled with changes in deep water circulation in the Irminger Sea, and offers novel constraints on different hypotheses regarding the stability of marine terminating ice sheets and their influence on, and by, deep water circulation. Ultimately, this knowledge is timely and relevant to better understand the potential future instability of marine terminating glaciers, and their impacts, in response to continued climate change.

The material for the study is provided by a 334.5 cm long sediment gravity core (GS15-196-02GC, 59°37.1 N, 40°44.25 W, 2468 m water depth) from the Eirik sediment drift retrieved onboard R/V *G. O. Sars* during the SNACS cruise in April 2015. The Eirik sediment drift is an ideal study site due to its generally high-accumulation rates, providing high-resolution records. The site is also ideal when reconstructing ice sheet, climate and ocean variability due to its proximity to the Greenland Ice Sheet and ambient ocean currents such as the East Greenland Current (EGC), Irminger Current (IC) and Denmark Strait Overflow Water (DSOW).

The overall objective of the thesis is to establish an understanding of the coupling between ice sheet calving (IRD), freshwater input ($\delta^{18}\text{O}$) and deep water ventilation ($\delta^{13}\text{C}$) in the Irminger Basin during millennial scale climate change (e.g. Heinrich events and D-O cycles).

Specifically, the thesis aims to answer the following scientific questions:

- Was circum-North Atlantic ice sheet calving synchronous or non-synchronous during large climatic events (e.g. Heinrich events)? Are there “precursor” calving events to Heinrich events and what impact might they have as a possible trigger for Heinrich events?
- Was deep water ventilation in the Irminger Basin reduced during climatic cold events (e.g. Heinrich events and D-O stadials)? Which poorly ventilated water mass replaced well ventilated northern sourced water?

- What was the timing of reduced Atlantic Meridional Overturning Circulation (AMOC), iceberg activity, and freshwater perturbations during H-events and D-O stadials? Was reduced AMOC a response to, or trigger for, increased iceberg activity and freshwater perturbations?

2. BACKGROUND

The global climate is constantly changing and is projected to continue to change in the future, largely due to human activities. The nature of human-induced climate change depends mainly on the increased level of greenhouse gases (GHG) in the atmosphere associated with the burning of fossil fuels, and the Earth's climate system response to increasing GHG levels. Responses may include shrinking glaciers and ice sheets, a rise in the global sea level, increasing global temperatures, changes in precipitation patterns, warming of the global ocean and changes in ocean circulation patterns (IPCC, 2013). In the global ocean circulation system, the THC and the AMOC are projected to be largely influenced by the changing climate. However, uncertainties follow these future projections and improved knowledge about the ocean circulation response to future climate change remains crucial. According to the IPCC fifth assessment report it is *very likely* that the AMOC will weaken during the 21st century, although, abrupt collapse remains *very unlikely* (Rhein et al., 2013). The most probable trigger for a reduction of the AMOC is freshening of the North Atlantic due to increased rainfall and melting of large continental ice sheets (e.g. the Greenland Ice Sheet), which decrease the density of the surface waters and inhibit sinking and formation of deep water. In addition, the global ocean is getting warmer and will continue to do so during the 21st century (IPCC, 2013), further reducing the surface water density and the AMOC.

The GIS is the second largest body of ice in the world, and is in volume equivalent to a 7.3 m global sea level rise (Cronin, 2010). Recent studies of the GIS mass balance budget show that the GIS currently is melting, and suggests an accelerated melt rate over the last decades (Rignot et al., 2011; Schrama and Wouters, 2011). If this trend continues, enhanced freshwater fluxes from Greenland to the surface ocean could cause a substantial reduction in the AMOC. Hence, understanding the possible effect of GIS melting (and ice sheet melting in general) on deep water circulation patterns is essential. One way to increase knowledge about this future aspect is to study events of freshwater perturbations in the past. Several such events can be found during the last glaciation and subsequent deglaciation and have shown to greatly affect the THC (e.g. (Heinrich, 1988; Bond et al., 1992; Broecker et al., 1992)). In this thesis, I will investigate the relationship between ice sheet melting, near-surface water properties (changes in temperature and salinity) and deep water ventilation over the past glacial and deglacial period (5 ka-35 ka).

2.1 The Climate System

The Earth's climate system consists of five interacting components: the atmosphere, hydrosphere, cryosphere, biosphere and the land surface. Several factors cause and drive changes in the climate system, on longer, and shorter timescales. These factors are often referred to as *forcings* and the resulting change as *responses*. Three main types of climatic forcing exist; tectonic processes, changes in the Earth's orbit around the sun and changes in the strength of the sun. Anthropogenic climate forcing, caused by human rather than natural factors, is viewed as a fourth contributor. A change in one or more of the *forcings* will induce a change in the interaction between the different components in the system. Such interactions within the system may then bring positive or negative feedbacks. Positive feedbacks are processes that amplify the initial change, while negative feedbacks suppress the initial change (Ruddiman, 2014). Hence, a change in an external factor such as the strength of the sun, will cause a range of different responses (at different rates) among the various internal components of the climate system. These responses will further perturb the Earth's climate through positive and negative feedbacks.

The components of the climate system constantly interact with each other, at different timescales. They hold different response times and changes may be annual, seasonal or take thousands to billions of years. The atmosphere is the fastest responder (hours to weeks), while the deep ocean and ice sheets are slower responders and may lag 100 - 10.000 years behind the initial climatic forcing (Ruddiman, 2014).

2.2 Climate variability

The Quaternary geological time period (2.58 Ma - today) (Cohen et al., 2013) includes the Pleistocene (2.58 Ma - 11.7 ka ago) and Holocene (11.7 ka ago - today) epochs (Cohen et al., 2013). This period is associated with cyclic growth and decay of continental ice sheets in the Northern Hemisphere and is related to Milankovitch's orbital forcing; 23,000 year cyclic changes in the precession of the solstices and equinoxes (the position of Earth's rotational axis), 41,000 year cyclic changes in the obliquity (the angle of the tilt of Earth's rotational axis) and 100,000 (413,000) year cyclic changes in the eccentricity (the shape of Earth's orbit) (Ruddiman, 2014). Based on Milankovitch's theory, Hays et al. (1976) proposed that ice sheets in the Northern Hemisphere grow when summer insolation is reduced, that is when the Earth's tilt is low, the orbit is greatly eccentric, and when northern summer solstices occur in the

aphelion, when the Earth is furthest from the Sun. Oxygen isotope records from North Atlantic sediment cores (Raymo, 1992) reveal a strong 41,000 year (obliquity) and 23,000 year (precession) signal in the early Quaternary, up until 900,000 years ago. While during the last 900,000 years, ice sheets have grown over longer time intervals, more consistent with the 100,000 years eccentricity cycle (Raymo, 1992; Berger and Jansen, 1994; Lisiecki and Raymo, 2005). However, variations in the eccentricity are not likely to have a significant effect on the insolation signal and are considered to be too small to produce the corresponding climate cycle observed (Imbrie et al., 1993). Hence, it has been suggested that eccentricity does not by itself promote the growth of large ice sheets and glaciations, but rather modulates the influence of precession and obliquity. Thus, at the time of low eccentricity, the influence of precession or obliquity is enhanced (Cronin, 2010). In addition, the Pleistocene epoch is characterized by abrupt millennial scale climate oscillations superimposed on the longer orbital-scale climate cycles. Such climate variability, when the climate switches rapidly and the change persists on centennial to millennial time scales, during a longer glacial period cannot be explained by orbital theory but rather by internal fluctuations within the climate system such as the interaction between the ocean and the atmosphere.

Dansgaard-Oeschger (D-O) events are several abrupt climatic events (first) observed in the Greenland ice cores (Dansgaard and Oeschger, 1989) during the last glacial period. Their onset is marked by a rapid transition to interstadial conditions (over only a few decades) with atmospheric warming (8-16°C) over Greenland (Figure 2.1). Warm conditions persist for 500-2500 years, followed by a gradual return to a colder, stadial state. In total, 25 D-O events have been identified in the last glacial period (115 ka-20 ka) (Dansgaard et al., 1993). Records from North Atlantic sediments have been correlated to the D-O events found in Greenland ice cores, revealing rapid changes in sea surface temperatures (SST), foraminifera assemblages, stable oxygen isotopes and ice rafted debris (IRD) in phase with the Greenland D-O events (Bond et al., 1993; McManus et al., 1994; Rasmussen et al., 1996; Chapman and Shackleton, 1998).

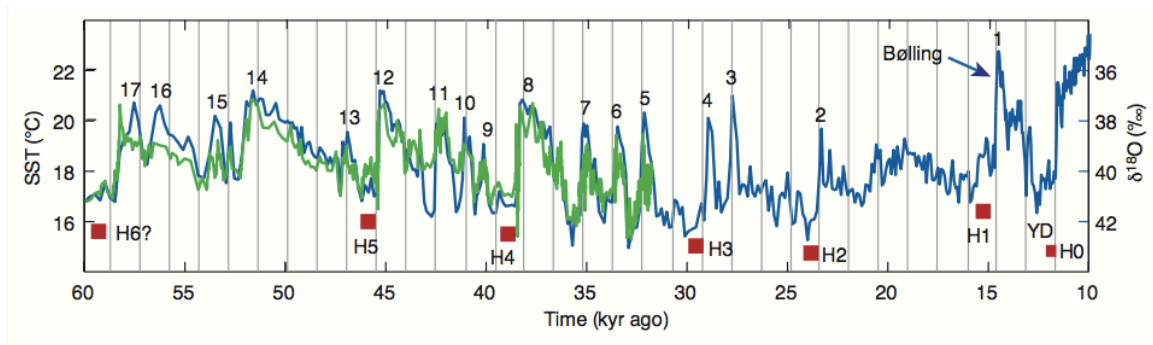


Figure 2.1: Temperature reconstructions from Greenland (GISP2, blue) and the subtropical Atlantic (green). Numbers denote Dansgaard-Oeschger warming events, while red boxes denote cold Heinrich-events over the last 10 ka – 60 ka (Grootes et al. (1993); Sachs and Lehman (1999); Bacon et al. (2002) in Rahmstorf (2002)).

During the last glacial period (115 ka-20 ka) there was little variability in the solar insolation at high latitudes. Thus, the rapid warming over Greenland during D-O events must be caused by something other than orbital variations/drivers. One clue to their origin resides in the close correlation of D-O cycles in the marine sediment cores and the Greenland Ice cores, which clearly show that the ocean surface (sediment cores) and atmosphere (ice cores) are a coupled system, at least for the last 80 ka (Bond et al., 1993), implying that ocean-atmospheric changes may be responsible for D-O events.

Related to some of the coldest periods (stadials) between the warm D-O events are six distinct events named Heinrich-events (H-events) (Heinrich, 1988; Bond et al., 1992; Broecker et al., 1992). H-events are believed to be related to massive iceberg discharges from the North American Laurentide Ice Sheet (LIS) through the Hudson Strait and into the North Atlantic (Broecker, 1994). In sediment cores, H-events are identified as 10-15 cm thick layers deposited across a wide belt (40°-55°N (Ruddiman, 1977)) on the ocean floor in the North Atlantic (Hemming, 2004). The cause of H-events is still debated and the explanations revolves around either internal ice sheet dynamics (e.g. binge/purge model by MacAyeal (1993)) or external climatic forcings (e.g. (Bond and Lotti, 1995; Marcott et al., 2011)). If caused by internal ice sheet dynamics, it is suggested that the continental ice sheets grew to a critical thickness, crossing an unknown threshold, becoming unstable and thereby releasing massive surges of ice into the ocean. If climatically induced, another possibility is that a sea level rise produced by the warming accompanying D-O events destabilized the ice shelves and released the iceberg armadas (Bond and Lotti, 1995). Alternatively, a weakening of the AMOC, will reduce the overturning and formation of deep water. A weaker AMOC will reduce the oceanic heat loss to

the atmosphere and heat will build up in the subsurface oceanic layers. Further, this subsurface warming may cause increased basal melting underneath ice shelves (Figure 2.2), triggering ice sheet collapse, as illustrated in Figure 2.3 (Marcott et al., 2011). Nevertheless, ice sheet collapse increase the freshwater input to the North Atlantic region, and reduce the surface water density and possibly inhibit deep water formation in the region, further weakening the AMOC (McManus et al., 1994).

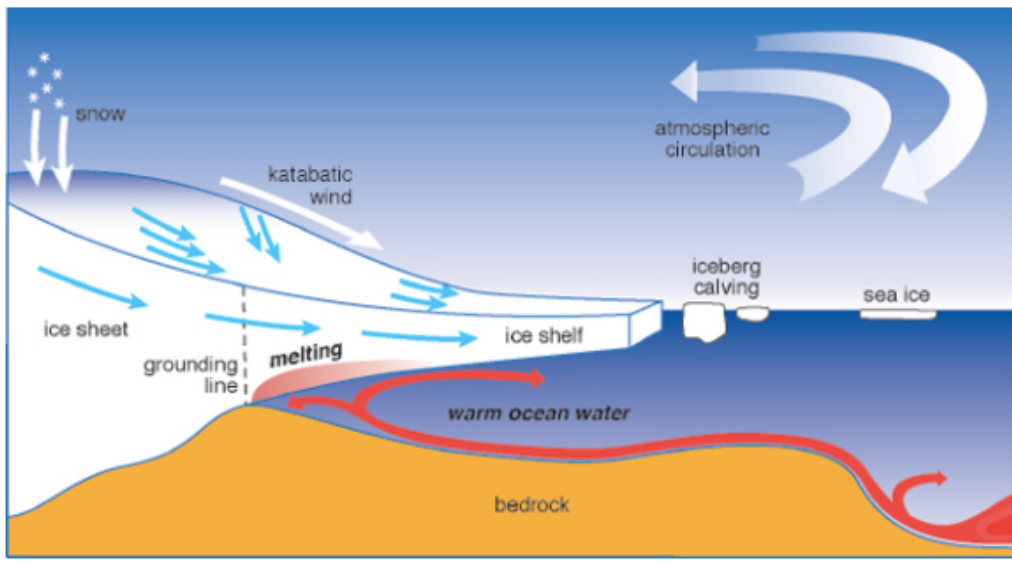


Figure 2.2: Schematic of the processes that affect an ice shelf. Warm water flowing underneath the ice shelf promotes increased basal melting and thinning of the ice shelf, causing increased release of icebergs. Additional processes are wind patterns and snow accumulation (National Academies of Sciences Engineering and Medicine, 2015).

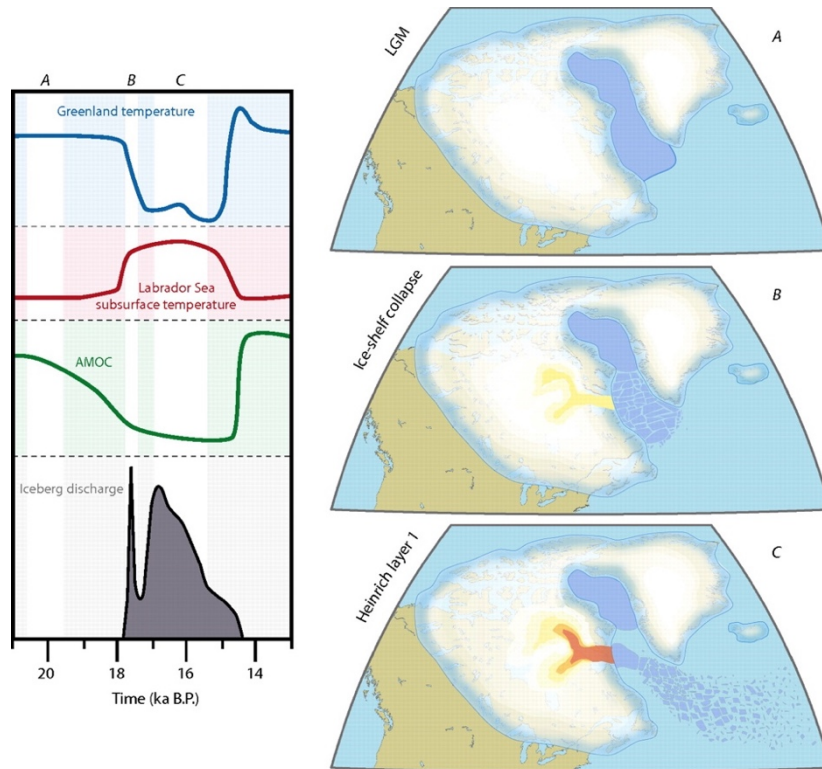


Figure 2.3: Schematic of one of the proposed triggering mechanisms for Heinrich event 1. On the left panel is the variability of the involved triggering mechanisms over time (from A to C). First AMOC starts to decrease (green curve), then the oceanic subsurface temperatures in the Labrador Sea increase (red curve), coinciding with the Greenland temperature (blue curve), and finally iceberg discharge increases (grey curve). On the right, time slice of the events A (LGM) to C (H1) are shown. White colours represent the Laurentide ice sheet, darker blue the ice shelves, yellow and red the thinning and acceleration of ice streams (Alvarez-Solas and Ramstein, 2011).

2.3 The Thermohaline Circulation

The global circulation pattern of ocean currents is divided into two types of flow according to the force that drive them; surface currents and subsurface (deep ocean) currents (Figure 2.4). Surface currents are wind-driven, while deep currents are density-driven, often called the thermohaline circulation (Pinet, 2013). The thermohaline circulation is driven by fluxes of heat (thermo) and freshwater (haline) across the ocean surface and mixing between the two. The THC consists of four main components, (1) deep water formation regions where water masses become dense enough to sink (on the globe this process only occurs in a few areas: The Nordic Seas, Labrador Sea (and partly the Irminger Sea), Mediterranean Sea, The Weddell Sea and the Ross Sea). (2) Spreading of deep water through deep boundary currents (e.g. DWBC). (3) Upwelling processes which transport water from the deep to the near surface ocean (upwelling of deep water is challenging to observe but it is believed to take place mainly in the Antarctic Circumpolar Current Region). (4) Near-surface currents that transport relatively low-density

water from low to high-latitudes and closing the loop (Kuhlbrodt et al., 2007). The four components cover the entire Atlantic Ocean in both hemispheres and forms a circulation system that includes two overturning cells: North Atlantic Deep Water and Antarctic Bottom Water (AABW), where the latter has the highest density. Related to the THC is the Meridional Overturning Circulation (MOC), that refers to the north-south flow in regards to latitude and depth, and unlike the THC, MOC includes wind-driven parts such as Ekman cells (Rahmstorf, 2006). The Atlantic component of the MOC (AMOC) is closely linked to the climate in the North Atlantic region.

The THC plays an important role in Earth's climate system and regulates several processes in the Atlantic Basin, such as the stratification and distribution of different water masses, the amount of heat transported by the ocean and the cycling and storage of chemical species (e.g. CO₂) (Kuhlbrodt et al., 2007). The heat and freshwater fluxes across the surface ocean are essential for deep water formation as they control the surface water density by cooling or warming and/or increasing and decreasing the salinity. Decreasing the density in key deep water formation regions in the North Atlantic creates a more stratified water column, inhibits deep convection and weakens the THC.

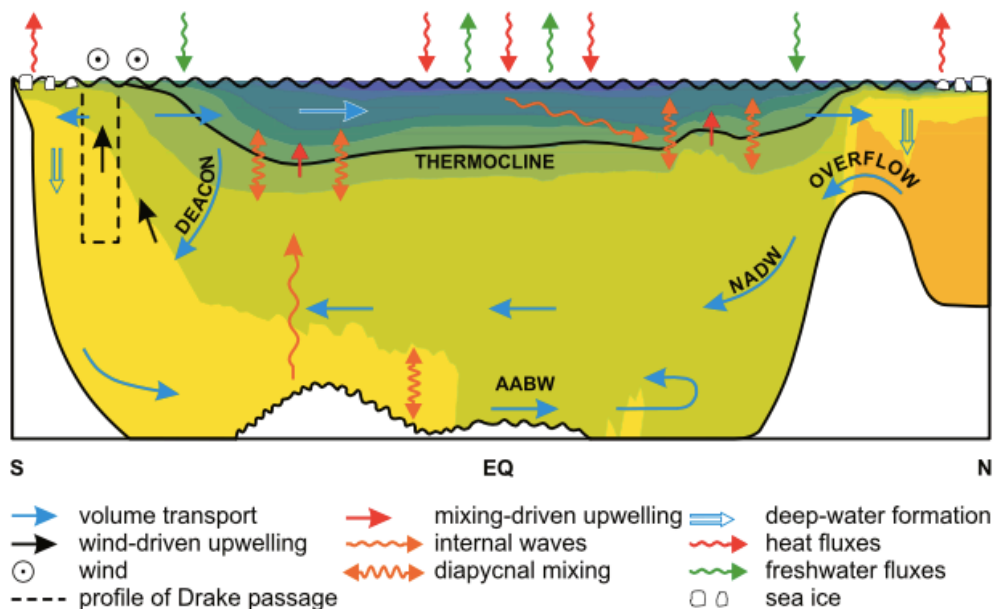


Figure 2.4: Circulation in the Atlantic Ocean. Straight arrows represent the MOC. Colour shading indicates observed density stratification: light waters in blue and heavy waters in orange. Wind driven upwelling is also displayed (Southern Ocean) - a result of the Ekman transport. NADW=North Atlantic Deep Water, AABW=Antarctic Bottom Water (Kuhlbrodt et al., 2007).

2.3.1 Past ocean circulation changes

Several studies have demonstrated the close link between millennial scale climate variability and the strength of the THC (e.g. (Keigwin and Lehman, 1994; McManus et al., 2004)). These studies connect changes in ocean circulation patterns to abrupt climate changes in the past, such as large temperature shifts in Greenland (D-O events) and iceberg surges (H-events) into the North Atlantic. Over the past 120,000 years, the ocean circulation system has undergone major changes and studies of Atlantic sediment cores reveal three distinct modes of Atlantic THC as defined by Rahmstorf (2002) (Figure 2.5): the interstadial (warm) mode, the stadial (cold) mode and the Heinrich (off) mode. This is currently the leading model to explain rapid climate variability observed in several paleoclimate archives (e.g. ice cores, marine sediment cores, speleothems). The switches between the different modes can be abrupt and are recorded in North Atlantic sediments (Bond et al., 1993). During the interstadial (warm) mode, NADW is formed in the Nordic Seas, as it is today. This mode has often been connected to D-O warming events. In the stadial (cold) mode, the site of NADW formation shifts to the south of Iceland, to the subpolar open North Atlantic. In this mode, NADW do not become as dense as during the interstadial mode, sinking to depths of less than 2500 m (Labeyrie et al., 1992), causing a reduction in the strength of the Atlantic THC and allowing for greater influence of Southern Ocean source water in the deep Atlantic basin. During Heinrich events, in the Heinrich (off) mode, NADW formation may have ceased and the deep Atlantic basin filled with Southern Ocean source waters to depths as shallow as 1000 m (Sarnthein et al., 1994). It has been suggested that this cessation, or at least a strong reduction of NADW formation, was induced by freshwater released from icebergs that decreased the surface water density in the North Atlantic region (Rahmstorf, 1995). Indeed, ocean model simulation runs suggest that the THC is sensitive to freshwater perturbations of 0.1 Sv ($1 \text{ Sv} = 10^6 \text{ m}^3 \text{ s}^{-1}$) (Stouffer et al., 2006). Hence, freshwater input in the North Atlantic is potentially of major importance regarding the strength of the THC.

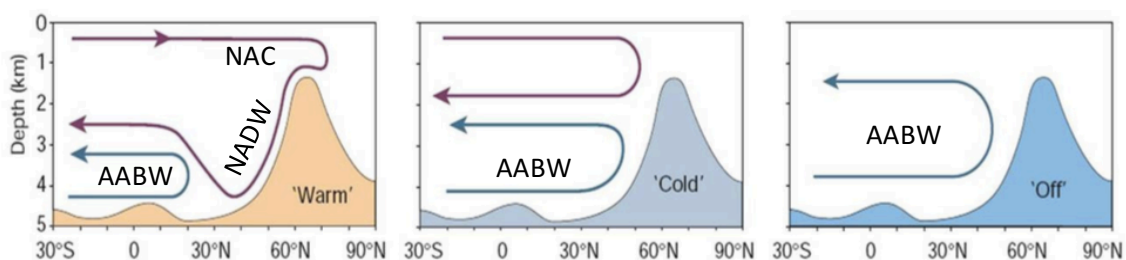


Figure 2.5: Illustration of the three modes of past ocean circulation in a section along the Atlantic. The topographic high symbolizes the Greenland-Scotland Ridge. Red line denotes North Atlantic overturning, while blue line denotes Antarctic overturning (Rahmstorf, 2002).

As mentioned above, the rate of deep water formation and overturning affects the strength of the THC. However, the location of deep water formation has also shown to vary on glacial timescales (Curry and Oppo, 2005). A southward shift in the location of deep water formation from the Nordic Seas to the south of Iceland, reduces the ocean heat transport from low to high latitudes, allowing for an expansion of sea ice – which could have amplified the glacial cooling (albedo feedback). Additionally, deglacial melting of large continental ice sheets that increase the freshwater input to the North Atlantic will in turn affect the THC. Such meltwater pulses (e.g. Meltwater Pulse 1A (Fairbanks, 1989), Younger Dryas (Manabe and Stouffer, 1995) and the 8.2 ka event (Kleiven et al., 2008)) could explain observed climate oscillations during the deglaciation and the Holocene.

Finally, evidence from benthonic $\delta^{13}\text{C}$ isotope measurements further confirms a different Atlantic Ocean circulation pattern during glacial times relative to the present (Curry and Oppo, 2005) (Figure 2.6). Today, the deep Atlantic basin is characterized by a strong convection of NADW (with high $\delta^{13}\text{C}$ values of $\sim 1.2\text{‰}$ (Eide et al., 2017)) formed in the Nordic Seas. NADW flows southward at depths of 2000-4000 m, while AABW (with $\delta^{13}\text{C}$ values of $\sim 0.2\text{‰}$ (Eide et al., 2017)) flows northward underneath the NADW cell. The last glacial maximum (LGM) reconstructions from benthonic $\delta^{13}\text{C}$ show that the NADW at that time shoaled to depths of 2000 m. Hence, the waters in the high-latitudes did not become as dense as today, reaching only intermediate depths and allowing for a stronger influence of Southern Ocean source waters (to as far as 60°N) in the North Atlantic (Keigwin and Lehman, 1994; Oppo and Lehman, 1995). However, this traditional interpretation of glacial low $\delta^{13}\text{C}$ values in the deep Atlantic has been challenged by the suggestion that increased sea ice formation in the Nordic Seas which lead to brine rejection and the production of brines with low $\delta^{13}\text{C}$ values. Brine rejection is the process where salt is rejected from the sea ice leaving the surrounding ocean water saltier (Ruddiman, 2014). Further, these brines with low $\delta^{13}\text{C}$ mix with Glacial North Atlantic Intermediate Water (GNAIW) in the Nordic Seas and are transported across the Greenland-Scotland Ridge (GSR) and subsequently spread in the deep North Atlantic (Thornalley et al., 2010). Seen in this way, the negative $\delta^{13}\text{C}$ water mass is attributed to the Nordic Seas and not the Southern Ocean.

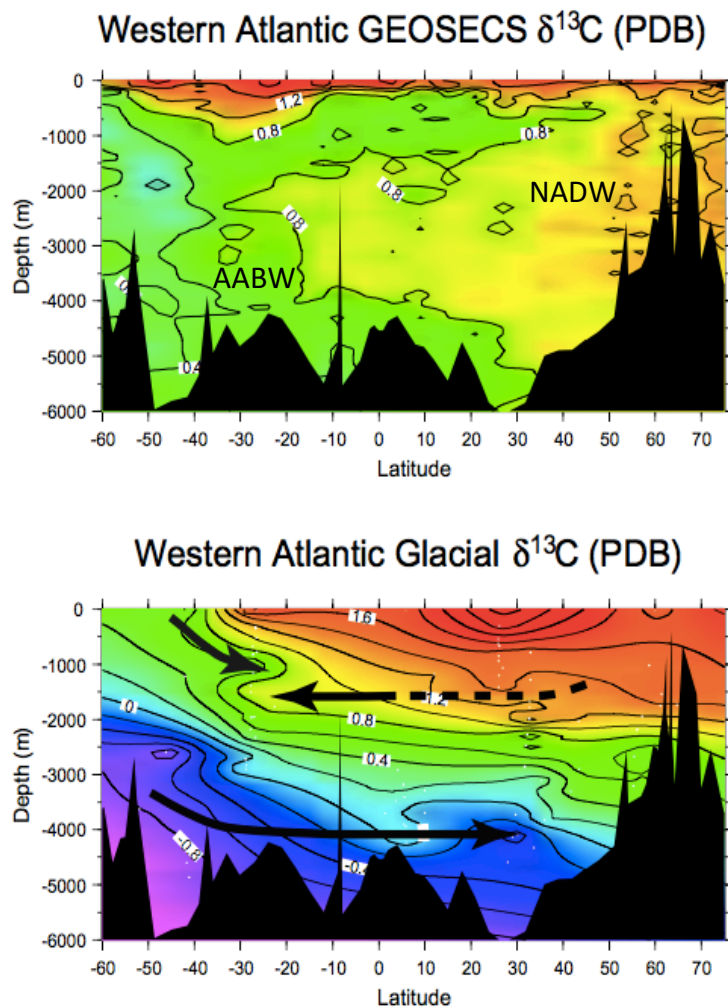


Figure 2.6: Distribution of $\delta^{13}\text{C}$ (PDB) in modern western Atlantic (top) and glacial western Atlantic (bottom). During glacial times, the Atlantic Ocean is more stratified and the deep Southern Ocean water (AABW) mass can be traced to 60°N . Northern sourced water (NADW) did not sink below depths of 2000 m (Kroopnick, 1985) revised and updated by Curry and Oppo (2005). Colour scale: Red = heavy $\delta^{13}\text{C}$ \rightarrow Green and blue/purple = light $\delta^{13}\text{C}$.

2.3.2 Future projections

Reductions in the THC are predicted to impact several parts of the climate system, among them are the El Niño-Southern Oscillation, the location of the Intertropical Convergence Zone, marine ecosystems (Schmittner, 2005) and sea level in the North Atlantic.

In the Intergovernmental Panel on Climate Change (IPCC) fifth assessment report (AR5) modellers find it very likely (90-100% probability) that the AMOC will slow down in the next decades, however the magnitude remains uncertain (Rhein et al., 2013). Models have shown that reductions in the strength of the Atlantic THC coincide with reduced ENSO variability due

to a deepening of the Pacific thermocline (up to 5 m) (Timmermann et al., 2005). In addition, models show that reductions in the THC are associated with large and rapid regional sea level changes and that cessation of NADW formation could raise the sea level along the North American Atlantic coast by up to ½ m- 1 m. A cessation of the AMOC can also cause a slow warming of the deep ocean, leading to additional sea level rise (Levermann et al., 2005). Lastly, Atlantic THC reductions are predicted to cool parts of the Northern Hemisphere which may cause a southward shift of the Intertropical Convergence Zone (ITCZ) towards the warmer Southern Hemisphere. This further causes large changes in precipitation patterns with an increasingly wetter South America and Africa, and drier and colder North Atlantic region (Vellinga and Wood, 2002).

Model experiments, using similar freshwater input (0.1 Sv) as those projected for the future, show that deep water production in the North Atlantic may decline by 30% or more by the end of this century (Stouffer et al., 2006); which will have a strong impact on the North Atlantic climate as well as tropical rainfall patterns. With larger forcing (1.0 Sv), NADW production ceases in all models (Stouffer et al., 2006). However, there is large uncertainty in the model results and the THC sensitivity to freshwater input and its multidecadal variations, as well as reversibility after shut down remains unclear. The disagreement among different model simulations reflect how complex the ocean circulation system is and hence the current limitations in future climate projections (Stouffer et al., 2006). A better fundamental understanding of ocean circulation, its variability, and its forcing is necessary to narrow these uncertainties and improve predictions.

3. STUDY AREA

The sediment core used in this study was recovered from the Eirik Sediment Drift (59° 37.1N, 40° 44.28W) at 2468 m water depth during the University of Bergen cruise GS15-196 onboard R/V *G. O. Sars* in April 2015. The core site is located east of Cape Farewell and is ideally situated to reconstruct climate and ocean variability due to its proximity to the GIS and its oceanographic setting (Figure 3.1). The core site is near the boundary between the East Greenland Current and the Irminger Current, and is therefore well positioned to record changes in the freshwater flux from the GIS and the Arctic export carried southward by the EGC. In terms of deep water circulation, the site is overlain by Denmark Strait Overflow Water (Figure 3.2), as part of the Deep Western Boundary Current and is therefore well positioned to record changes in the strength of proto-North Atlantic Deep Water. The core is located on the steeply sloping northern drift flank of the Eirik Sediment Drift (see Figure 3.10). In this area DWBC is strong and in the regions where the bottom water flows are at its strongest the conditions are non-depositional or even erosional, resulting in a relatively low sedimentation rate for the Holocene (Hunter et al., 2007).

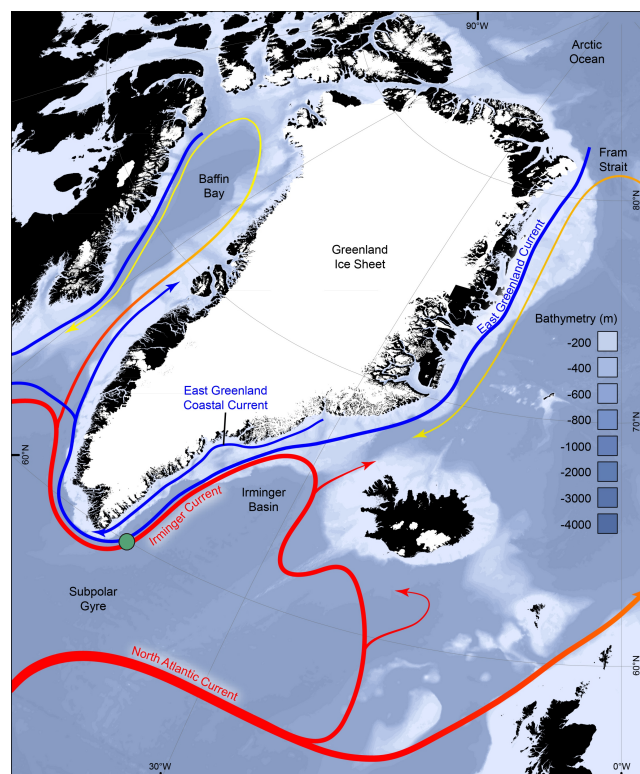


Figure 3.1: Surface ocean circulation around the GIS (1:18 000 000). The green dot denotes the GS15-196-02GC core site. Colours illustrates the relative temperatures of the surface current, blue=cold and red=warm. Modified from Bacon et al. (2002); Jakobsson et al. (2012); Straneo et al. (2012) in Dyke (2016).

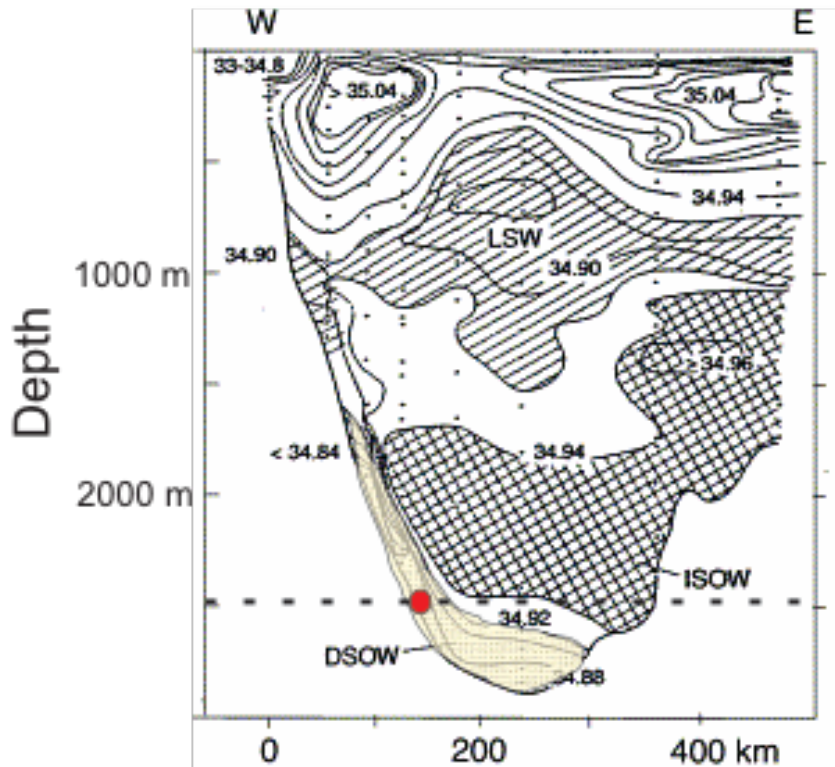


Figure 3.2: Vertical distribution of water masses in the Irminger Sea. Km west-east indicates the distance from the Greenland margin. Numbers in the plot denote salinity. Scale to the left shows the water depth. DSOW is shaded in yellow. The red dot notes GS15-196-02GC core depth location. Modified from Dickson and Brown (1994); Kuijpers et al. (2003).

In the next subchapters, the general bathymetry and oceanography in the study region will be presented.

3.1 Bathymetry

Below 840 m water depth, the Greenland-Scotland Ridge (Figure 3.3) forms a continuous barrier between the deep basins of the northern North Atlantic and the Nordic Seas and Arctic Ocean. Iceland and the Faroe Islands divide the ridge into three gaps, with respective troughs that control deep water exchange between the deep basins north and south of the ridge. The deepest troughs are the Denmark Strait (620 m) between Greenland and Iceland, and the Faroe Bank Channel (840 m) between Iceland and Scotland (Hansen and Østerhus, 2000).

The ocean region north of the GSR is divided into the Arctic Ocean and Nordic Seas. Southwest of the ridge, three basins are divided by two shallow structures. The Reykjanes ridge, the northern extension of the Mid-Atlantic Ridge (MAR), separates the Irminger Basin from the

Iceland Basin. To the east, the Iceland Basin is further separated from the Rockall Channel by the Rockall-Hatton Plateau (Hansen and Østerhus, 2000) (Figure 3.4).

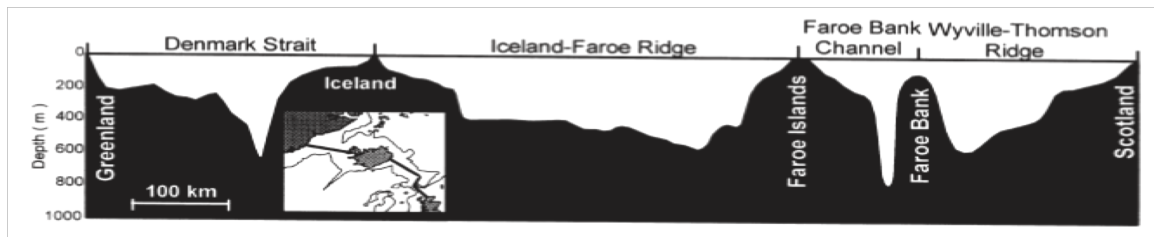


Figure 3.3: Bathymetric west-east profile (see inset map) of the Greenland-Scotland ridge in the North Atlantic (0-1000 m water depth) (Hansen and Østerhus, 2000).

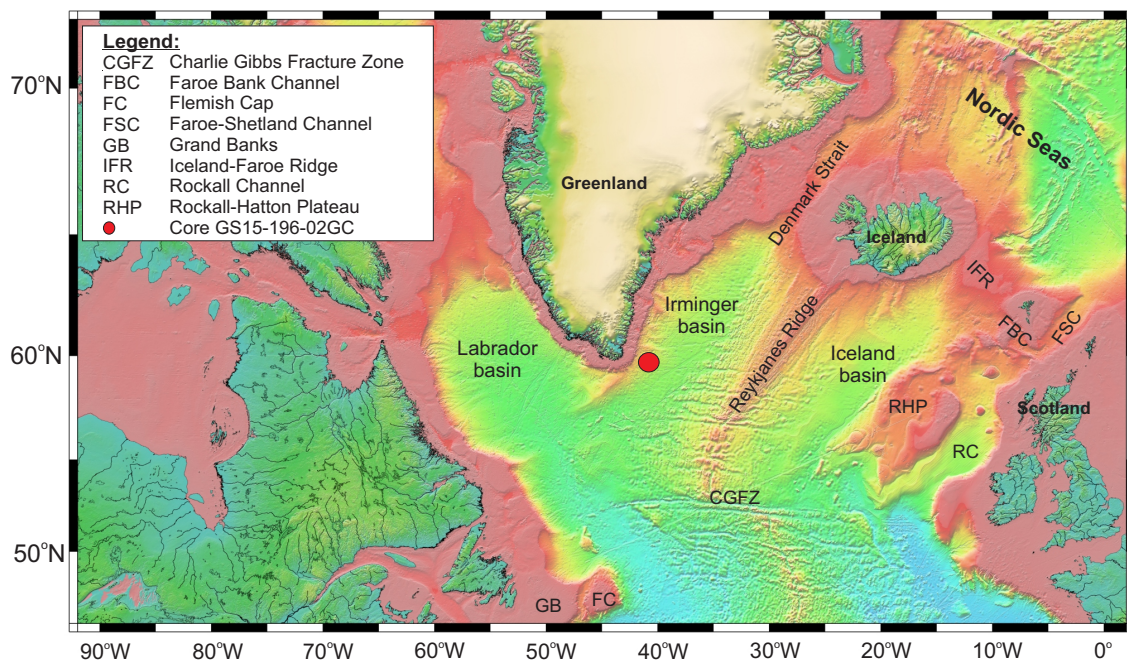


Figure 3.4: Bathymetric map of the North Atlantic. The red dot denotes the GS15-196-02GC core location. See legend for abbreviations. Modified from Smith and Sandwell (1997).

3.2 Oceanography

This subchapter describes the near-surface and deep ocean circulation patterns in the North Atlantic and partly the Nordic Seas that are of importance for this study.

In the North Atlantic Ocean, the Gulf Stream and its continuation, the North Atlantic Current (NAC) transports warm and salty water from the Gulf of Mexico northwards. In the North Atlantic high latitudes, large volumes of this surface water sinks to depths below 2000 m.

Inflow of new surface waters from the south compensate for this sinking water. Thus, a circulation pattern from south to north in the Northern Hemisphere (THC) partially compensate for the imbalance in solar energy received at different latitudes on the Earth.

3.2.1 Surface circulation

The major surface circulation (Figure 3.5) in the North Atlantic is dominated by the anticyclonic subtropical gyre located between 20°-40°N and the cyclonic subpolar gyre between 50°-70°N, both strongly influenced by the Coriolis force and wind patterns. The major current features associated with the gyres in the Atlantic includes the warm, fast, deep and narrow western boundary currents and the slower and shallower eastern boundary currents, creating an asymmetrical flow pattern from west to east in the gyres. In the Northern Hemisphere, the western boundary currents include the Gulf Stream, which continues as the North Atlantic Current in high latitudes (40°-51°N) (Rossby, 1996). This surface current is the main carrier of warm water from low to high latitudes in the Northern Hemisphere. The eastern boundary current includes the Canary Current off the European and African coasts. Large parts of the NAC turn southeast to contribute to the Canary Current and recirculate in the subtropical gyre, while other parts contribute to the subpolar gyre, connecting the subpolar and subtropical gyres (Cronin, 2010).

After passing Grand Banks, the Gulf Stream splits into several branches, the largest being the NAC that continues its flow path northeast. This flow turn east at 50°-52° N, crossing the MAR close to the Charlie Gibbs Fracture Zone (CGFZ) (Rossby, 1996). Shortly after crossing the MAR the NAC splits into several branches. The Irminger Current branches off, flowing north to northeast, along the eastern side of the MAR, towards Iceland before crossing west over the ridge. The IC is further separated along the Reykjanes Ridge, south of the Denmark Strait, where the main bulk of water meets the southward flowing East Greenland Current. The remainder continues in an anticyclonic fashion around the Icelandic continental shelf, quickly losing the salinity and temperature properties of North Atlantic water and contributing with a small portion of the net inflow of Atlantic water to the Nordic Seas (Krauss, 1995). The IC water that is not mixed with the EGC flows southwards, parallel to the EGC.

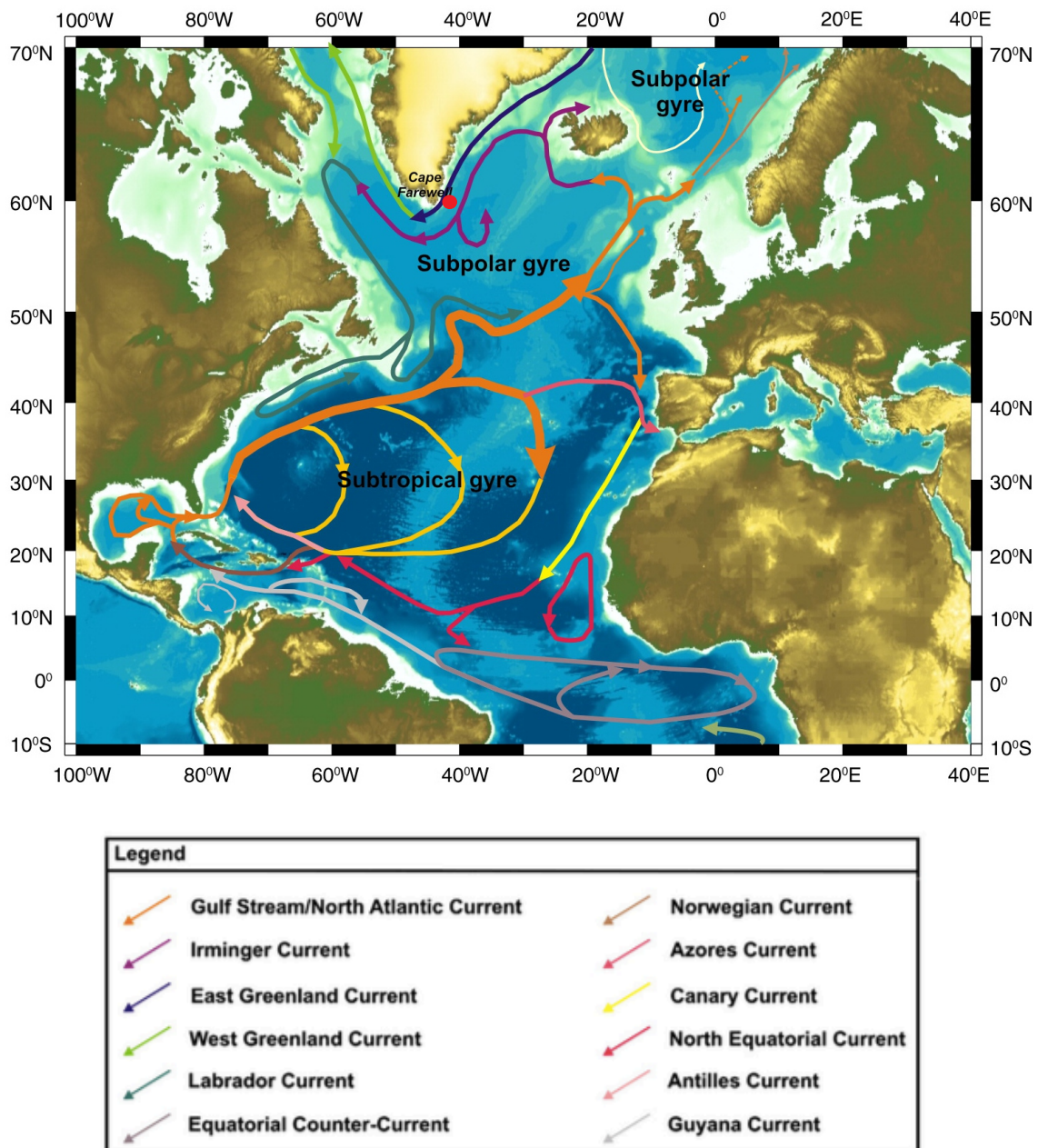


Figure 3.5: Map of the surface circulation in the North Atlantic region. Red dot denotes the location of core GS15-196-02GC. Modified from Stanford et al. (2011).

After the IC has branched off, the remainder of the NAC flows toward the northeast, crossing the Rockall Hatton Plateau. Further north, when the NAC approach the Faroe Islands it splits into two branches. Both cross the GSR and enter the Nordic Seas (Hansen and Østerhus, 2000). However, one branch flow towards the Iceland-Faroe Ridge (the Faroe Current), cross the ridge and encounters colder and less saline waters in the Iceland-Faroes Front. The other branch flow into the Faroe-Shetland Channel (Shetland Current) and follow the European continental slope northward (Hansen and Østerhus, 2000).

Once crossed the GSR the different branches of the NAC continue into the Nordic Seas and gradually into the Arctic Ocean (Figure 3.6) as the Norwegian Atlantic Current (NwAC). In general, the two-branch system of the NwAC has been used as a collective term for the northward continuation of the Faroe and Shetland Currents, however it must be noted that the two currents in many cases should be considered as separates. The western branch of the NwAC, the continuation of the Faroe Current, is topographically controlled by the Vøring Plateau and is directed towards Jan Mayen (Poulain et al., 1996). The main water masses in this branch continue northward along the slope of the Mohn Ridge, while a small portion recirculate in the Nordic Seas. The eastern branch of the NwAC, the continuation of the Shetland Current, continues northward along the Norwegian Continental Shelf edge towards the Arctic. This current then splits, with one branch entering the Arctic Ocean through the Fram Strait and another the Barents Sea (Orvik and Niiler, 2002).

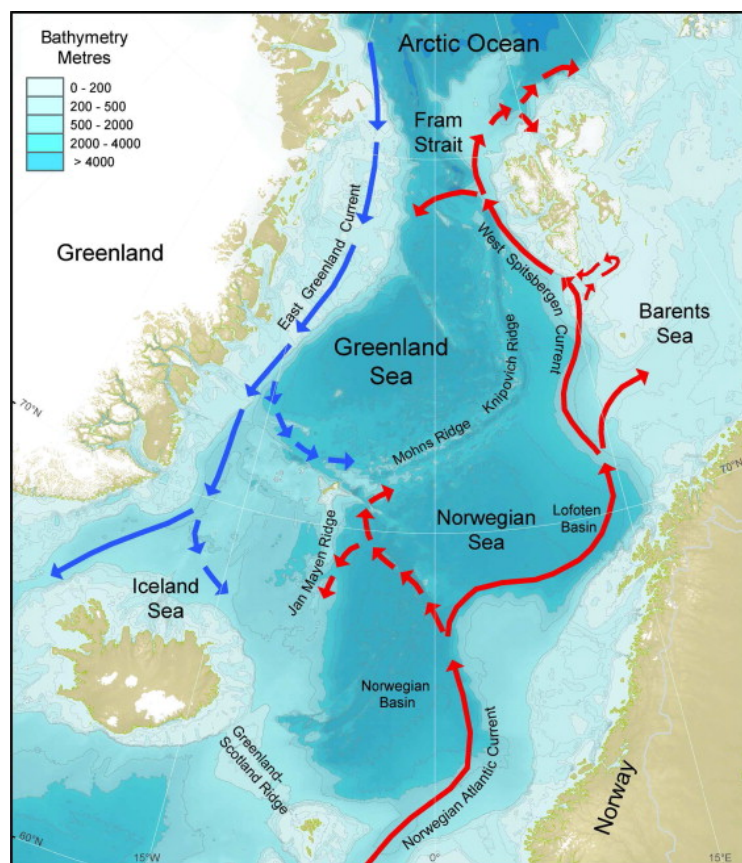


Figure 3.6: Map of the surface circulation in the Nordic Seas. Red=warm, blue=cold (Isachsen et al., 2014).

In the Arctic Ocean, the water remnants of the NAC circulate within the Arctic where its modified and eventually exits through the Fram Strait and flows south along the eastern continental shelf of Greenland as the EGC. The EGC transports low salinity Polar Ocean water, sea ice, deep-intermediate Arctic water and re-circulated Atlantic water (Rudels et al., 2002). Parts of the fresh Polar Ocean water branches out from the EGC at the Jan Mayen Fracture Zone and enters the Greenland Sea, and continues towards Jan Mayen and the Mohn Ridge as the Jan Mayen Current (Rudels et al., 2002). The remainder of the EGC continues southward through the Denmark Strait, enters the Irminger Basin and continue towards Cape Farewell. The EGC is considered to be the main source of DSOW (Rudels et al., 2002) and together with the East Greenland Coastal Current (EGCC) it is considered to be the main conduit for fresh polar waters to reach the lower latitudes of the North Atlantic (Hansen and Østerhus, 2000).

When approaching the south-eastern coast of Greenland, the EGC flow between the EGCC to the west and the IC to the east. There is a sharp boundary between the cold and fresh EGC and the warm and saline IC (Krauss, 1995). The EGCC is a seasonal, cold and fresh current originating from polar waters that flow southward along the east Greenland continental shelf. The GIS is believed to be the source of the EGCC freshwater signal (Bacon et al., 2002). However, some of the freshwater content in the EGCC stems from local melting of sea ice transported from the Arctic Ocean through the Fram Strait (Bacon et al., 2014). Since the EGCC is a direct recipient of freshwater runoff from the GIS, the freshwater transport is likely to increase if the ice sheet net ablation and freshwater runoff increases (Bacon et al., 2014). Additionally, retroflection of a portion of the EGC south of Cape Farewell (Holliday et al., 2007) provides a direct route for EGC to enter the subpolar gyre, where the freshwater can decrease the density of surface waters and inhibit deep water formation in the Irminger and Labrador basins (Bacon et al., 2014). The EGCC is strengthened during the summer due to enhanced density stratification caused by increasing freshwater input from melting continental ice (Bacon et al., 2014). The core used in this study is located east of the EGCC, near the boundary between the EGC and the IC.

Around Cape Farewell, the IC subducts under the EGC and EGCC, to become Irminger Sea Water (ISW), which flows into the Labrador Basin on the west coast of Greenland. Here, the EGC and EGCC merges and continues as the West Greenland Current (WGC) (Jakobsen et al., 2003). In the Labrador Basin, the cold and fresh WGC flow inshore of the warm and saline ISW (Holliday et al., 2007). The WGC propagate north along the western coast of Greenland

towards south of the Davis Strait, where it separates in two branches; one of which continues north through the Davis Strait and into Baffin Bay, while the other turns westward and follows the topography (Jakobsen et al., 2003). The Baffin Bay branch turns south just after passing through the Davis Strait, again flowing through the strait and merges with the second branch of the WGC, joining the Labrador Current (LC) southwards. The LC is a shallow current that flows southward along the Labrador coast on the western side of the Labrador Basin. The transport velocities are at its maximum in late summer due to increased freshwater flux from Baffin Bay (Cuny et al., 2002). The LC continues towards Grand Banks, where the current splits. Most of it turns northeast and joins the NAC, while a minor part of the current continues westward (Rossby, 1996). Lastly, the LC, EGC and the IC contribute to the southward flowing western part of the subpolar gyre.

3.2.2 Deep ocean circulation

The deep ocean circulation in the Atlantic is dominated by two water masses; North Atlantic Deep Water and Antarctic Bottom Water. These water masses exhibit different properties (e.g. temperature, salinity and nutrient composition) and their transport route can therefore be traced far from the source region. Compared to AABW, NADW (2-4°C and ~35 psu) is relatively warm, and lies stratigraphically above the colder AABW (0-2°C and ~34.6 psu) (Broecker, 1991). Together these water masses drive the global thermohaline circulation. AABW forms around the Antarctic continent through brine formation and cooling at the surface. When sea-ice is formed on the continental shelves around Antarctica, the salt is rejected, increasing the salinity of the surface layer. Consequently, this high-density water with increased salinity sinks. Because AABW also is colder than NADW, it sinks underneath NADW and flows northward in the deepest basins of the Atlantic (Figure 3.7). In the North Atlantic, NADW is formed through winter convection in the Labrador and Nordic Seas. The source of NADW is warm water that originates in the tropics and subtropics. This water flows north and becomes saltier due to evaporation. When arriving in the high-latitudes, it cools and sinks (2000-4000 m) overlaying the AABW (Rahmstorf, 2006).

NADW is the most nutrient depleted deep water mass forming in the world ocean today and the phosphate concentration is generally very low (Figure 3.8). This is due to its source water, which is depleted in nutrients such as phosphate, because of high productivity. AABW however, contains higher nutrient and phosphate concentrations than NADW and the mixing of low nutrient NADW flowing north to south and high nutrient AABW flowing south to north

results in a strong horizontal and vertical nutrient gradient in the deep Atlantic basin (Hillaire-Marcel and Ravelo, 2007).

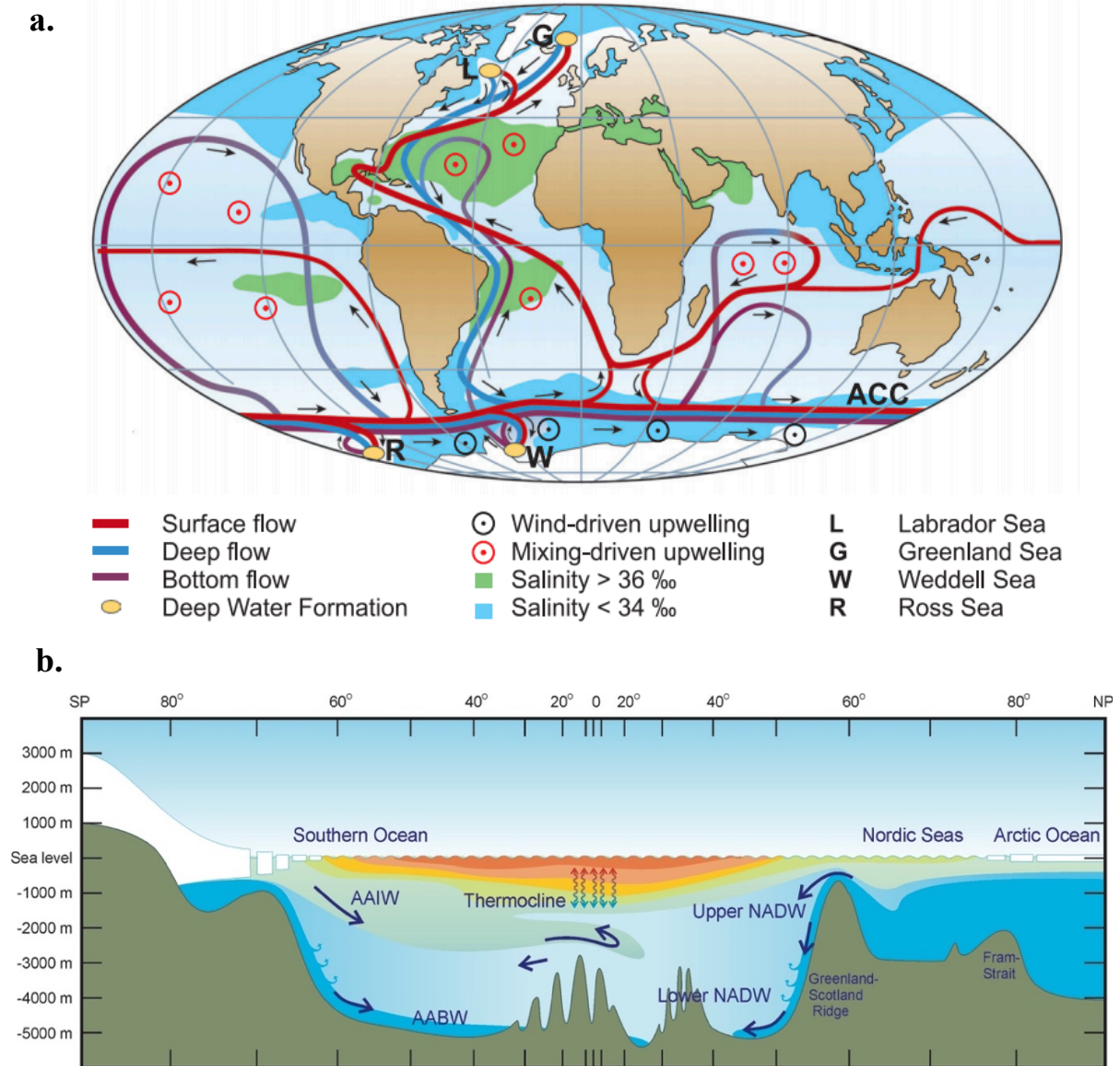


Figure 3.7: a. Global distribution of the thermohaline circulation (THC). Note the four places where deep water formation occurs; Labrador, Greenland/Nordic, Weddell and Ross Seas (yellow dots) (Rahmstorf, 2002) b. Cross-section (60°S-60°N) of the Atlantic Basin. Stratigraphically AABW underlies NADW (Fer, 2012).

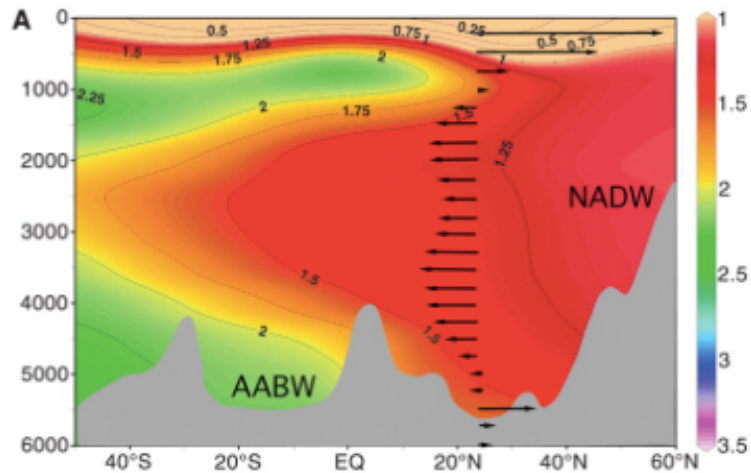


Figure 3.8: The modern distribution of phosphate ($\mu\text{mol/liter}$) in the western Atlantic. The figure illustrates the substantial differences in nutrient concentration between NADW and AABW. Arrows indicate the flow direction (Lynch-Stieglitz et al., 2007).

North Atlantic Deep Water

North Atlantic Deep Water originates from three distinct water masses with different densities and water depths: Nordic Sea Overflow Water (NSOW), originating from mid-depths in the Nordic Seas, Labrador Sea Water (LSW) formed in the western subpolar Atlantic and a smaller contribution from AABW (Haine et al., 2008) (Figure 3.9). The dense water formed in the Nordic Seas, collectively known as NSOW, spills southward across the GSR, forced by a pressure gradient between the waters north and south of the ridge. The water mass crosses the ridge in two separate currents, mainly through the deepest conduits of the ridge; the Denmark Strait known as Denmark Strait Overflow Water, and the Faroe Bank Channel known as Iceland-Scotland Overflow Water (ISOW). DSOW is the densest component of the two (Dickson and Brown, 1994) and transports approximately 2.9 Sv to the DWBC. The composition of DSOW is complex, but Arctic water flowing in the EGC southward from the Arctic Ocean to the Denmark Strait has been suggested as the largest contributor to DSOW (Mauritzen, 1996). However, there is also some contribution from the Nordic and Greenland Seas. Furthermore, a variable influence of Polar waters is suggested to be important in freshening the DSOW (Tanhua et al., 2008). Even though most of the water mass mixing occurs north of the strait, the water mass is not completely formed when passing through the strait, since active mixing within the overflow as well as entrainment of ambient water masses still occurs south of the GSR (Rudels et al., 1999). In addition, it has been suggested that a reduction

ISOW originates in the Norwegian and Greenland Seas (Smethie et al., 2000). After crossing the GSR and entering the eastern North Atlantic, ISOW flows along the eastern flank of the Reykjanes Ridge and turns westward passing through the CGFZ and continues further into the Irminger basin (Haine et al., 2008). On this route, the density of the ISOW is reduced due to entrainment of ambient water masses and therefore it forms the upper limb of the DWBC at depths around 2000 m. It is estimated that ISOW contributes with 2-3 Sv to the DWBC (Dickson and Brown, 1994).

From the south, Lower Deep Water (LDW), originating from AABW, is entrained in both ISOW and DSOW, and circulates around Cape Farewell and into the Labrador Basin (McCartney, 1992). Once entered the Labrador Basin, this flow joins Labrador Sea Water and flows southward (McCartney, 1992).

The last water mass contributing to NADW is LSW formed in the Labrador Sea during wintertime. LSW is considered to be the lightest constituent of NADW and is described as a cold and fresh water mass with high oxygen content (Talley and McCartney, 1982). LSW can be traced at mid-depths (down to 2000 m) in a broad area north of 40° in the North Atlantic (Talley and McCartney, 1982). During wintertime, cold winds from the Arctic cause increased atmosphere-ocean heat exchange in the Labrador Sea, transferring heat from the surface ocean to the atmosphere. This heat loss creates the dense winter layer accumulating in the water mass known as Labrador Sea Water (Yashayaev et al., 2008). It has been a common belief that LSW is formed solely in the Labrador Sea. However, a second convection site east of Greenland, in the western Irminger Sea, has been identified, forming Upper Labrador Sea Water (ULSW) at depths of 1500-2000 m (Pickart et al., 2003). ULSW is lighter than LSW, but in large part follows the same pathway. A large part of LSW flows southwest joining the DWBC. Formation of LSW has large scale global impacts and contributes to the MOC, the global heat flux and modification of Nordic Sea Overflow waters. Because LSW formation is central in the formation of NADW in the subpolar Atlantic and is strongly modulated by the GIS and Arctic wind patterns, many consider LSW formation and a possible reduction of this as the most vulnerable component of the MOC in the coming decades (Kawasaki and Hasumi, 2014).

The DWBC, now consisting of ISOW, DSOW, LDW and LSW (and ULSW) enters the Labrador Basin and flows southward along the continental slope of northeastern North America. When the current reaches Grand Banks, it constitutes fully formed NADW. The

DWBC that passes Cape Farewell, close to the study site in this thesis, is considered as proto-NADW, and is often referred to as Lower North Atlantic Deep Water (LNADW) (Hunter et al., 2007) as it is most strongly influenced by DSOW. Considered to be nearly mature, this water mass represents the major constituents of NADW and is thus a good representation of NADW properties.

3.3 Contourites

“Contourites are the sediments deposited by or significantly affected by the action of bottom currents” (Stow et al., 2002, p. 8). Since contourites were first recognized in the 1960’s, the importance of bottom currents for sediment transport has been acknowledged. These bottom currents, which flow in response to the thermohaline and wind-driven circulation, deposit large-scale sediment accumulations on the ocean floor. These accumulations have been thoroughly studied and named “sediment drifts” or “contourite drifts”. The study of contourite drifts has been used in paleoclimate and paleoceanographic research, revealing information of variability in the ocean circulation system, current velocities and oceanographic history. Because of high sedimentation rates, contourite drifts have the potential for high-resolution paleoceanographic reconstructions of major ocean current systems (e.g. (Bianchi and McCave, 1999; Kleiven et al., 2008; Irvali et al., 2012)), which make them especially interesting.

3.3.1 The Eirik Sediment Drift

The Eirik Sediment Drift (Figure 3.10) is the study area in this thesis. This contourite drift is defined as a detached elongated mounded drift (Stow et al., 2002). The drift extends approximately 360 km from the Greenland margin in the north (1500 m water depth) to the southwest (3400 m water depth) and is built up by the DWBC/proto-NADW, downstream of the deep water formation sites in the Nordic Seas (Müller-Michaelis and Uenzelmann-Neben, 2014). The drift morphology is strongly influenced by the topography, characterized by a steep but regular slope of 1.3° . The northern part of the drift shows slope variations between 0.3° and 1.5° , identifying three secondary ridges. It is suggested that these ridges were created when the DWBC branched out in three parts, each part depositing an isolated ridge. These three ridges extend northwest, relative to the main drift, and underlie the DWBC as it flows towards the Labrador Sea (Hunter et al., 2007).

The build-up of the Eirik drift is believed to have initiated 4.5 Ma ago during the early Pliocene, continuing with significant sediment accumulation through the Pleistocene as bottom currents weakened due to increased glacial activity (Hunter et al., 2007). Today, the Eirik drift is considered to be for the most part inactive (Hunter et al., 2007), although thick Holocene sediment accumulations have been found the southern parts of the drift (Hillaire-Marcel et al., 1994). The sediments in the Eirik drift are deposited as the southward flowing currents flow along the east Greenland margin approaching the southern tip of Greenland and the Coriolis force causes the currents to shift flow direction back north, flowing along the west Greenland margin. This shift in flow direction, controlled by the Coriolis force, cause the flow to slow down, reducing its competence and capacity and allowing for thick accumulations of sediment to be deposited (Wold, 1994).

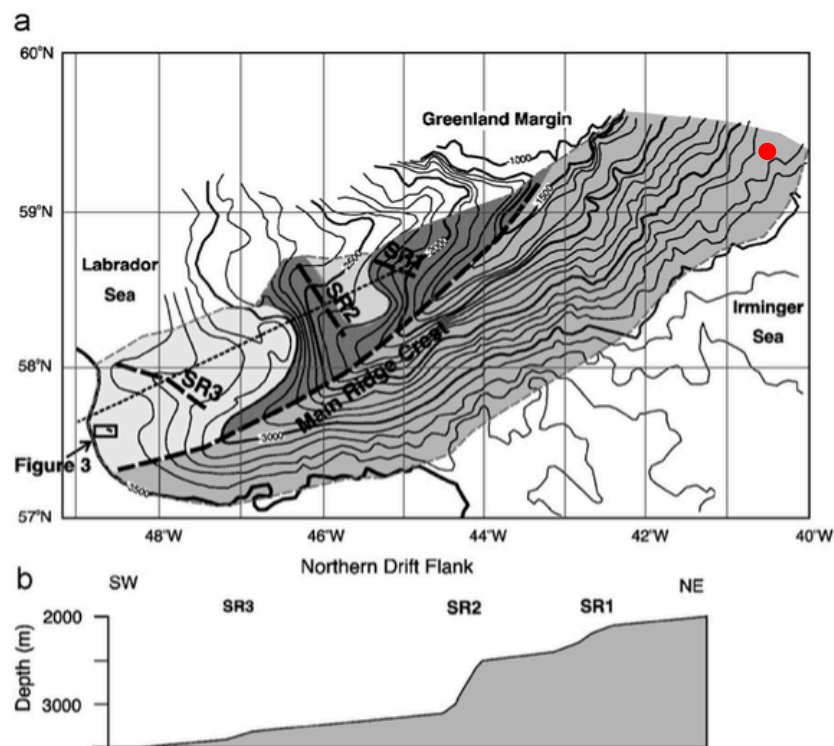


Figure 3.10: a) Bathymetric map of the Eirik Drift. SR1-3 denotes the secondary ridge crests. Darker shading indicates areas of steeper slope. b) Cross section of the northern drift flank (dotted line in a)). The red dot marks the location of core GS15-196-02GC. Modified from Hunter et al. (2007).

Sediments from the Eirik drift document changes in the flow pattern and intensity of the DWBC/proto-NADW, which reflect variability in deep water formation in the Nordic Seas coupled with climate change. Parts of the Eirik drift exhibit sedimentation rates of >30 cm/1000 year (Hillaire-Marcel et al., 1994; Hunter et al., 2007), making it a suitable area to study high-resolution millennial to decadal scale climate and ocean variability.

4. MATERIAL AND METHODS

This chapter describes the laboratory procedures involved in generating the data presented in this thesis. The laboratory work was carried out at EARTHLAB (Earth Surface Sediment Laboratory) and FARLAB (Facility for Advanced Isotopic Research), both at the Department of Earth Science, UoB.

4.1 Core GS15-196-02GC

Core GS15-196-02GC, studied in this thesis is recovered using a gravity corer. The complete length of the core is 334.5 cm. The core was cut into three sections and each section was split into a working half core and an archive half core. The working halves were used for image scan, MST-scanning, core description and sampling. Later during the study, the archive halves were used for XRF-analysis. Smear slides were taken to sample the changing lithology in the core. The smear slides were examined under a microscope and used to name the different lithological units downcore. Detailed core description is given in subchapter 6.1.

4.2 Laboratory methods

This section describes the laboratory methods applied in this study with a short theoretical summary for the different instruments.

4.2.1 Multi-sensor-track (MST)

Multi-sensor-track is a non-destructive core measurement device used to recover geophysical properties of both whole and split marine sediment cores. The MST device measures P-wave velocity, bulk density and magnetic susceptibility (ms) at predefined intervals downcore. The system consists of four parts: (1) a central sensor array, (2) a motorized track that push the core past the measuring sensors, (3) electronic interface transferring data to the logging computer and controlling the sensor settings and (4) a logging computer recording data (Gunn and Best, 1998). When measuring magnetic susceptibility of split cores, a point sensor is used. The point sensor is moved up and down, into and out of contact with the sediment surface, thereby creating a low frequency magnetic field and measuring the magnetization of the material. Readings of magnetic susceptibility are usually given in SI (10^{-5}) or cgs units (Gunn and Best, 1998). For this study, magnetic susceptibility was measured at intervals of 0.2 cm downcore at EARTHLAB, UoB.

Magnetic susceptibility is a measurement of how easily a material can be magnetized. The magnetism of a material is controlled by the inherent forces of the electrons within the atoms. Electrons spin around their own axis, creating a magnetic field. The way in which different electrons spin align determine the total magnetic energy of the atom. There are five different types of magnetic behaviour: ferromagnetic, ferrimagnetic, antiferromagnetic, paramagnetic, and diamagnetic. Ferro – and ferrimagnetic materials (e.g. magnetite) exhibit strong positive magnetic susceptibility, whereas diamagnetic materials (e.g. water, organic material, quartz, calcium carbonate) exhibit weak and negative magnetic susceptibility (Dearing, 1994).

In the northern North Atlantic, magnetic minerals mainly originate from the same source area; the Nordic Basaltic province. Hence, changes in the magnetic composition at the core site may reflect changes in the competence of deep currents to transport magnetic minerals from the source area to deposition at the core site (Kissel et al., 1999). However, other studies have linked peaks in magnetic susceptibility to IRD rich layers deposited during Heinrich events. A study from the Rockall Plateau found a correlation between Heinrich events 1, 2, 4, 5 and 6, and increases in magnetic susceptibility (Chi and Mienert, 1996), derived from the plutonic rocks in the Hudson Strait region (Grousset et al., 1993). This suggests that changes in the magnetic susceptibility at the core site may reflect changes in the transport of magnetic minerals from the Hudson Strait by icebergs calving off the Laurentide Ice Sheet.

4.2.2 X-Ray Fluorescence (XRF) analysis

The ITRAX core scanner at EARTHLAB, UoB, was used to recover the optical and microradiographic images and elemental variations of the complete GS15-196-02GC archive core. This core scanner is a non-destructive core measurement device used to gather optical and microradiographic images and elemental variations (aluminium and heavier) simultaneously for the same core section. The ITRAX core scanner consists of a measuring tower containing an X-ray focusing unit and several sensors (Croudace et al., 2006). Prior to analysis, the core surface was carefully scraped clean and covered with a thin foil. Each section was scanned at intervals of 0.2 cm downcore. Elemental readings are usually given in ratios or cps (counts per second). The core scanner used the following settings; voltage = 60 kV, current = 50 mA and exposure time = 375 ms.

Ca/Sr variations are of interest when considering IRD rich layers in the North Atlantic. Biogenic CaCO₃ contain greater amounts of strontium (Sr) than inorganic CaCO₃. Thus, high Ca/Sr can

be used to detect IRD layers rich in detrital carbonate, such as some Heinrich layers (Rothwell and Croudace, 2015). In general, Heinrich layers 1, 2, 4 and 5, contain increased Ca-content and low Sr-content, resulting in high Ca/Sr ratios (usually Ca/Sr values of 200 or more). Heinrich layers 3 and 6 are usually not associated with high Ca/Sr content (Hodell et al., 2008b). The comparison of Ca/Sr and Si/Sr ratios in North Atlantic sediment cores is based on differences in bedrock geology around the North Atlantic region. In the Hudson Strait area, the bedrock consists of large Paleozoic carbonate platforms, whereas the bedrocks in Greenland, Iceland, Scandinavia and Britain are comprised of (Precambrian) crystalline igneous and metamorphic shields, and not carbonate platforms (Naafs et al., 2013). Hence, increased Ca in layers associated with Heinrich events are believed to be derived from Paleozoic limestones from the Hudson Strait region and related to surges of the LIS. Si/Sr reflect layers that are poor in biogenic carbonate and rich in detrital silicate minerals (Hodell et al., 2008b), and believed not to be derived from the Hudson Strait and the LIS.

4.2.3 Sampling

The GS15-196-02GC working halves were sampled at EARTHLAB, UoB, at 1 cm spacing intervals. Bulk samples were dried in a heating cabinet (50°C) and then weighed. To disaggregate the sediments the samples were shaken for 24 to 48 hours in distilled water, before they were wet sieved into three fractions; >150 µm, 150-63 µm and <63 µm. Next step was to dry the samples in a heating cabinet (50°C) to evaporate all the water. Finally, the dry weights for the two largest fractions were noted and the samples were transferred to sample glasses. The >150 µm and 150-63 µm fractions were later used for picking of foraminifera and lithic counts, while the <63 µm fraction was stored for later analysis.

4.2.4 Smear slides

Smear slides are used for identifying, describing and classifying the sediments found in marine sediment cores. When sampling for smear slides all lithologies in the core should be represented, therefore the frequency of smear slide sampling depends on changing lithologies and/or the presence of unusual features that could be interesting to study in more detail. In total 11 smear slides were made from the GS15-196-02GC core.

A toothpick was used to sample small parts (1-2 mm³) of the surface sediments. The sample was placed on a microscope slide and a few drops of distilled water were added. The sample

was smeared out on the slide using a toothpick and placed in a heating cabinet to allow for the residual water to evaporate. Then, Norland Optical Adhesive 61 was added to the sample and a glass cover placed on top and cured using UV light. Lastly, the smear slides were examined under a microscope and used to name different lithologies in the core (see Figure 6.1).

4.2.5 Picking foraminifera and counting Ice rafted debris (IRD)

In this study, IRD was counted with 4 cm sample spacing. Every sample was divided in equal parts using a microsplitter until the remaining size was at least 250-300 grains. The IRD grains and foraminifera in the >150 μm fraction was counted under the microscope and the % of IRD calculated. In intervals of special interests and to achieve higher resolution, IRD was counted every 1 cm (intervals 105 cm-114 cm and 127 cm-134 cm). In order to calculate standard deviation, repeated counts were carried out at approximately every 50 cm.

When selecting foraminifera for stable isotope analysis, only the largest sample fraction (>150 μm) was used. Two species of foraminifera were picked; the planktonic species *Neogloboquadrina pachyderma* (sinistral) (hereinafter *N. pachyderma* (s)) and the benthonic species *Cibicidoides wuellerstorfi* (hereinafter *C. wuellerstorfi*). Prior to picking, the samples were dry sieved in four fractions; >250 μm , 212-250 μm , 150-212 μm and 63-150 μm . *N. pachyderma* (s) was selected from the 212-250 μm fraction, while *C. wuellerstorfi* was selected from all fractions depending on the abundance. Narrow size constraints were used for planktonic foraminifera selection to minimize possible ontogenic effects (developmental history of an individual organism). For example, the isotopic values of planktonic foraminifera can change with shell size (Berger et al., 1981), physiological (Zeebe, 1999) or habitat effects (Ravelo and Fairbanks, 1992; 1995) as foraminifera can change their position in the water column over the span of its life time and accumulate calcite at different depths (this concept is explained in detail in subchapter 4.5). Therefore, all *N. pachyderma* (s) used for analysis were chosen from the same narrow size fraction.

4.2.6 Preparation for stable isotope analysis

Sample preparation

When preparing samples for mass spectrometer analysis the optimal sample weight is 40-70 μg which assures a complete reaction. To make sure that the samples were within this weight limit most of the samples were weighed. In general, about 6-7 *N. pachyderma* (s) shells and 1-5 *C.*

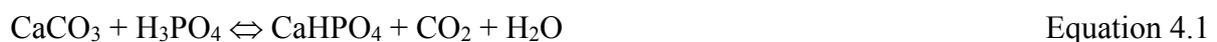
wuellerstorfi shells were used in each sample run. For the planktonic species, repeated runs were carried out for every third depth interval. For the benthonic species, repeated runs were carried out when possible. This was done to quantify and minimize the uncertainty.

Removal of contaminants

The cleanest foraminifera were selected for isotopic analyses. Even so, the samples were cleaned prior to isotopic analysis in order to remove any remaining sources of contamination attached to the foraminifera shell. In addition, most of the benthonic shells were cracked open prior to the cleaning step to ensure that (1) complete reaction was achieved for maximum sample yield, and (2) to expose and release any potential contaminants during the cleaning step. The foraminifera shells were ultrasonicated in methanol (CH₃OH) for approximately five seconds to dislodge and suspend any fine fraction contaminants. The methanol was then carefully drawn off using a syringe, making sure that no sample material was removed. Subsequently, the samples were placed in a heating cabinet (50°C) to allow for the residual methanol to evaporate.

4.3 Mass spectrometry

Stable isotope analysis of *N. pachyderma* (s) and *C. wuellerstorfi* was carried out in FARLAB at the Department of Earth Science, UoB, with the use of a Finnegan MAT253 gas source mass spectrometer. The stable isotopes of carbon and oxygen are determined by the mass ratios of carbon dioxide (CO₂) obtained from the sample when the carbonate foraminifera shell reacts with phosphoric acid, a method developed by (McCrea, 1950):



Derived from Equation 4.1, all of the carbon is converted to CO₂, indicating that all of the carbon in calcium carbonate is recovered and that the δ¹³C can be directly measured. However, fractionation of oxygen occurs and only 2/3 of the oxygen content in the carbonate is converted to CO₂. This fractionation is a function of the temperature at which the reaction takes place, and can be corrected for using the fractionation factor defined in Equation 4.2 (Rohling and Cooke, 1999). Water-free orthophosphoric (100% H₃PO₄) acid is used to prevent oxygen exchange between the phosphoric acid and CO₂, and with these corrections the oxygen isotope content can be measured (Clark and Fritz, 1997). The results are reported relative to a standard

with known isotopic composition. For both oxygen and carbon in carbonates the standards are referred to as PDB scale or VPDB (scale developed after the source of PDB was exhausted), further explained in section 4.3.1.

Since Alfred Nier in 1947 developed the first dual-inlet gas source mass spectrometer, his method has become the preferred method for measuring isotope ratios of light elements (e.g. H, C, N, O). The mass spectrometer consists of three parts; the ion source, the mass analyser and the detector (Figure 4.1). A computer is also utilized to collect and process the data. The ion source creates gas phase ions under low pressure. The ions are then focused into a beam and travels through a tube that bends corresponding to an electromagnet. The magnet separates the ions according to their mass/charge ratio and the resulting ion beams are sent to the detectors that captures the ion beams of interest. The ion beams for mass 44 (^{12}C , $^{16}\text{O}_2$), mass 45 (^{13}C , $^{16}\text{O}_2$ or ^{12}C , ^{17}O , ^{16}O) and mass 46 (^{14}C , ^{16}O , ^{18}O or ^{13}C , ^{17}O , ^{16}O or ^{12}C , $^{17}\text{O}_2$) are then counted by the detectors. Furthermore, the isotope ratio mass spectrometer (IRMS) uses this to determine the mass ratios 45/44 and 46/44. The final results obtained are $\delta^{18}\text{O}$ and $\delta^{13}\text{C}$ relative to VPDB. A correction for the ^{17}O content in the sample is applied (Rohling and Cooke, 1999). Because of a dual-inlet system, the mass spectrometer can alternately measure isotopic ratios in the sample and a working standard, avoiding extreme fractionation during ionization in the source (Clark and Fritz, 1997).

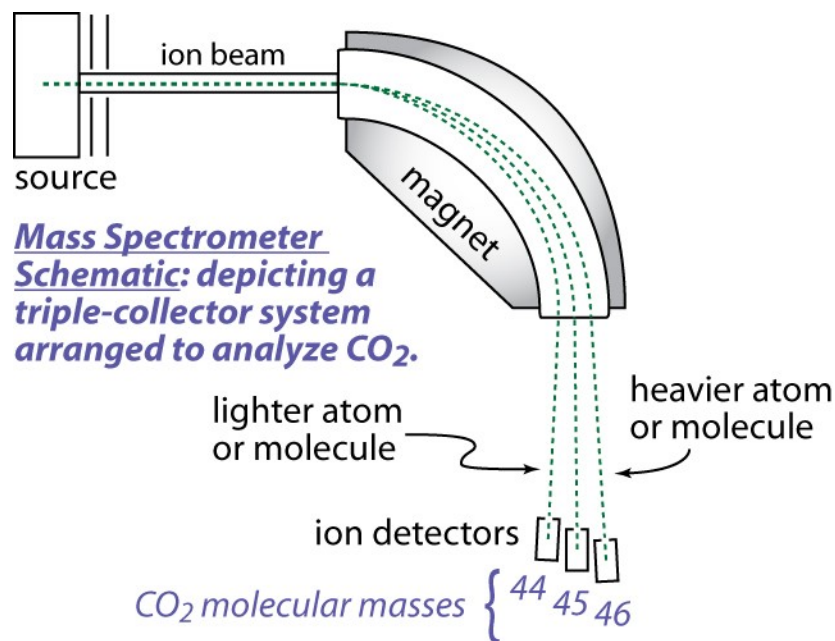


Figure 4.1: Schematic illustration of a gas source mass spectrometer showing the three parts discussed in the text; the ion source, the mass analyser (magnet) and the detector (Dunn, 2016).

Connected to the mass spectrometer is the Kiel IV Carbonate device. This device ensures direct injection of CO₂ into the mass spectrometer. The CO₂ gas is produced when phosphoric acid reacts with carbonate at ~70°C as explained in Equation 4.1.

4.3.1 Standards

It is exceedingly difficult and time consuming to accurately determine the absolute abundance of minor isotopes, such as ¹⁸O or ¹³C. However, by comparing results in a given sample to a known external standard a quantitative estimate can be achieved.

The internationally accepted standard, provided by the International Atomic Energy Agency (IAEA), that is used for both oxygen and carbon in carbonates was originally a fossil Belemnite from the Cretaceous Pee Dee formation (PDB) in South Carolina (Urey et al., 1951) defined as $\delta^{18}\text{O} = 0$ and $\delta^{13}\text{C} = 0$ (Epstein et al., 1953). This sample is now depleted and has been replaced by Vienna Pee Dee Belemnite (VPDB), defined by the IAEA.

Laboratories develop their own working standard which is calibrated to a reference standard defined by the National Institute of Standards and Technology (NIST) or IAEA. The working standard used in this study is the Carrara Marble 12 (CM12). When preparing for the mass spectrometer the CM12 standards are weighed. The preferred standard weight is in the range of the sample weights, both heavier and lighter. Based on replicate measurements of CM12 the long-term analytical precision for Finnegan MAT253 is reported to be $\pm 0.08\text{‰}$ and $\pm 0.03\text{‰}$ for $\delta^{18}\text{O}$ and $\delta^{13}\text{C}$, respectively. CM12 is calibrated to the VPDB scale using the international reference standard National Bureau of Standards-19 (NBS19) which has a fixed and known value related to VPDB (NBS-19; $\delta^{13}\text{C}_{\text{VPDB}} = 1.95\text{‰}$ and $\delta^{18}\text{O}_{\text{VPDB}} = -2.2\text{‰}$). In addition, the National Bureau of Standards-18 (NSB-18; $\delta^{13}\text{C}_{\text{VPDB}} = -5.014\text{‰}$ and $\delta^{18}\text{O}_{\text{VPDB}} = -23.2\text{‰}$), provided by the IAEA (2009) was used for calibration.

4.4 Climate proxies

In this subchapter a short theoretical background of the different climate proxies used in this thesis will be given.

4.4.1 Stable isotopes

Stable isotope ratios (e.g. $^{18}\text{O}/^{16}\text{O}$ and $^{13}\text{C}/^{12}\text{C}$) are widely applied proxies used to extract past climate parameters from a broad range of materials and archives. Isotopes are atoms with a nucleus containing the same number of protons but a different number of neutrons, and hence a different atomic mass. If they are not radioactive, they are considered to be stable isotopes.

The utility of stable isotopes as a proxy derives from the idea that the ratio of heavy to light isotopes in a material is controlled by a range of different variables, and among them are climate related variables such as ice volume, ocean temperature, hydrography, atmospheric temperature and moisture source (Cronin, 2010). Stable isotope analyses have played a fundamental role in paleoceanography since the early, pioneering works of Emiliani (1955) who, building on work of Urey (1947), McCrea (1950) and Epstein et al. (1953), constructed a series of Pleistocene climate and temperature cycles using isotopic records from marine sediment cores. Later, Shackleton and Opdyke (1973) produced an isotopic stratigraphy correlated with magnetic stratigraphy, dated 22 isotopic stages, and also used benthonic foraminifera to show that the $\delta^{18}\text{O}$ signal primarily demonstrates fluctuations of the global ice volume and that temperature plays a secondary role. This discovery further triggered a widespread use of $\delta^{18}\text{O}$ records for stratigraphy and studies of past ice volume and sea level variations. Shackleton (1977) later demonstrated that $\delta^{13}\text{C}$ variations could be valuable for studying water mass movement and proposed a connection between climatically induced changes in parts of the biosphere and the flux of dissolved CO_2 in the oceans. With the ongoing efforts of several scientists a detailed age control for $\delta^{18}\text{O}$ records around the world has been established and oxygen isotope records have not only evolved into a global correlation tool but are also a recognized and widely used dating tool (Rohling and Cooke, 1999).

Separation of isotopes between substances and differential uptake of heavy or lighter isotopes during formation or break down of chemical compounds is called fractionation. Isotopic fractionation occurs in all thermodynamic reactions because of varying reaction rates for different molecular species (Clark and Fritz, 1997). Fractionation cause a disproportionate

concentration of one isotope over the other on one side of the reaction. Fractionation occurs because of two different isotopic chemical reactions; equilibrium processes (mainly temperature dependent) and kinetic effects (non-equilibrium processes) (Rohling and Cooke, 1999). For example, if R_A and R_B are the heavy and light versions for any two isotopes (e.g. $^{18}\text{O}/^{16}\text{O}$ or $^{13}\text{C}/^{12}\text{C}$), then the isotopic fractionation factor (α) is defined as the isotopic ratios in one substance or phase (A) divided by the isotopic ratios in another substance or phase (B):

$$\alpha_{A-B} = R_A/R_B \quad \text{Equation 4.2 (Rohling and Cooke, 1999)}$$

$$\text{e.g. } \alpha_{\text{O}} = \frac{(^{18}\text{O}/^{16}\text{O})_{\text{carbonate}}}{(^{18}\text{O}/^{16}\text{O})_{\text{CO}_2}}$$

Oxygen isotopes

Oxygen occurs naturally in three variations; ^{16}O (99.76%), ^{17}O (0.04%) and ^{18}O (0.20%) (Cronin, 2010). It is exceedingly difficult to precisely and accurately determine the absolute abundance of minor isotopes, such as oxygen isotopes. Instead isotopic ratios, which are much easier to determine, are reported as deviations from a reference sample, a standard with known isotopic value. In the global hydrological cycle, ratios of ^{18}O and ^{16}O vary as they are transferred through the climate system and the $^{18}\text{O}/^{16}\text{O}$ is the ratio that is most commonly used in paleoclimate research, given by the higher abundances and greatest mass difference. The reported $^{18}\text{O}/^{16}\text{O}$ values are given in dimension-less delta (δ) notation and in parts per mill (‰), defined in Equation 4.3:

$$\delta^{18}\text{O} (\text{‰}) = 1000 \times \frac{^{18}\text{O}/^{16}\text{O}_{\text{sample}} - ^{18}\text{O}/^{16}\text{O}_{\text{standard}}}{^{18}\text{O}/^{16}\text{O}_{\text{standard}}} \quad \text{Equation 4.3}$$

$\delta^{18}\text{O}$ is closely linked to the hydrological cycle that involves evaporation, atmospheric water vapour transport and the return of freshwater to the ocean through precipitation, runoff and/or iceberg melting (Rohling and Cooke, 1999). Foraminifera that live in the ocean and grow in equilibrium with the surrounding seawater incorporate the isotopic values and temperature of the seawater in their calcium carbonate shells. If the species secretes its shell in thermodynamic equilibrium with the surrounding seawater and if other influences are equal, the greater the temperature of the seawater, the less enriched the foraminifera $\delta^{18}\text{O}$ will be (Cronin, 2010). However, the $\delta^{18}\text{O}$ is also affected by the global ice volume stored in continental ice sheets. When water evaporates from the ocean (or lakes and rivers) lighter molecules are preferentially

moved to the vapour phase due to higher vapour pressures. Such preferential uptake of lighter isotopes (^{16}O) during evaporation relatively increase the $\delta^{18}\text{O}$ in the remaining surface water (Figure 4.2). Hence, precipitation that build up ice sheets preferentially consists of more ^{16}O than ^{18}O . This precipitation depleted in $\delta^{18}\text{O}$ that falls over areas where ice sheets are built up will be long term stored in the ice sheet. This causes two delay processes: (1) icebergs calving off marine terminating ice sheets import freshwater with older (more negative ^{18}O) isotopic values to the ocean surface waters (ice could be 100,000 – 400,000 years old). (2) Aquifers, can also contain old isotopic values (up to 35,000 years old) and distribute this to the ocean (Rohling and Cooke, 1999). Seasonal sea ice formation will affect the $\delta^{18}\text{O}$ in local areas, while the $\delta^{18}\text{O}$ distribution in oceans will mainly depend on advection and mixing of water masses from different source regions (Rohling and Cooke, 1999).

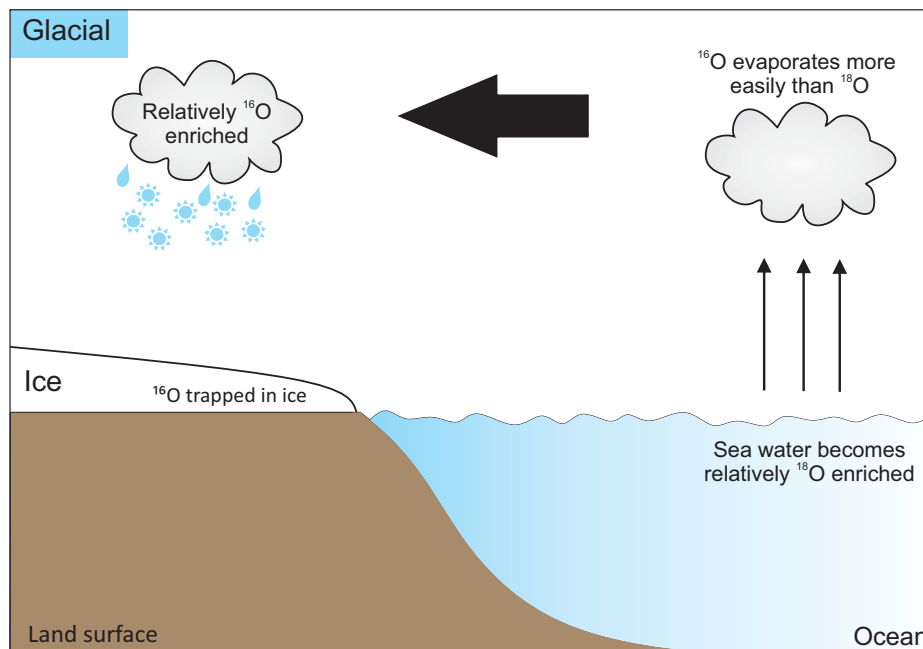


Figure 4.2: Simplified schematic illustration of oxygen isotope fractionation during a cold (glacial) climate state. During glacials, proportionally more ^{16}O is trapped in ice, leaving the remaining sea water relatively ^{18}O enriched and $\delta^{18}\text{O}$ values positive. During interglacials, the global ice volume decreases and proportionally more ^{16}O exists in the seawater. Hence, interglacial seawater $\delta^{18}\text{O}$ is isotopically more negative (illustration by S. Rutledal).

The isotopic composition measured in foraminifera shells are both reflecting the isotopic composition and the temperature in the surrounding ocean water. Harold C. Urey and his team (1947) demonstrated that there is a correlation between the temperature at which the marine organisms grow and the $\delta^{18}\text{O}$ abundance in their calcium carbonate shells (Urey, 1947). This discovery of temperature dependent isotope fractionation triggered the development of

“isotopic paleothermometers” or “paleotemperature equations”, where isotopic measurements in foraminifera calcium carbonate were used as a proxy for reconstructing paleotemperatures in past oceans. Building on work of Urey, Samuel Epstein and co-workers (1953) developed such a paleotemperature equation (Equation 4.4) based on mollusc shells, expressing the relationship between the temperature (T), the $\delta^{18}\text{O}$ of the sample (δ_c) and the $\delta^{18}\text{O}$ of the sea water (δ_w), relative to VPDB. Later this equation has been slightly modified by Shackleton (1974) using experimental data from O'Neil et al. (1969) improving the precision in the low temperature domain (<10°C).

$T (^{\circ}\text{C}) = 16.9 - 4.38(\delta_c - A) + 0.10(\delta_c - A)^2$, $A = \delta_w - 0.27\text{‰}$ Equation 4.4 (Epstein et al., 1953; Shackleton, 1974).

The offset value of -0.27‰ accounts for the equation specific conversion from Vienna Standard Mean Ocean Water (VSMOW) to VPDB.

The paleotemperature equation provided by Epstein et al. (1953) assumes that the $\delta^{18}\text{O}$ of seawater is known. However, this is only true for the present, and not for the past. The $\delta^{18}\text{O}$ of seawater in the past has been greatly influenced by changes in ice volume. During glacial periods, seawater $\delta^{18}\text{O}$ was substantially higher compared to the interglacial periods due to the preferential removal of ^{16}O from the ocean when building ice sheets. In addition, precipitation and atmospheric vapour transport affect the global $\delta^{18}\text{O}$ of sea water. The isotopic composition of the first precipitation remain similar to that of the original seawater. However, with increasing distance from the source region and progressively more rain out the $\delta^{18}\text{O}$ signal will be depleted. In addition, when travelling into the high-latitudes where the temperature decreases, the moisture content of the air mass drops and becomes more $\delta^{18}\text{O}$ depleted. Subsequently, precipitation in the high latitudes are more depleted in $\delta^{18}\text{O}$ than precipitation in the tropics, potentially affecting the isotopic composition in the high – and low-latitude oceans (Rohling and Cooke, 1999).

The paleotemperature equation assumes calcification in chemical equilibrium with the surrounding seawater. However, there are several factors that may cause deviations from equilibrium such as the ontogenic effect, symbiont photosynthesis, respiration effects, gametonic calcite effects and changes in CO_3^{2-} . All of these effects are important for planktonic foraminifera, but deviations from equilibrium also exist in benthonic foraminifera. In addition,

temperature varies with regards to depth in the surface ocean and vertical migration of species may cause deviations from equilibrium (Rohling and Cooke, 1999). Despite these possible shortcomings, modifications of Epstein's paleotemperature equation has been of great value in the field of paleoceanography and paleoclimatology.

Carbon isotopes

There are two naturally occurring, stable carbon isotopes: ^{12}C (98,89%) and ^{13}C (1,11%). ^{14}C is a radioactive variation of carbon, and is a commonly used dating tool for <50,000 years old sediments containing organic matter. Fractionation between the two stable isotopes, ^{12}C and ^{13}C , has become an established tool in paleoceanography for describing paleoproductivity, CO_2 fluxes and water mass movements in the geological past. As for oxygen isotopes, carbon isotope ratios are reported in δ -notation and as deviations from a standard (Equation 4.5).

$$\delta_{^{13}\text{C}} \text{‰} = 1000 \times \frac{^{13}\text{C}/^{12}\text{C}_{\text{sam}} - ^{13}\text{C}/^{12}\text{C}_{\text{std}}}{^{13}\text{C}/^{12}\text{C}_{\text{std}}} \quad \text{Equation 4.5}$$

On Earth, there are two main carbon reservoirs; organic and inorganic (sedimentary) carbon. The inorganic carbon in oceans is governed by carbonate reactions. Most of the CO_2 in water is stored in HCO_3^- and the total dissolved inorganic carbon (DIC) consists of HCO_3^- , CO_3^{2-} and dissolved CO_2 (Rohling and Cooke, 1999). Foraminifera precipitate their shells in close relation to the $\delta^{13}\text{C}_{(\text{DIC})}$ (Rohling and Cooke, 1999). The concentration and distribution of $\delta^{13}\text{C}_{(\text{DIC})}$ in the ocean is governed by different factors. Primarily by photosynthesis and remineralisation of organic carbon, but also by mixing different water masses with different isotopic compositions (Curry et al., 1988). The importance of these factors varies with location and must be examined for each ocean basin.

Marine organisms living in the surface water sequester carbon through photosynthesis. In general, there is a preferential uptake of the lighter isotope ^{12}C and the remaining CO_2 in the surface water is enriched in ^{13}C (Rohling and Cooke, 1999). In addition, nutrients are also consumed by the organisms, leaving the surface water nutrient depleted. Commonly, phosphate (PO_4) concentrations are used as a nutrient proxy, and has an inverse relationship with $\delta^{13}\text{C}$ (high $\delta^{13}\text{C}$, low PO_4). When these organisms die, and remineralise in the deep ocean a transfer of ^{12}C occurs from the surface to the deep water and the deep ocean becomes $\delta^{13}\text{C}$ depleted (Figure 4.3). An increasing gradient between $\delta^{13}\text{C}$ enrichment in the surface and $\delta^{13}\text{C}$ depletion

in the deep indicates an increase in export productivity, sometimes referred to as the biological pump, which in turn can be observed in certain species of benthic foraminifera. During remineralisation of organic matter in the deep, nutrients are also released. Consequently, depleted $\delta^{13}\text{C}$ values correlate well with enhanced nutrient concentrations.

$\delta^{13}\text{C}_{(\text{DIC})}$ in the ocean is influenced by the carbon cycle and the distribution of carbon between the ocean, atmosphere and terrestrial biosphere reservoirs. The photosynthesis's preferential uptake of ^{12}C creates a terrestrial biosphere that is depleted in ^{13}C , while the ocean and atmosphere are enriched in ^{13}C . Ocean and atmosphere $\delta^{13}\text{C}$ values are also influenced by other geological factors such as gas hydrates, volcanic outgassing, increased weathering etc. (Hillaire-Marcel and Ravelo, 2007).

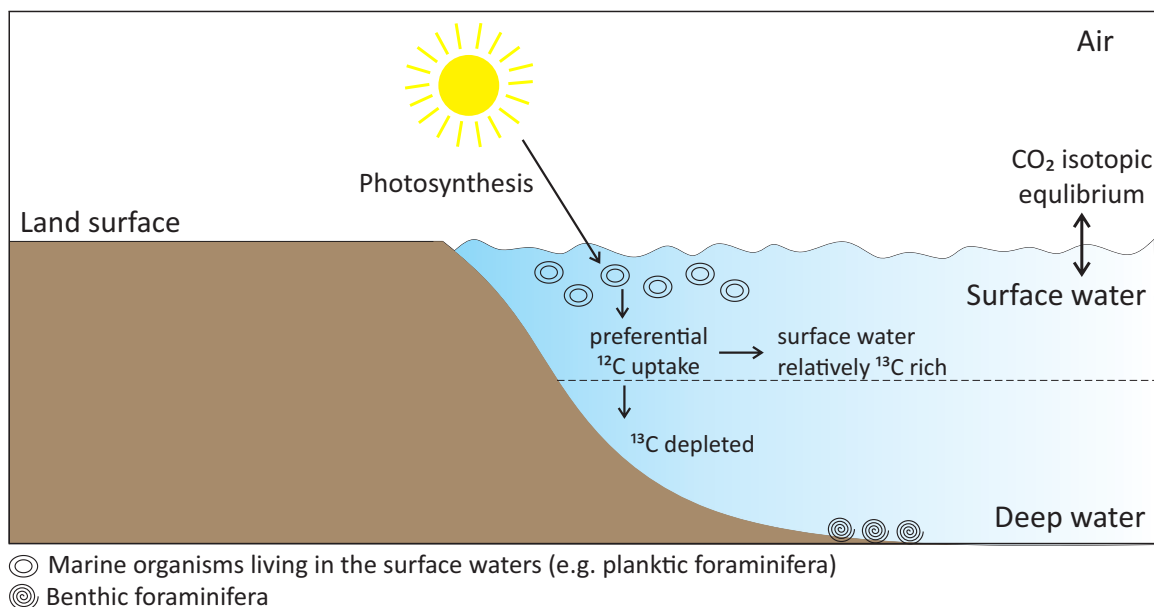


Figure 4.3: Simplified illustration of the carbon isotope transfer in the ocean, in high productive areas. A carbon isotope gradient between the sea surface and deep water develop due to export production and interactions between the marine organic and inorganic carbon cycles. ^{13}C is depleted in the deep and ^{13}C enriched at the surface (illustration by S. Rutledal).

Deep water forms in the high-latitudes, after physical processes increase the surface water density, causing it to sink. This high-latitude surface water transfers its isotopic and nutrient properties to the deep. The initial carbon isotopic composition of this water mass is determined by the extent of photosynthesis that has occurred when it existed in the photic zone (Curry et al., 1988). After leaving the surface and sinking to the deep ocean, exiting the photic zone, there are only two processes that can alter the $\delta^{13}\text{C}$ properties of the water; remineralisation of carbon

and mixing with other water masses containing different isotopic values. In the Atlantic, the rates of production and degradation of organic carbon are so low, that $\delta^{13}\text{C}$ can be used as a tracer for deep ocean masses (Curry et al., 1988).

NADW has high $\delta^{13}\text{C}_{(\text{DIC})}$ values and is the most nutrient depleted deep water mass in the ocean today, due to its surface water source. The surface water that sinks to form NADW originate in the tropics and subtropics where extensive photosynthesis and productivity depletes the water of nutrients and ^{12}C . When this surface water mass travels northward and sinks to form NADW it is $\delta^{13}\text{C}_{(\text{DIC})}$ enriched, with values of ~ 1.2 (VPDB) ‰ (Eide et al., 2017). The other main deep water mass in the Atlantic, AABW has relatively low $\delta^{13}\text{C}_{(\text{DIC})}$ values (~ 0.2 (VPDB) ‰ (Eide et al., 2017)) due to mixing between surface Southern Ocean water and deep water from other basins, with low $\delta^{13}\text{C}_{(\text{DIC})}$ values. NADW (high $\delta^{13}\text{C}_{(\text{DIC})}$, nutrient depleted) flowing from north to south Atlantic and AABW (low $\delta^{13}\text{C}_{(\text{DIC})}$, nutrient enriched) flowing from south to north Atlantic results in a strong gradient in the deep Atlantic Basin (Hillaire-Marcel and Ravelo, 2007). Hence, given the characteristic $\delta^{13}\text{C}_{(\text{DIC})}$ and nutrient properties of deep water masses in the Atlantic basin, isotope records extracted from benthonic foraminifera are a useful tool to trace the pathways and variability of the deep ocean currents in the Atlantic.

4.4.2 Ice Rafted Debris (IRD)

Marine calving of ice sheets and glaciers, and the subsequent melting of icebergs are a source of distinct sediments in open ocean environments known as ice rafted debris (IRD). Sea ice that is transported by ocean currents can also deposit layers of IRD. High summer insolation causes meltwater discharge from the ice sheets into the ocean which enhances sea ice formation during winter. On the other hand, high winter insolation increases the growth of continental ice sheets, which increase glacial flow and potentially make the ice sheets more unstable (Heinrich, 1988). This enhances iceberg formation and reduce the salinity in the surface ocean waters. The amount of ice rafted material deposited in marine sediment cores provides a framework for constraining climate change in the North Atlantic Ocean, but is also a frequently used index for glacial activity in the Pacific Ocean and around the Antarctic (Heinrich, 1988). The discovery of irregular IRD rich layers in Atlantic sediment cores led to the detection of Heinrich-events, associated with short-lived abrupt intervals of increased iceberg discharge and freshwater flux. The nature of Heinrich-events was further confirmed through other proxies such as high concentrations of detrital carbonate (Bond and Lotti, 1995) and decreases in foraminifera

abundance coinciding with increases in IRD (Hemming, 2004). However, the IRD method is not without complications. The debris in a glacier is usually concentrated in a 1-3 m layer at the base, and if present in icebergs, this layer typically melts off during the first 10-100 km of transport from the ice margin. IRD is commonly defined as the weight percentage of grains per gram within a certain size fraction (e.g. $>250\ \mu\text{m}$, $>150\ \mu\text{m}$ $>63\ \mu\text{m}$), and a common assumption is that the selection of size fraction does not bias the result (e.g. (Ruddiman, 1977; Heinrich, 1988)). However, studies have shown little correlation between the weight percentage of IRD in the different size fractions (e.g. (Andrews, 1985; 2000)). In addition, the main portion of the sediments transported by icebergs are in the silt and clay size fraction (Andrews, 2000). Consequently, any interpretation of abrupt IRD changes in marine sediment cores must consider these complexities and limitations contained within IRD-signals when determining the origin of an event. On the other hand, in many cases the IRD signals show widespread coherence and have become an important correlation tool between sediment cores. Figure 4.4 show a photo of a typical IRD-rich layer (sample 120 cm from the core GS15-196-02GC).

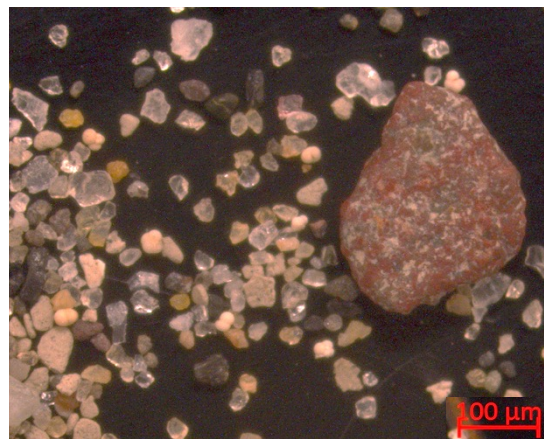


Figure 4.4: Photo with IRD from core GS15-196-02GC (120cm), scale in bottom right corner. (Photo: S. Rutledal).

Studies on iceberg trajectories in the North Atlantic show that the IRD found at the core site could originate from different areas and ice sheets (Ruddiman, 1977). The IRD rich Heinrich-layers mainly originate from the North American Laurentide Ice sheet discharging icebergs through the Hudson Strait. However, some Heinrich-layers show an Arctic/European/Greenland/Iceland source (Bond and Lotti, 1995; Grousset et al., 2001; Darby et al., 2002). The IRD deposited at the study site during the last glaciation is most likely from the Greenland, Icelandic, Faroe Island or Eurasian ice sheets, as well as derived from sea ice in the Arctic region transported by the EGC (Figure 4.5) (Ruddiman, 1977).

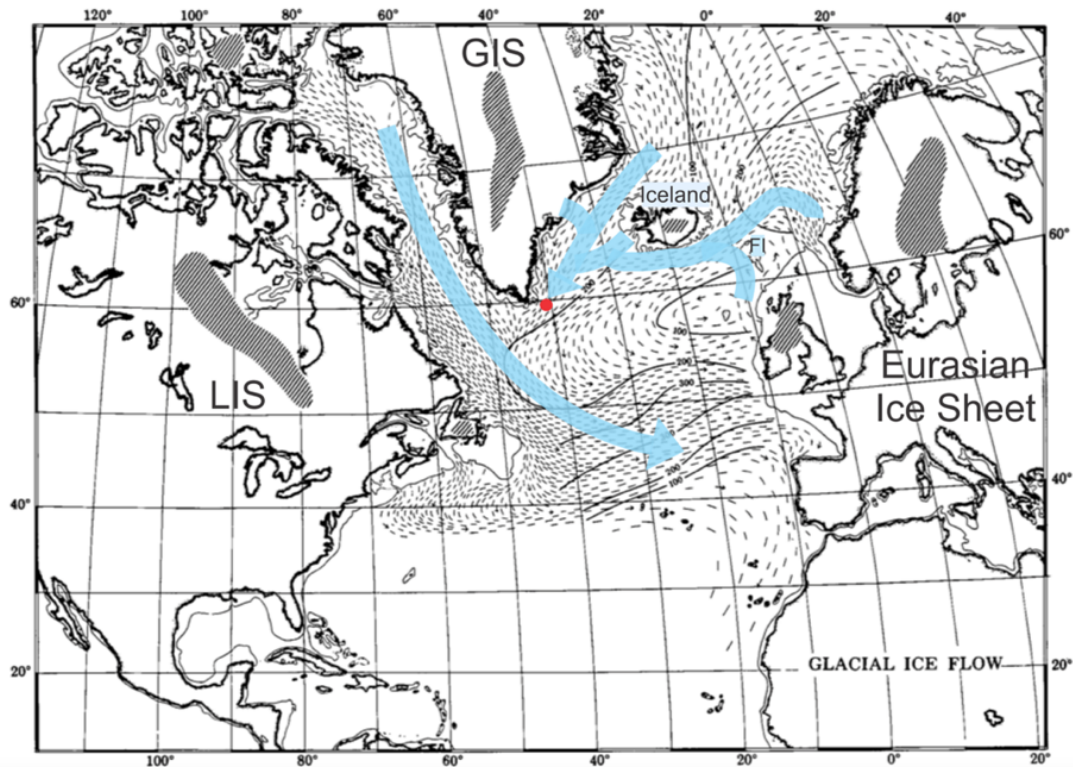


Figure 4.5: Map of the main paths of IRD distribution during a glacial world. Grey shaded areas mark the spreading centers of the continental ice sheets. Blue arrows denote the main IRD paths passing through (and/or close to) the core site. Red circle denotes the core site (GS15-196-02GC). GIS=Greenland Ice Sheet, LIS=Laurentide Ice sheet, FI=Faroe Islands. Modified from Ruddiman (1977).

4.5 Foraminifera

Foraminifera are single celled protozoa that live either among the marine plankton or on the sea floor. Foraminifera are found in the geological record from early Cambrian to modern times (Armstrong and Brasier, 2009). They live in a range of different environments and their ecological sensitivity makes them useful in present and paleoclimate studies. Previous studies of foraminifera have been used to describe Quaternary climate cycles (Hillaire-Marcel and de Vernal, 2007) and laid the foundation for reconstructing the Earth surface at the time of the last glacial maximum (e.g. CLIMAP members (1976)).

The foraminifer shell may consist of organic matter, secreted minerals such as calcite, aragonite and silica or agglutinated particles. Foraminifera with calcareous shells incorporate the oxygen and carbon isotope composition and temperature in the surrounding water during calcification. This isotopic data can be extracted and calibrated to reconstruct past seawater chemistry and biogeochemical cycles (Hillaire-Marcel and de Vernal, 2007).

4.5.1 Planktonic foraminifera

Planktonic foraminifera float at different water depths in the upper water column depending on the species, but preferably close to the surface (Ruddiman, 2014). For this study, stable isotope analysis was carried out on one planktonic species: *Neogloboquadrina pachyderma* sinistral.

Neogloboquadrina pachyderma (Ehrenberg, 1861)

N. pachyderma can either have a chamber coiled in the right (dextral) or left (sinistral) direction. The preferred coiling direction is believed to be controlled by the temperature of the seawater. *N. pachyderma* with sinistral coiled shells dominate the polar waters in both hemispheres, whilst *N. pachyderma* with dextral coiled shells (or *N. incompta*) are most abundant in subpolar and temperate waters (Darling et al., 2006). However, a small percentage of right coiling *N. pachyderma* can appear in polar waters (Pflaumann et al., 1996). North of 70°N, the $\delta^{18}\text{O}$ of both dextral and sinistral variations are largely the same. However, in the region of the Denmark Strait and Norwegian Sea, south of 64°N, the dextral variation is genotypic and highly distinct from the left variation (Bauch et al., 2003). For this reason, the two variations should be considered different species and for this study only *N. pachyderma* (sinistral) (Figure 4.6) was selected.



Figure 4.6. Photo of *N. pachyderma* (s) from core GS15-196-02GC (28cm), scale in the bottom right corner (Photo: S. Rutledal).

N. pachyderma (s) is a common species in the surface water in polar regions (Kipp, 1976) and covers more than 90% of the marine surface sediment assemblage in the areas north of the Arctic front in the Greenland, Iceland and Norwegian Seas (Pflaumann et al., 1996). Thus, making it a very useful ecological and geochemical proxy of past polar oceans. The blooming

season of *N. pachyderma* (s) in polar waters is limited to ice free conditions and peaks in the summer season (July-September) (Schiebel and Hemleben, 2005). In the Irminger Sea maximum *N. pachyderma* (s) flux occurs during the spring and in late summer, during minimum and maximum stratification, respectively (Jonkers et al., 2010). Thus, since the population size of *N. pachyderma* (s) varies throughout the year, the signal retrieved from the foraminifera shell is bias towards that period of the year of with highest production rates. For example, north of 30°, during Heinrich 1, maximum production occurred up to 6 months later in the year compared to LGM (Kretschmer et al., 2016). These findings confirm the species sensitivity to seasonal changes in sea ice extent and food supply, and that paleoceanographic reconstructions of ocean surface properties (from $\delta^{18}\text{O}$) during this time might be bias and in some cases underestimated due to a shift in the time of maximum production.

Under normal salinity (33-36‰) conditions, planktonic foraminifera do not seem to be affected by salinity. However, *N. pachyderma* (s) is known to avoid low salinity layers (<32‰) in the Arctic (Hillaire-Marcel and de Vernal, 2007). There is some disagreement as to which water depth *N. pachyderma* (s) calcifies at. Because of the species encrustation potential, it has been classified as a deep planktonic species by many scientists and is expected to grow below 200 m water depth (Hemleben et al., 1989). However, a study from the northeast water polynya off the east Greenland coast found that the maximum abundance of *N. pachyderma* (s) grows and lives at depths of 20-80 m, in the zone associated with maximum chlorophyll (Kohfeld et al., 1996). Another study from the Nansen Basin in the Arctic infer that *N. pachyderma* (s) prefers habitat depths between 100-200 m (Bauch et al., 1997). The variations in the preferred depth habitat of *N. pachyderma* (s) have led to the suggestion that the depth habitat of this species is probably not based only on the optimal salinity or temperature range, but instead it is to a greater extent controlled by the food and light supply (Bauch et al., 1997). Hence, *N. pachyderma* (s) live in a thick part of the upper water column and not just in the uppermost surface. Lastly, a study from the Nordic Seas show that in the western part of the basin, close to Greenland, *N. pachyderma* (s) prefers a relatively deep habitat of 70-130 m, which is below the halocline related to the EGC (Simstich et al., 2003). Nevertheless, $\delta^{18}\text{O}$ changes recorded in *N. pachyderma* (s) can reveal significant climate changes, because a relatively large part of the upper water column is affected, causing little to no regional and seasonal signal disturbances. In conclusion, despite the complexity of establishing its exact depth habitat in the water column, the species has proven to be a very good and reliable proxy for water mass changes (Bauch et al., 1997; Jonkers et al., 2010).

In past studies, correlation between *N. pachyderma* (s) abundance and stable isotope chemistry in North Atlantic sediment cores correlated with $\delta^{18}\text{O}$ changes in Greenland Ice cores has been used to characterize millennial scale climate changes and demonstrates that the North Atlantic surface ocean and atmosphere are connected (Bond et al. (1993); McManus et al. (1994); Oppo and Lehman (1995)). Furthermore, *N. pachyderma* (s) $\delta^{18}\text{O}$ have been used to trace meltwater pulses (e.g. Heinrich events (Bond et al., 1992) and 8.2 ka event (Kleiven et al., 2008)). Additionally, $\delta^{13}\text{C}$ and $\delta^{18}\text{O}$ isotopes in *N. pachyderma* (s) have been used to define a link between the surface, intermediate and deep water ocean circulation (Kohfeld et al., 1996).

4.5.2 Benthonic foraminifera

Benthonic (bottom-dwelling) foraminifera are found in a range of different environments. They can live both in substrate above the sediment surface, in the surface/sediment zone and within the sediment where they move up and down (up to 10 cm down) in the sediments depending on food supply (Linke and Lutze, 1993).

The ocean floor is relatively stable and therefore, deep-sea foraminifera assemblages are expected to contain little short-term variability (Goody and Rathburn, 1999) and little to no variance due to short-term changes in temperature and salinity. Benthonic $\delta^{13}\text{C}$ records have been used to determined deep water (e.g. NADW) response to Dansgaard-Oeschger cycles and Heinrich events (e.g. (Oppo and Lehman, 1995; Henry et al., 2016)). Studies on benthonic foraminifera have also been used to reconstruct changes in deep water circulation patterns and intensity (e.g. (Boyle and Keigwin, 1985; Curry et al., 1988; Duplessy et al., 1988; Boyle, 1992; Curry and Oppo, 2005)) and have revealed dramatic changes in the ocean circulation patterns and carbon chemistry over interglacial-glacial timescales in the late Quaternary.

In this study, stable isotope analysis was carried out on one benthonic species; *Cibicidoides wuellerstorfi*.

Cibicidoides wuellerstorfi (Schwinger, 1866)

In general, the species *C. wuellerstorfi* (Figure 4.7) have been used for deep water $\delta^{13}\text{C}$ reconstructions and several studies have shown that *C. wuellerstorfi* $\delta^{13}\text{C}$ reflect large scale bottom water variations in the modern world oceans (e.g. (McCorkle and Keigwin, 1994)).

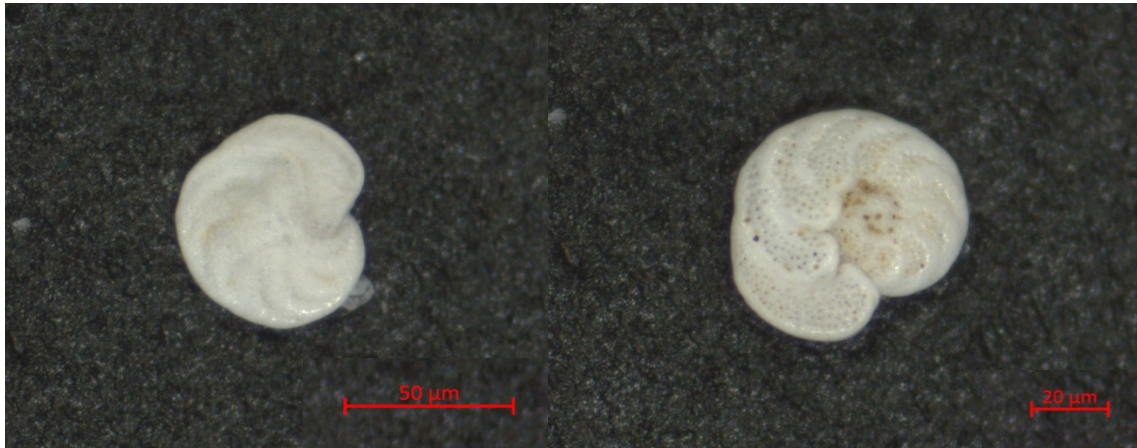


Figure 4.7: Photo of *C. wuellerstorfi* from core GS15-196-02GC (24cm), front (left) and back (right). Scale in the bottom corners (Photo: S. Rutledal).

The species prefer to live in an epibenthonic or elevated position on and above the sediment surface (Lutze and Thiel, 1989). However, some populations have been found to live within soft sediments, suggesting that not all *C. wuellerstorfi* secrete their shells at the sediment-water zone (e.g. (Corliss, 1991; McCorkle et al., 1997)). *C. wuellerstorfi* that live on elevated surfaces secrete their shells in equilibrium with the ambient bottom water, without influence from sediment pore water chemistry. However, the population of the species that live within the sediments, can be influenced by the microenvironments, so that the secreted shells reflect both bottom water and pore water chemistry. Mackensen et al. (1993) suggest that in regions with high phytodetritus deposits, the release of $\delta^{13}\text{C}$ depleted CO_2 during organic matter dissolution may lead to the development of a strong $\delta^{13}\text{C}$ gradient above the sediment-water interface. This can further influence the isotopic composition of epifaunal foraminifera if calcification takes place when a strong $\delta^{13}\text{C}$ gradient exists. Furthermore, this leads to the suggestion that in some areas *C. wuellerstorfi* shell production is limited to a very short period of the year, when the organic flux is at its maximum. The resulting isotopic composition of the *C. wuellerstorfi* may then represent only short periods of time and not an average, long-term isotopic composition of the bottom water (Jorissen and Wittling, 1999). However, in general, the $\delta^{13}\text{C}$ values of *C. wuellerstorfi* are in or near equilibrium with $\delta^{13}\text{C}_{\text{DIC}}$, apart from areas with extremely high productivity.

Despite these possible shortcomings, *C. wuellerstorfi* is considered as the best foraminifer species for recording deep water $\delta^{13}\text{C}_{\text{(DIC)}}$ (Duplessy et al., 1984). The $\delta^{13}\text{C}$ signal observed in *C. wuellerstorfi* reflect glacial and interglacial cycles, with low $\delta^{13}\text{C}$ values during glacials and

higher values during interglacials. In addition, variability in $\delta^{13}\text{C}$ of *C. wuellerstorfi* reflect, in part, changes in the bottom-water chemistry, which can be related to the source and mode of deep water formation (Cronin, 2010), and therefore may be used to reconstruct the distribution of different water masses in the past. The species is dominant in areas bathed by NADW (Sen Gupta, 1999) and scientists agree that fluctuations in the abundance of *C. wuellerstorfi* are likely related to temporal changes in the advection of NADW (Schmiedl and Mackensen, 1997).

5. CHRONOLOGY

5.1 Dating method

Seven samples of approximately 5.0 mg of *N. pachyderma* (s) were sent for Radiocarbon ^{14}C dating at the AMS Laboratory, Eidgenössische Technische Hochschule (ETH) in Zürich.

5.1.1 AMS Radiocarbon ^{14}C dating

There are three naturally occurring isotopes of carbon; ^{12}C (98.89%), ^{13}C (1.11%) and ^{14}C (one part in $10^{10}\%$) (Walker, 2005). ^{12}C and ^{13}C are stable isotopes, while ^{14}C is unstable and considered radioactive and decays to a stable form of nitrogen (^{14}N).

Interactions between cosmic ray neutrons and nitrogen in the upper atmosphere lead to the formation of ^{14}C atoms ($n + ^{14}\text{N} \rightarrow ^{14}\text{C} + p$). When these ^{14}C atoms combine with oxygen to form $^{14}\text{CO}_2$, which further mixes with the non-radioactive form of carbon dioxide (CO_2), ^{14}C becomes part of the global carbon cycle and is absorbed by plants through photosynthesis. Approximately 95% of the ^{14}C in the global carbon cycle is absorbed by the ocean as dissolved carbonate, which in turn is absorbed by organisms living in the sea water, such as foraminifera. Even though ^{14}C in the terrestrial biosphere and oceans is constantly decaying, the amount of ^{14}C stored in plants, animals and the ocean remains constant due to continual replenishment of ^{14}C from the atmosphere. Hence, the ^{14}C in the terrestrial biosphere and the surface oceans is in isotopic equilibrium with the atmosphere (Walker, 2005).

When an organism dies, replenishment of ^{14}C from the atmosphere stops and ^{14}C decays to ^{14}N at a constant and known rate. Consequently, measuring the remaining amount of ^{14}C in organic material and comparing this to modern ^{14}C in a standard material can reveal the age of the organic material. The half-life of a ^{14}C atom is 5730 years (Godwin, 1962) and generally the dating method is valid for eight half-lives, approximately 45,000 years.

However, when converting ^{14}C -activity to calendar age several assumptions are made, some of which causes uncertainties. The method assumes constant atmospheric ^{14}C levels over time, although, studies have found a fluctuation in ^{14}C activity in the atmosphere in the past (Beck et al., 2001; Hughen et al., 2004). Factors producing these ^{14}C variations in the atmosphere include modulation of the cosmic ray flux, variations in the solar activity and changes in ocean ventilation and deep water formation, affecting the amount of ^{14}C depleted oceanic CO_2

released into the atmosphere. Furthermore, human activity has affected atmospheric ^{14}C over the past 250 years (Olsen and Ninnemann, 2010). Moreover, the different carbon reservoirs are not always in isotopic equilibrium with the atmosphere. In the oceans, once the surface water sinks to become intermediate and deep water, ^{14}C decays without replenishment from the surface, producing an apparent age, referred to as “the reservoir effect”. The effect varies in the different ocean basins and is estimated to be approximately 400 years in the North Atlantic (Bard et al., 1991), which have to be corrected for. Furthermore, because of the circulation of water masses in the ocean, more localized variations may occur. Deep water is depleted in ^{14}C because of no contact with the atmosphere and in upwelling areas this water mixes with modern surface water, causing an apparent age, which varies with the geographical location. Lastly, isotopic fractionation between the three isotopes ^{12}C , ^{13}C and ^{14}C must also be considered (Walker, 2005). Due to these factors, radiocarbon dates do not directly correlate to calendar years. However, because of the development of radiocarbon calibration tools, conversion from radiocarbon years to calendar years can be achieved.

In this study, the ^{14}C activity of the samples was measured by an accelerator mass spectrometer (AMS) at the AMS Laboratory ETH Zürich. By accelerating the particles to extreme speeds, the small ^{14}C signal can be distinguished from other isotopes and the ratio of ^{14}C relative to ^{13}C or ^{12}C determined (Walker, 2005). In total, seven AMS ^{14}C dates were obtained from the calcareous shells of *N. pachyderma* (s). The ^{14}C dates were corrected for a reservoir age of 400 years with a delta R value of 129 ± 74 , considering the regional reservoir age (Appendix B). The ^{14}C dates were calibrated to calendar years using Bacon v2.2 software (Blaauw and Christen, 2011) and the Marine13 calibration dataset (Reimer et al., 2013) (Table 5.1).

Table 5.1: Samples dated with the ^{14}C AMS method in core GS15-196-02GC, (0 BP = 1950 AD).

Laboratory ID	Core depth (cm)	^{14}C AMS age (BP) $\pm 1\sigma$	Calibrated age (BP)	Age range (min-max)	Delta R
ETH-73712	0-1	6110 \pm 27	6449	6205-6760	129 \pm 74
ETH-73713	4-5	6969 \pm 28	7344	7076-7553	129 \pm 74
ETH-73714	28-29	12217 \pm 36	13535	13248-13829	129 \pm 74
ETH-73715	60-61	14957 \pm 43	17596	17166-17976	129 \pm 74
ETH-73716	100-101	19788 \pm 63	23101	22450-23541	129 \pm 74
ETH-73717	204-205	24293 \pm 92	27967	27615-28468	129 \pm 74
ETH-73718	332-333	30768 \pm 181	34648	33869-36959	129 \pm 74

5.2 Age model

The age model was constructed using the Bacon v.2.2 software (Blaauw and Christen, 2011) (Figure 5.1). Bacon age-depth modelling uses Bayesian statistics to reconstruct the accumulation history of deposits based on single data points. In the past, linear interpolation has been a common method for producing age-depth models, which assumes linear accumulation between each dated interval, resulting in accumulation rates abruptly changing at each dated depth interval. The Bacon software divides the core into several thin sections, and through millions of repetitions it estimates the accumulation rate for every section. Joined with an estimated starting date of the interval, the accumulation rates make the basis for the age-depth model (Blaauw and Christen, 2013).

Sedimentation rates (Table 5.2) for each dated depth interval were calculated based on the age model. On average, the sedimentation rate is 10.67 cm/kyr.

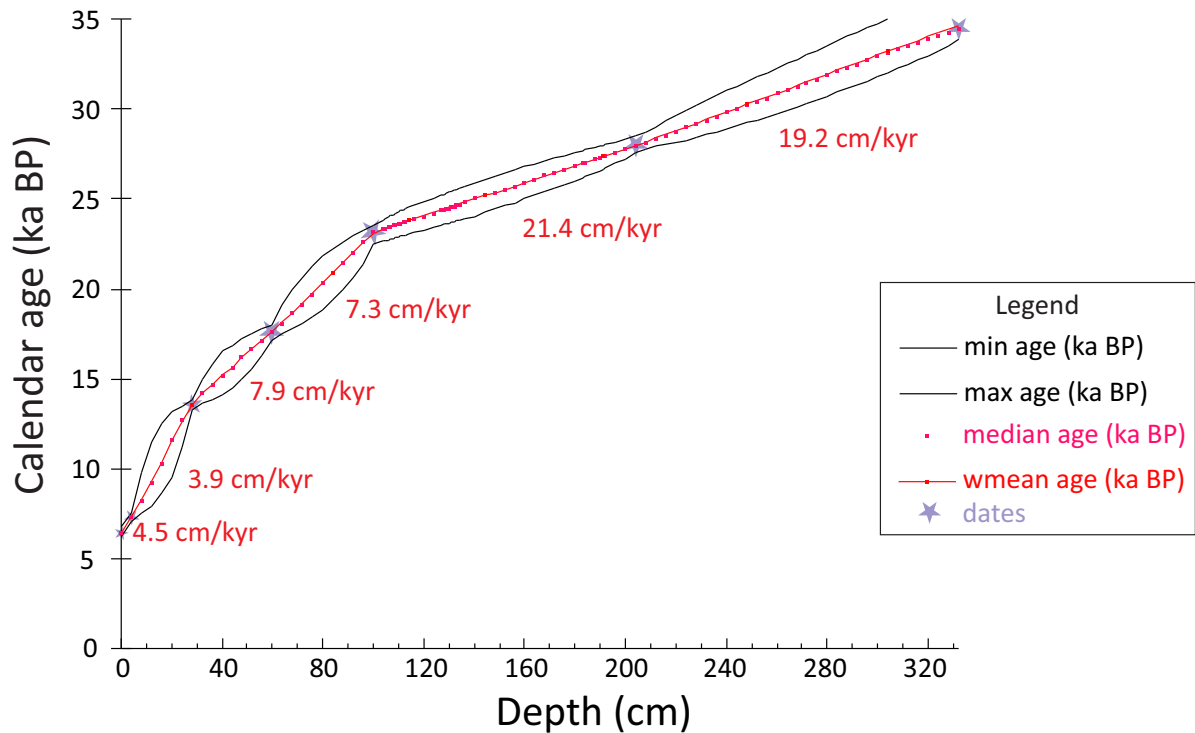


Figure 5.1: Age depth plot for core GS15-196-02GC constructed with Bacon v.2.2 software (Blaauw and Christen, 2011). Red text notes the accumulation rates for each dated depth interval. The results presented in the next chapters are plotted against the wmean age.

Table 5.2: Sedimentation rates for GS15-196-02GC.

Depth Interval	Age range (yr. BP)	Sedimentation rate
0-4 cm	6448 - 7343	4.5 cm/kyr
4-28 cm	7343 - 13534	3.9 cm/kyr
28-60 cm	13534 - 17595	7.9 cm/kyr
60-100 cm	17595 - 23101	7.3 cm/kyr
100-204 cm	23101 - 27785	21.4 cm/kyr
204-332 cm	27785 - 34647	19.2 cm/kyr

5.2.1 Reservoir ages in the North Atlantic

Current age model calibrations assume that the reservoir age of surface waters in the North Atlantic (ca. 400 years) have been constant over time. However, studies have found that reservoir ages in the high-latitudes North Atlantic during the last deglaciation (especially during H1) may be substantially older, up to 2000 years (Waelbroeck et al., 2001; Thornalley et al.,

2011), although some of the dates have been questioned (Broecker et al., 2009). If such high reservoir ages influenced the core site, then the age model constructed from GS15-196-02GC might be biased toward old dates. However, the upcoming results are mainly based on samples taken from the same core and age model uncertainties will not affect the coupling and relative timing of the different climate proxies recorded within the same sediment sequence.

6. RESULTS

The gravity core GS15-196-02GC (0-334.5 cm) covers the last glaciation (MIS 2), as well as the deglaciation and early Holocene, allowing for a detailed study of Eirik drift sediments and key variations in DSOW, a constituent of NADW, during both glacial and deglacial periods.

Planktonic and benthonic foraminifera species picked at 4 cm space interval underwent stable isotope analysis. The 4 cm space interval gives relatively high time resolution (on average ~340 years/4 cm), especially during the last glaciation (~200 years/4 cm). The bottom water record is of slightly lower resolution in a few intervals due to scarcity of *C. wuellerstorfi*.

In the following subchapters, the core description and the results from sedimentological analysis, IRD counts and stable isotope analysis will be presented.

6.1 Core description, magnetic susceptibility and XRF-results

Detailed core description is given in Figure 6.1. The complete core (0-334.5 cm) exhibit little sedimentary disturbances, except for bioturbation around 110 cm. The sediment throughout the core is mostly silt and clay, apart from the upper 16.5 cm, which consists of sand. The upper 125 cm show a dark brown to light brown colour change, whereas from 125 cm and downcore there is a colour change to a darker grey green, with lighter grey mottling. To determine the colours, Munsell colour chart (Munsell, 1976) was used. The entire core is rich in ice rafted debris. At 120 cm, a black (approximately 1 cm thick) layer is found, presumably ash. This is also apparent in the magnetic susceptibility data displaying an increase in this layer. In addition, an increase in the tephra shard abundance was found in the 63-150 μm fraction (pers. comm. N. Irvall). In general, the magnetic susceptibility oscillates with amplitudes ranging between 100×10^{-5} and 600×10^{-5} , apart from extremely high values ($\sim 1000 \times 10^{-5}$) at the ash layer around 120 cm and in the sandy top layer ($\sim 3000 \times 10^{-5}$). The Ca/Sr record oscillates with amplitudes ranging from 2-10 in Ca/Sr ratio. Low Ca/Sr is found in the sandy top layer (around 15–17 cm), around 120 cm and 280-290 cm depth. The highest Ca/Sr ratio occurs at 55 cm core depth, but no clear Ca/Sr peaks are found throughout the record. The Si/Sr record oscillates with amplitudes ranging from 0-0.5 in Si/Sr ratio. High Si/Sr ratios occurs around 123-131 cm and 255–270 cm. Low Si/Sr ratios occurs around 200 cm and 285-290 cm. In the interval 123–131 cm Ca/Sr decrease corresponds to Si/Sr increase.

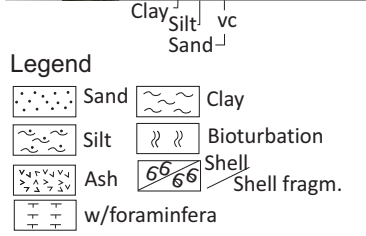
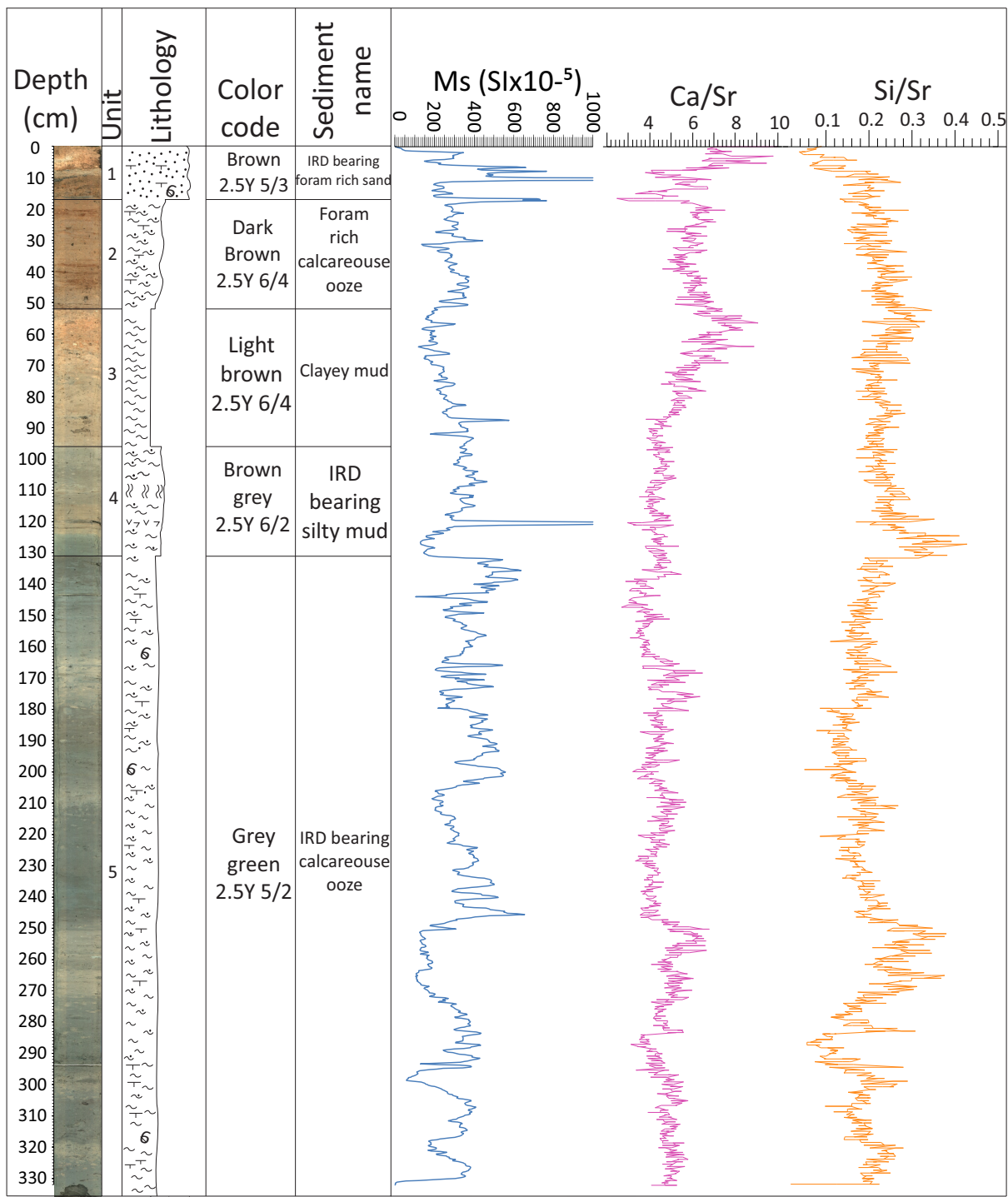


Figure 6.1: Detailed description of core GS15-196-02GC plotted against depth (cm), the sediment names are based on smear slides. The curves represent the sedimentological properties measured; magnetic susceptibility (blue), Ca/Sr (pink) and Si/Sr (orange).

6.2 Ice Rafted Debris (IRD)

In general, findings of increased percentage of ice rafted debris (IRD) in sediment cores are believed to be related to increased input of icebergs at the core site. The IRD found at the site, southeast of Greenland, are most likely derived from the Greenland, Icelandic, Faroe Island or (parts of the) Eurasian ice sheets (most likely Fennoscandian Ice Sheet (FIS) and British Ice Sheet (BIS)). Additionally, larger events (e.g. Heinrich events) may be related to icebergs from the Laurentide Ice sheet.

Seven duplicate counts were carried out approximately every 50 cm (at 0 cm, 52 cm, 100 cm, 152 cm, 200 cm, 252 cm and 300 cm) and a pooled standard deviation of $\pm 2.52\%$ was calculated (Figure 6.2). In addition, a standard error of the mean (SEM) of $\pm 1.78\%$ for sample depth intervals with two replicates was calculated. The results are expressed as the percentages of IRD grains relative to total entities (i.e. foraminifera) in each sample (IRD %). I chose to not express the IRD data in the grains/gram notation. This is due to the wide time interval spanned

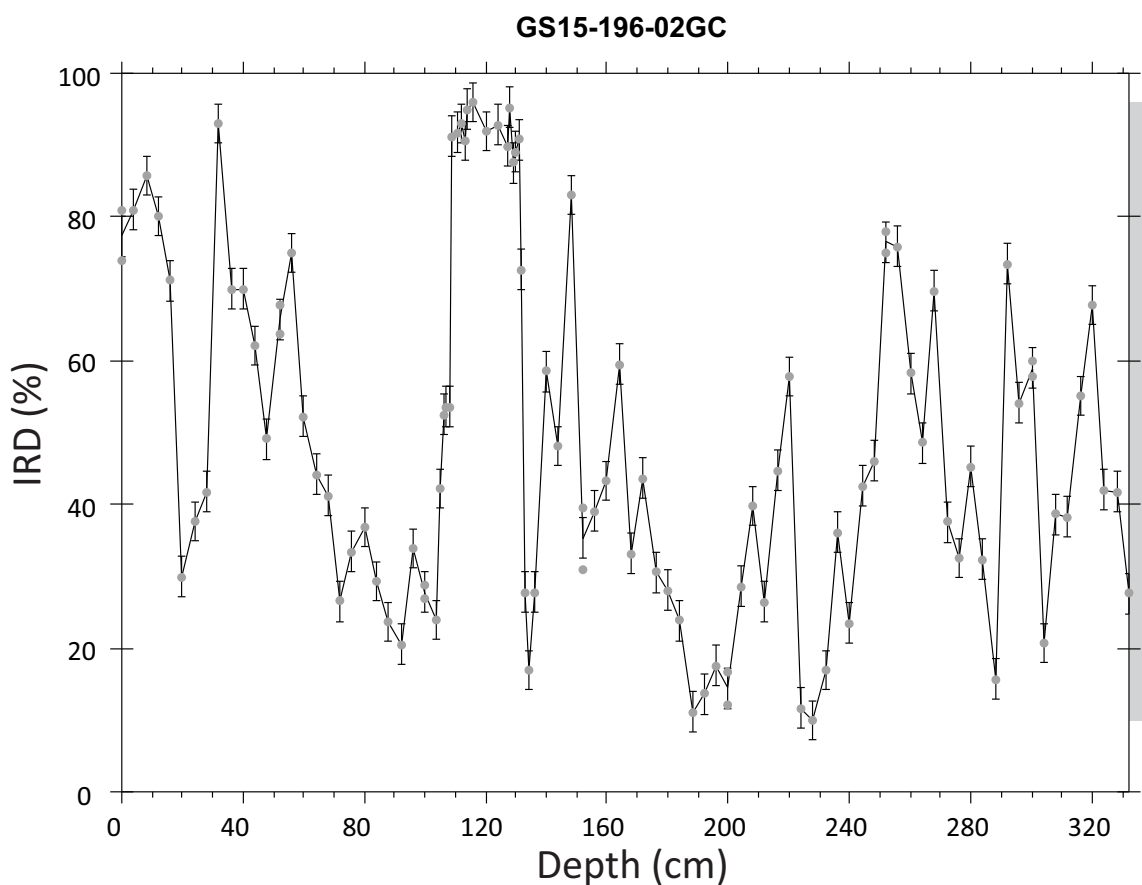


Figure 6.2: IRD (%) record plotted against depth (cm). Error bars denote the pooled standard deviation for all replicates (± 2.52). Grey bar notes the full range of variability.

by the core and the glacial-interglacial transition which can cause a significant change in the sedimentation rates at the core site, where increases in the delivery of fines to the study site might dilute the IRD signal. Figure 6.2 show the percentage of IRD plotted against depth (cm) downcore. However, in order to place the IRD record in a scientific context and make comparisons with well-known glacial/deglacial climate events in the North Atlantic (e.g. Heinrich events and D-O cycles), the IRD record will further be plotted against the GS15-196-02GC age model (Chapter 5).

The IRD % varies between 10% and 95%. 35 IRD peaks have percentages above the average of 55.5%. The highest percentage of IRD (95.9%) occurs at 116 cm at ~23.8 ka. In addition, four intervals of high (75%-95%) IRD % occur at 8 cm, 32 cm-56 cm, 109 cm-132 cm and 252 cm, at ~8.3 ka, 14.2 ka-17.1 ka, 23.5 ka-24.6 ka and 30.4 ka–30.6ka, respectively. The record is greatly oscillating from 132 cm and downcore (24.6 ka-34.6 ka) (Figure 6.3).

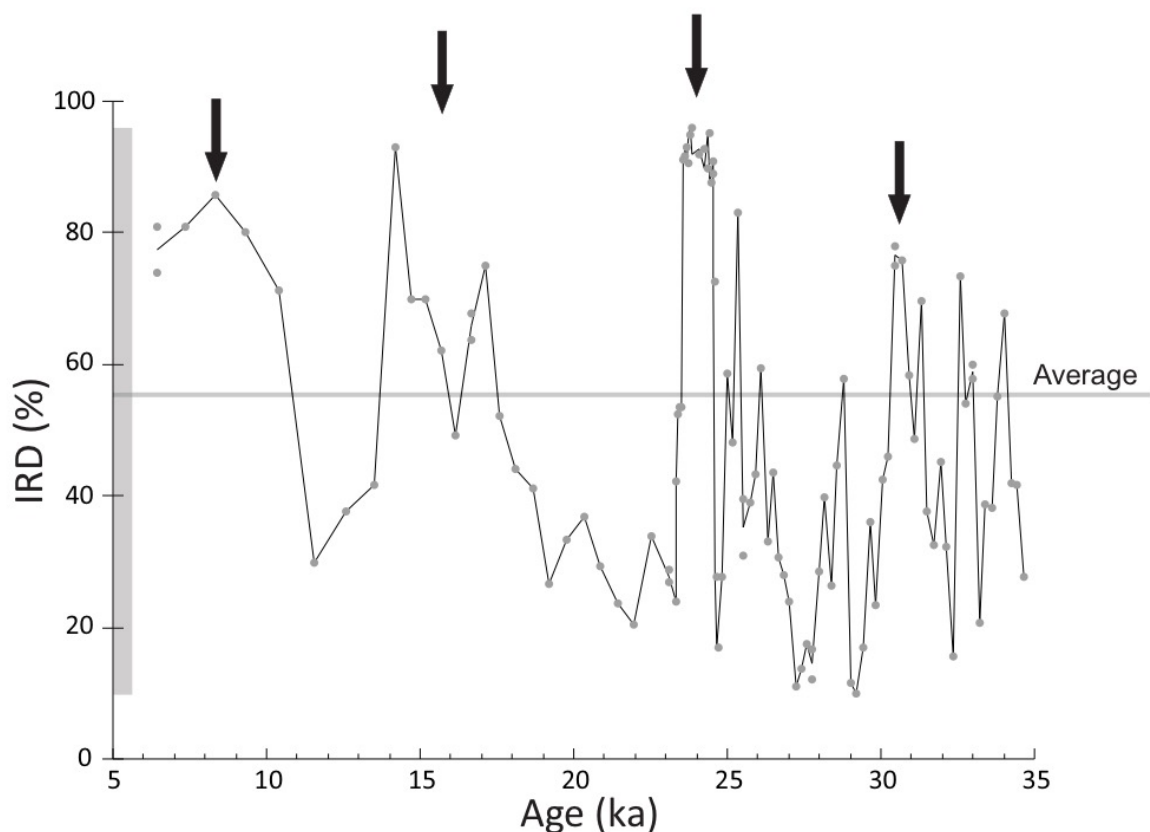


Figure 6.3: The IRD (%) record from core GS15-196-02GC plotted against age (ka BP). All measurements are shown (grey markers) with the solid black line tracing the average IRD values at every 4 cm core depth interval (apart from interval 109-134 cm where every 1cm was counted). The arrows denote the events of high IRD (%), described in greater detail in the text. The grey bar illustrates the full range of variability and the horizontal grey line represents the average.

A broad IRD peak (75%-93%) occurs during the period from 17.1 ka to 14.2 ka, partly associated with H1 (hereinafter event 1) previously dated to 17.5 ka - 16.5 ka (Hemming, 2004; Wang et al., 2006). Further, the highest percentage of IRD (90%-95%) occurs at ~24.6 ka-23.5 ka, and this event (hereinafter event 2) is associated with H2, previously dated to 26 ka – 24 ka (Hemming, 2004; Wang et al., 2006). Event 2 occurs abruptly (with IRD % decreasing from 90% to 27%) over a period of only 100 years (131–133 cm). In a similar manner, the event ends abruptly and a change from 53% to 91% occurs over a span of only 50 years (108 cm-109 cm). Lastly, an increase to 76% is found around 30.6 ka-30.4 ka and is associated with H3 (hereinafter event 3), previously dated to ~31 ka (Meese et al., 1997).

6.3 Oxygen isotope results

The most important factors influencing foraminifera $\delta^{18}\text{O}$ are the global sea level and continental ice volume. During glacial times, continental ice sheets store freshwater with negative $\delta^{18}\text{O}$ values, leaving the isotopic composition of the remaining sea water with more positive $\delta^{18}\text{O}$ values and reducing the global sea level, often referred to as “the glacial effect”. During the last glacial maximum between 23 ka and 19 ka (Mix et al., 2001), the global sea level has been estimated to be ~125 m lower than today (Lambeck et al., 2014), and we can assume that the seawater contained highly different oceanic $\delta^{18}\text{O}$ values.

Using Equation 4.4 presented in Chapter 4, relative changes in the $\delta^{18}\text{O}$ record can be calculated to corresponding relative changes in temperature. Based on the paleotemperature equation (Epstein et al., 1953), a 1‰ decrease in $\delta^{18}\text{O}$ corresponds to a 4.3°C surface temperature increase. Further, based on measurements of the $\delta^{18}\text{O}$ and salinity relationship in the region, a 1‰ decrease in $\delta^{18}\text{O}$ corresponds to a decrease in salinity of 1.81 psu (0.55‰ psu^{-1}) (Schmidt, 1999; Schmidt et al., 1999; Bigg and Rohling, 2000; pers. comm. U. Ninnemann). Although, the seawater and salinity $\delta^{18}\text{O}$ relationship is not constant over time. In the next subchapters, the calculated salinity changes are based on the modern seawater and salinity $\delta^{18}\text{O}$ relationship, which is dominated by evaporation and precipitation in the North Atlantic. However, during the last glacial and deglacial (e.g. H-events) the seawater and salinity $\delta^{18}\text{O}$ relationship were mainly dominated by freshwater from continental ice sheets that contain more depleted $\delta^{18}\text{O}$, and may drive a large $\delta^{18}\text{O}$ anomaly with a small salinity change. Hence, the calculated salinity change can be overestimated and must be considered as a maximum.

6.3.1 Near-surface water (planktonics)

The *N. pachyderma* (s) $\delta^{18}\text{O}$ record represent salinity and temperature variations in the near-surface waters in the Irminger Sea during the last glacial and deglacial period. Figure 6.4 shows the $\delta^{18}\text{O}$ (‰) record of *N. pachyderma* (s) plotted versus depth (cm). Duplicate measurements of *N. pachyderma* (s) were carried out approximately every third sample depth interval. A standard deviation (SD) for all replicates of $\pm 0.076\text{‰}$ was calculated, represented by pink error bars in Figure 6.4. The calculated standard deviation is slightly lower than the precision of the mass spectrometer ($\pm 0.08\text{‰}$), indicating reproducible and reliable results. In addition, a standard error of the mean (SEM) of $\pm 0.05\text{‰}$ for sample depth intervals with two replicates was calculated (see Appendix A).

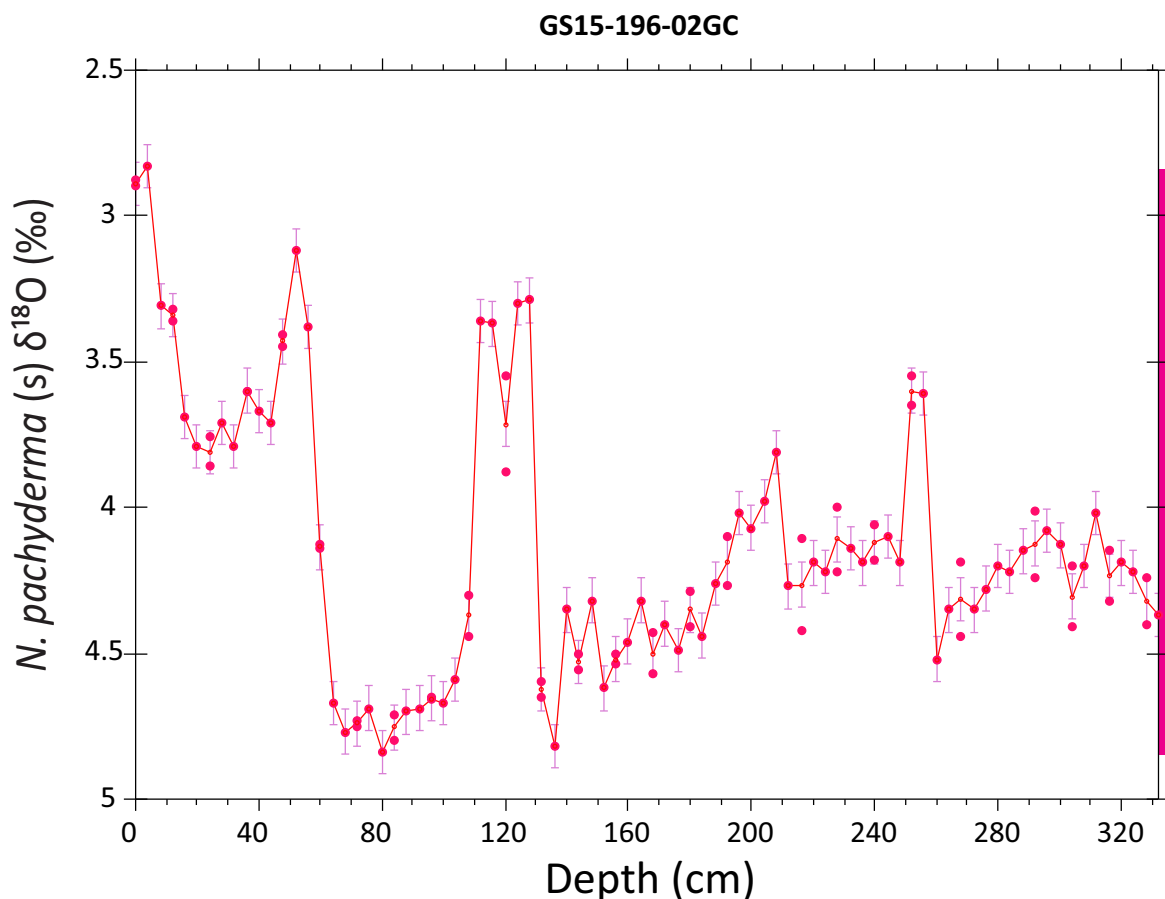


Figure 6.4: The planktonic $\delta^{18}\text{O}$ record (*N. pachyderma* (s)) from core GS15-196-02GC relative to VPDB plotted against depth (cm). The solid red line traces the average $\delta^{18}\text{O}$ values at every 4 cm core depth interval. The error bars represent the standard deviation for all replicates of $\pm 0.076\text{‰}$. The pink bar illustrates the full range of variability. Note that the $\delta^{18}\text{O}$ record is plotted on a reversed scale.

The *N. pachyderma* (s) oxygen isotope record show values ranging from 2.83‰ to 4.84‰, a total range in variability of 2.01‰. The record is characterized by large and abrupt events of decreasing or increasing values occurring over as little as 4 cm (one sample depth interval).

Some of these abrupt changes in $\delta^{18}\text{O}$ are large, with amplitudes ranging between 0.7‰ and 1.33‰, well above the uncertainties in the analyses. Further, since the oscillations found are so large in amplitude it is likely that the oscillations largely reflect changes in the surface water properties (temperature and salinity) and not uncertainties related to ontogenic effects and possible changes in depth habitat (explained in subchapter 4.5). In addition, with a 4-cm sample interval it is unlikely that bioturbation has disturbed the signal, since most of these events span over several samples that are significantly separated in depth. To place the oxygen isotope results in a scientific context and make comparisons with previously published $\delta^{18}\text{O}$ records a chronological view of the results must be established. Hence, further the results will be shown plotted against the age model presented in Chapter 5.

Four events with minimum $\delta^{18}\text{O}$ (‰) values occur at 0 cm-4 cm, 52 cm-56 cm, 112 cm-128 cm and 252 cm-256 cm, which corresponds to ~6 ka-7 ka (minimum value of ~2.8‰), 16.6 ka-17.1 ka (minimum value of ~3.12‰), 23.7 ka-24.4 ka (minimum value of ~3.3‰) and 30.4 ka-30.6 ka (minimum value of ~3.6‰), respectively (Figure 6.5). Further, $\delta^{18}\text{O}$ remains very high (value of ~4.8‰) from 60 cm to 108 cm, approximately at 23.5 ka-17.5 ka, during the LGM.

All events of low $\delta^{18}\text{O}$ are intervals with high percentages of IRD, however other IRD peaks occur without accompanying $\delta^{18}\text{O}$ reductions. The core top event (0-4 cm near ~6 ka-7 ka) reflect the Holocene at the core site and has values typical of the early Holocene in the area (e.g. (Kleiven et al., 2008)). The $\delta^{18}\text{O}$ low around 17.1 ka-16.6 ka (Event 1) falls close in time to Heinrich event 1. Prior to this event, during the deglacial/glacial transition (23.5 ka-17.5 ka), $\delta^{18}\text{O}$ values are stable around ~4.6‰ and over a period of only 1000 years (from 17.5 ka to 16.5 ka, during H1) the $\delta^{18}\text{O}$ values drop by ~1.55‰. This indicates a potential sea surface temperature (SST) increase of ~6.3°C or salinity decrease of 2.6 psu in the near-surface waters southeast of Greenland. The $\delta^{18}\text{O}$ values remain high during the last glacial maximum (LGM). However, prior to the LGM, the $\delta^{18}\text{O}$ values abruptly jump to low $\delta^{18}\text{O}$ values of ~3.3‰ lasting for ~700 years (24.4 ka-23.7 ka) (Event 2). This abrupt climatic jump indicates a potential SST increase in the near-surface waters southeast of Greenland of ~5.7 °C, or a salinity decrease of 2.4 psu, occurring over a period of maximum 200 years. In time this low $\delta^{18}\text{O}$ event falls close to Heinrich event 2. Further, prior to the low $\delta^{18}\text{O}$ anomaly during event 2, the record oscillates in the range of 4.6‰ to 3.6‰ (34.6 ka-24.6 ka). A third abrupt decrease in $\delta^{18}\text{O}$ is found around 30.6 ka-30.4 ka (Event 3), falling close in time to Heinrich event 3 and coincides with high IRD

% . Event 3 is both shorter in duration and smaller in magnitude compared to the other events, but the $\Delta\delta^{18}\text{O}$ represents a potential SST increase of $\sim 3.9^\circ\text{C}$ or a salinity decrease of 1.66 psu.

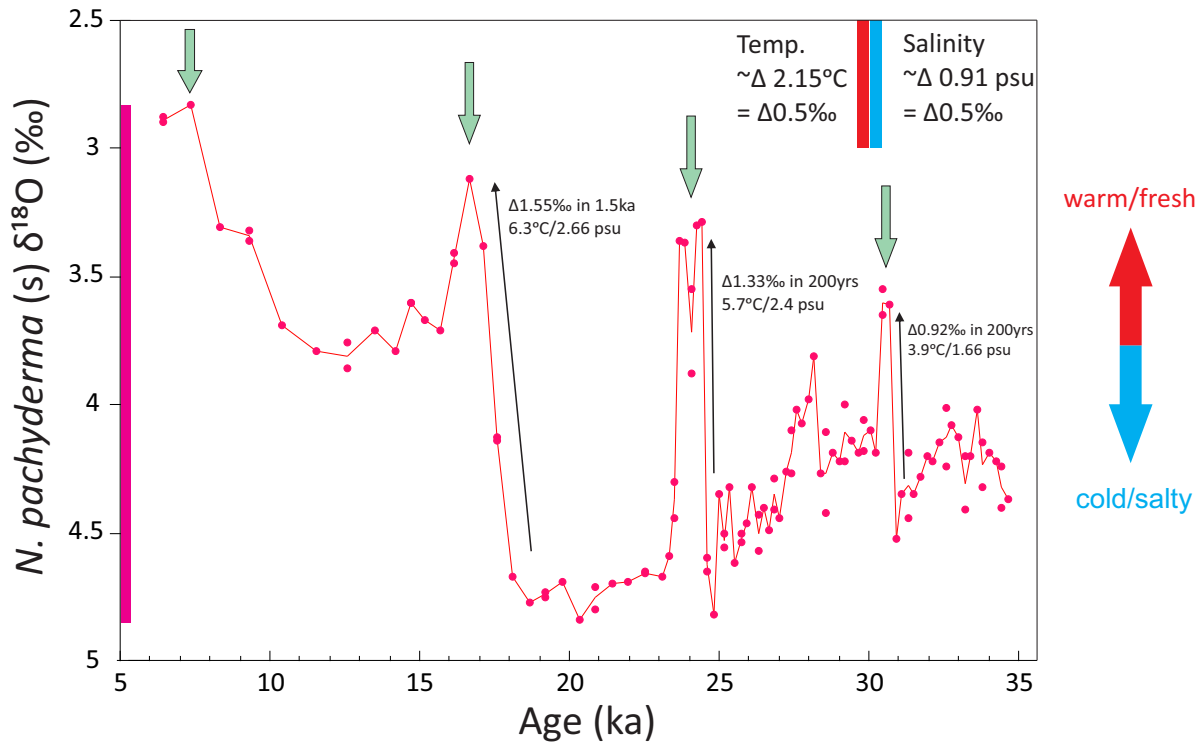


Figure 6.5: The planktonic $\delta^{18}\text{O}$ record (*N. pachyderma* (s)) from core GS15-196-02GC relative to VPDB plotted against age (ka BP). All measurements are shown (pink markers) with the solid red line tracing the average $\delta^{18}\text{O}$ values at every 4 cm core depth interval. The green arrows denote the events of low $\delta^{18}\text{O}$, described in the text. The black arrows indicate the possible temperature/salinity change occurring during the event. The red/blue arrow illustrates how the record oscillates between warm/fresh and cold/salty conditions. The pink bar illustrates the full range of variability.

6.3.2 Deep water (benthonic)

Benthonic foraminifera such as *C. wuellerstorfi* live in a deep-sea environment with very low and stable temperatures (Rohling and Cooke, 1999). Hence, the *C. wuellerstorfi* oxygen isotope record mainly reflects changes in the deep water properties (such as past temperatures) at the core site (2468 m water depth), which is directly overlain by the DSOW.

Figure 6.6 shows the $\delta^{18}\text{O}$ (‰) record of *C. wuellerstorfi* plotted versus depth (cm). Duplicate measurements of *C. wuellerstorfi* were carried out when possible and a pooled standard deviation from the mean of $\pm 0.08\text{‰}$ was calculated, represented by light blue error bars in Figure 6.6. The SD is the same as the precision of the mass spectrometer ($\pm 0.08\text{‰}$), indicating

that the samples reproduce well and give reliable results. In addition, a standard error of the mean (SEM) of $\pm 0.06\%$ for intervals with two replicates was calculated.

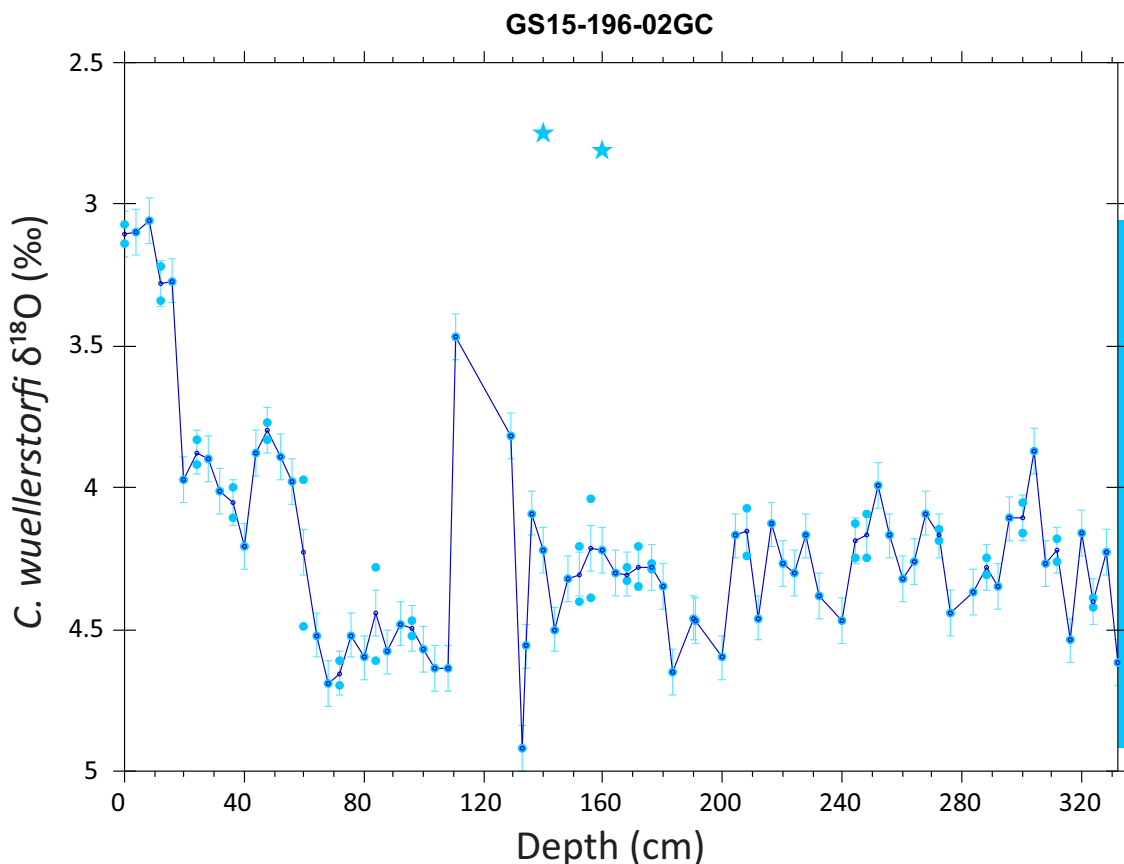


Figure 6.6: The benthonic $\delta^{18}\text{O}$ record (*C. wuellerstorfi*) from core GS15-196-02GC relative to VPDB plotted against depth (cm). The solid blue line tracing the average $\delta^{18}\text{O}$ values at every 4 cm core depth interval (when possible). Note that the interval from 111 cm to 129 cm only contains two data points. The error bars represent the standard deviation of $\pm 0.08\%$. The blue bar demonstrates the variability. Further, the two blue stars represents $\delta^{18}\text{O}$ measurements, which are believed to be incorrect due to incomplete reaction and/or insufficient removal of contaminants, and were not included in the calculations of the SD and average $\delta^{18}\text{O}$ values.

The *C. wuellerstorfi* oxygen isotope record has range of 3.06% - 4.92% , a difference of 1.86% . The record is characterized by a few large and abrupt events as well as small oscillations with amplitudes of $\sim 0.5\%$, this is seen especially during the second half of the record, from 132 cm and downcore. The large and abrupt events of decreasing and increasing values occur over 4 cm intervals, and have amplitudes ranging between 0.6% and 1.1% , well above the calculated average standard deviation.

Figure 6.7 shows the *C. wuellerstorfi* oxygen isotope record plotted against age. Three events of decreased $\delta^{18}\text{O}$ occur at 0 cm-16 cm (to values of 3.0% - 3.3%), 44 cm-56 cm (to a minimum

value of 3.8‰) and 111 cm-129 cm (to values of 3.4‰-3.8‰), approximately at ~6 ka-10 ka, 15.6 ka-17.1 ka and 23.6 ka-24.4 ka, respectively. The $\delta^{18}\text{O}$ record varies with $\sim 1.63\text{‰}$ between the Holocene and the LGM, reflecting large changes in the physical properties of the deep water masses in the area over glacial-interglacial time scales.

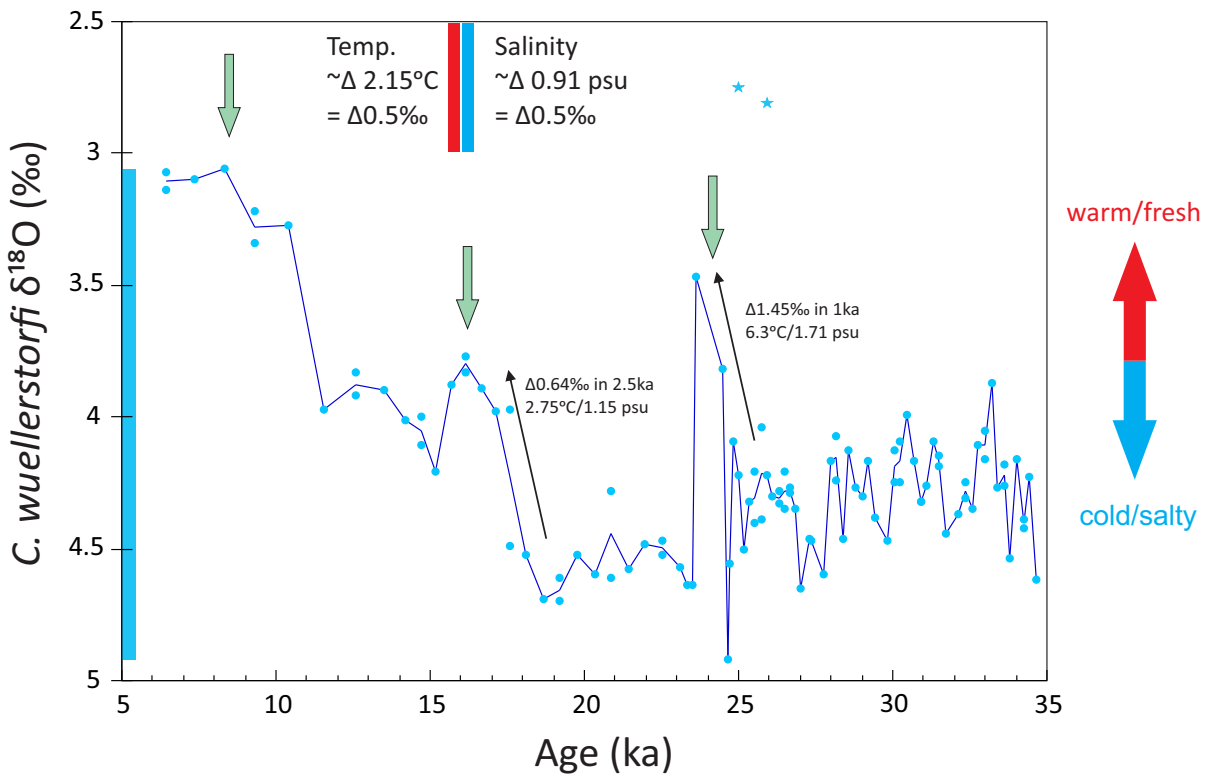


Figure 6.7: The benthonic $\delta^{18}\text{O}$ record (*C. wuellerstorfi*) from core GS15-196-02GC relative to VPDB plotted against age (ka BP). All measurements are shown (light blue) with the solid blue line tracing the average $\delta^{18}\text{O}$ values at every 4cm core depth interval (when possible). The green arrows denote the events described in the text. The black arrows indicate the potential temperature/salinity change occurring during the event. Note that the interval from 23.6 ka-24.4 ka (111 cm-129 cm) only contains two data points. The two blue stars represents $\delta^{18}\text{O}$ measurements believed to be incorrect due to incomplete reaction and/or insufficient removal of contaminants, and were not included in the calculations of the average $\delta^{18}\text{O}$ values.

The most clear and abrupt event occurs during the last glaciation around 24.4 ka-23.6 ka (Event 2), associated in time with Heinrich event 2. Event 2 shows a sharp transition into lower $\delta^{18}\text{O}$ values (from 4.9‰ to 3.8‰) occurring over a period of ~ 250 years. This period of low $\delta^{18}\text{O}$ lasts for ~ 800 years, before another sharp transition back to high $\delta^{18}\text{O}$ values (from 3.4‰ to 4.6‰) occurs. The entire event lasts for approximately 1000 years and shows a total $\delta^{18}\text{O}$ change of 1.45‰ (from 4.93‰-3.47‰). Event 2 could represent a $\sim 6.3^\circ\text{C}$ warming or ~ 1.71 psu salinity decrease of the bottom waters. Prior to this event, from ~ 34 ka-25 ka, the record oscillates in the range from 4.6‰ to 3.8‰. In addition, the low $\delta^{18}\text{O}$ event at 15.6 ka-17.1 ka

(Event 1) is in time associated with Heinrich event 1 and represents a potential temperature increase of $\sim 2.75^{\circ}\text{C}$ or salinity decrease of ~ 1.15 psu.

6.3.3 Planktonic $\delta^{18}\text{O}$ vs. Benthonic $\delta^{18}\text{O}$

The benthonic oxygen isotope record compared to the planktonic oxygen isotope record highlights the similarities in the records (Figure 6.8). Generally, the records are in phase with each other and low planktonic $\delta^{18}\text{O}$ corresponds to low benthonic $\delta^{18}\text{O}$. All three low $\delta^{18}\text{O}$ events found in the benthonic record (early-mid Holocene, event 1 and event 2) are also found in the planktonic $\delta^{18}\text{O}$ record. However, the last planktonic $\delta^{18}\text{O}$ reduction (event 3) is not seen in the benthonic record, at least not with the same magnitude. Event 1 (~ 16.5 ka ago) which is found in both benthonic and planktonic records, differs in amplitude. The planktonic record shows a larger reduction in $\delta^{18}\text{O}$ than the benthonic record. This larger reduction of $\sim 0.7\text{‰}$ observed in the planktonic $\delta^{18}\text{O}$ record suggests that the near-surface water at the core site warmed an additional 3°C or experienced an extra freshening of ~ 1.23 psu relative to the deep water during this event. The latter seems more likely given the coeval increase in IRD %. The other large and abrupt decrease in $\delta^{18}\text{O}$, event 2, is represented in both records, with similar $\delta^{18}\text{O}$ values.

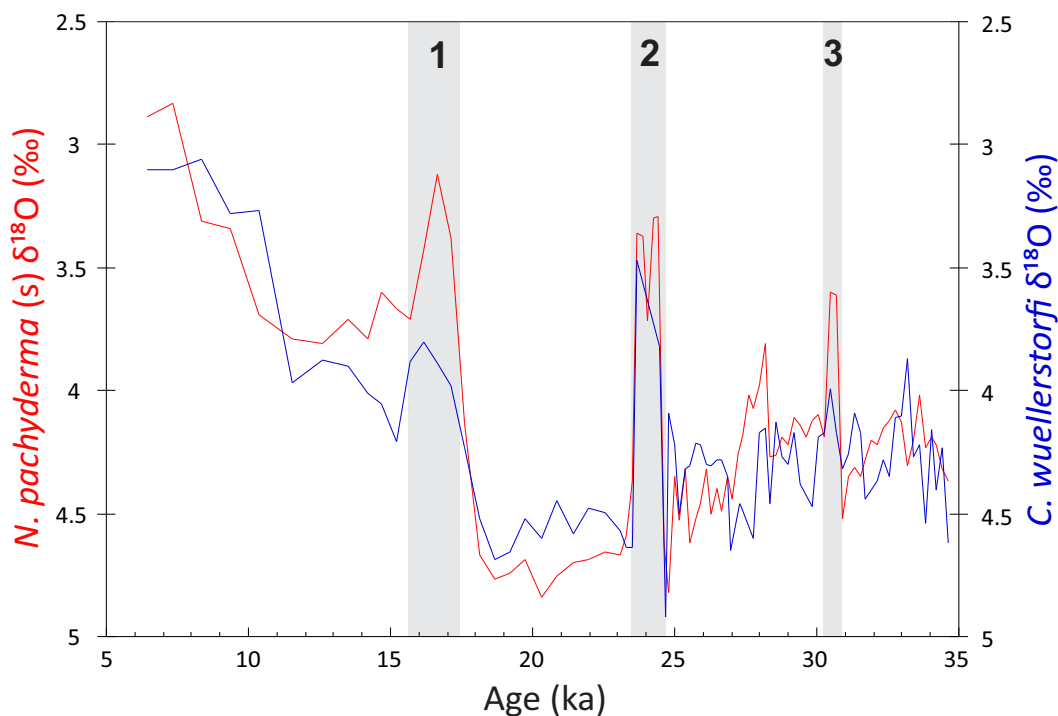


Figure 6.8: GS15-196-02GC planktonic (*N. pachyderma* (s)) (red curve) and benthonic (*C. wuellerstorfi*) (blue curve) averaged $\delta^{18}\text{O}$ record relative to VPDB plotted against age (ka BP). Shaded grey areas represents event 1-3 described in the text.

6.4 Carbon isotope results

The main deep water mass bathing the core site today is DSOW, a constituent of NADW. During glacial times and the last glacial maximum, the distribution of $\delta^{13}\text{C}$ in the deep Atlantic was considerably different than today (see subchapter 2.3.1). The modern $\delta^{13}\text{C}$ distribution in the Atlantic show a much smaller range of $\delta^{13}\text{C}$ values than during the LGM. Today, the highest $\delta^{13}\text{C}$ values are found in the surface waters of the subtropical gyre, and the lowest values in the Southern Ocean ($\sim -0.2\text{‰}$ (Eide et al., 2017)). $\delta^{13}\text{C}$ rich NADW ($\sim -1.2\text{‰}$ (Eide et al., 2017)) and constituents of this water mass are found down to at least 2500 m in the North Atlantic (Oppo and Lehman, 1993).

6.4.1 Near-surface water (planktonic)

Duplicate measurements of *N. pachyderma* (s) $\delta^{13}\text{C}$ were carried out at approximately every third sample depth interval. For $\delta^{13}\text{C}$ a pooled standard deviation for all replicates of $\pm 0.056\text{‰}$ was calculated (Figure 6.9). This is slightly higher than the precision of the mass spectrometer ($\pm 0.03\text{‰}$), but still indicating reproducible and reliable results. In addition, a SEM of $\pm 0.04\text{‰}$ for intervals with two replicates was calculated (Appendix A).

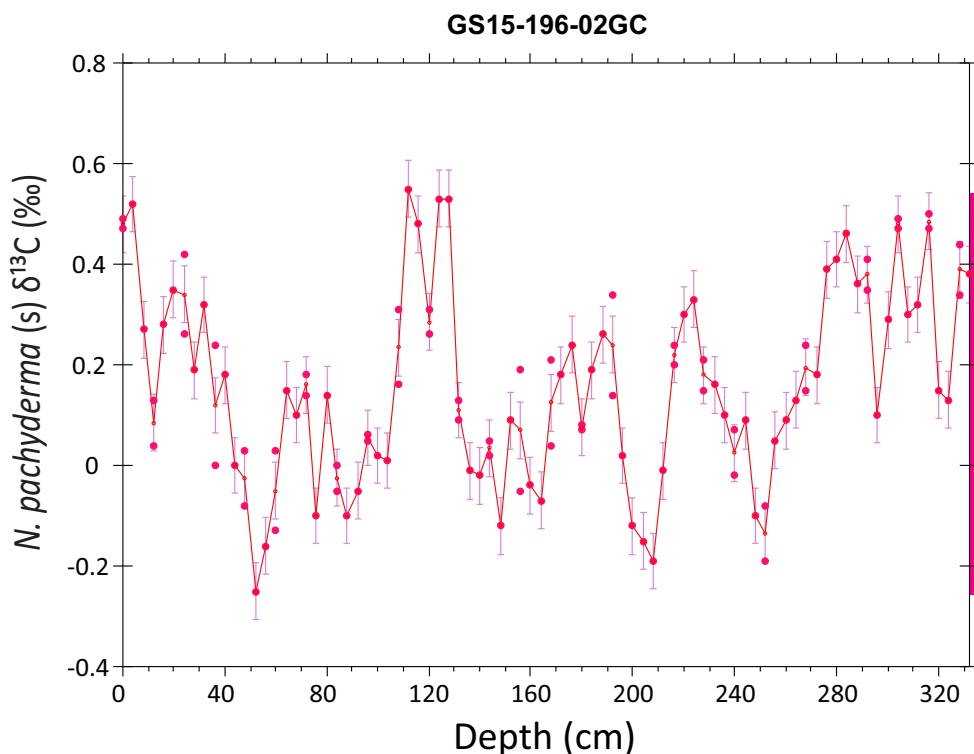


Figure 6.9: The planktonic (*N. pachyderma* (s)) $\delta^{13}\text{C}$ from core GS15-196-02GC relative to VPDB plotted against depth (cm). The solid red line tracing the average $\delta^{13}\text{C}$ values at every 4 cm core depth interval. Dots represents all measurements. Error bars represent a pooled standard deviation of $\pm 0.056\text{‰}$. The pink bar illustrates the full range of variability.

The *N. pachyderma* (s) $\delta^{13}\text{C}$ record shows variability and oscillates in the range from -0.25‰ to 0.55‰ . Generally, *N. pachyderma* (s) $\delta^{13}\text{C}$ and $\delta^{18}\text{O}$ records show a positive covariance where planktonic $\delta^{13}\text{C}$ lows corresponds to planktonic $\delta^{18}\text{O}$ lows, excluding event 2, when planktonic $\delta^{13}\text{C}$ increase occurred at the same time as planktonic $\delta^{18}\text{O}$ decrease. The record (Figures 6.9 and 6.10), documents four main events of low $\delta^{13}\text{C}$ which occur at 12 cm ($\delta^{13}\text{C}$ value of 0.08‰), 48 cm-60 cm ($\delta^{13}\text{C}$ minimum value of -0.25‰), 200 cm-212 cm ($\delta^{13}\text{C}$ minimum value of -0.19‰) and 248 cm-252 cm ($\delta^{13}\text{C}$ minimum value of -0.13‰), approximately at 9 ka, 16.1 ka-17.5 ka (associated with H1), 27.7 ka-28.3 ka and 30.2 ka-30.4 ka (associated with H3), respectively. In addition, a rapid $\delta^{13}\text{C}$ increase to 0.55‰ occurs at ~ 23.5 ka. This period of high $\delta^{13}\text{C}$ lasts for maximum 1000 years (24.5 ka-23.5 ka) and is associated with H2.

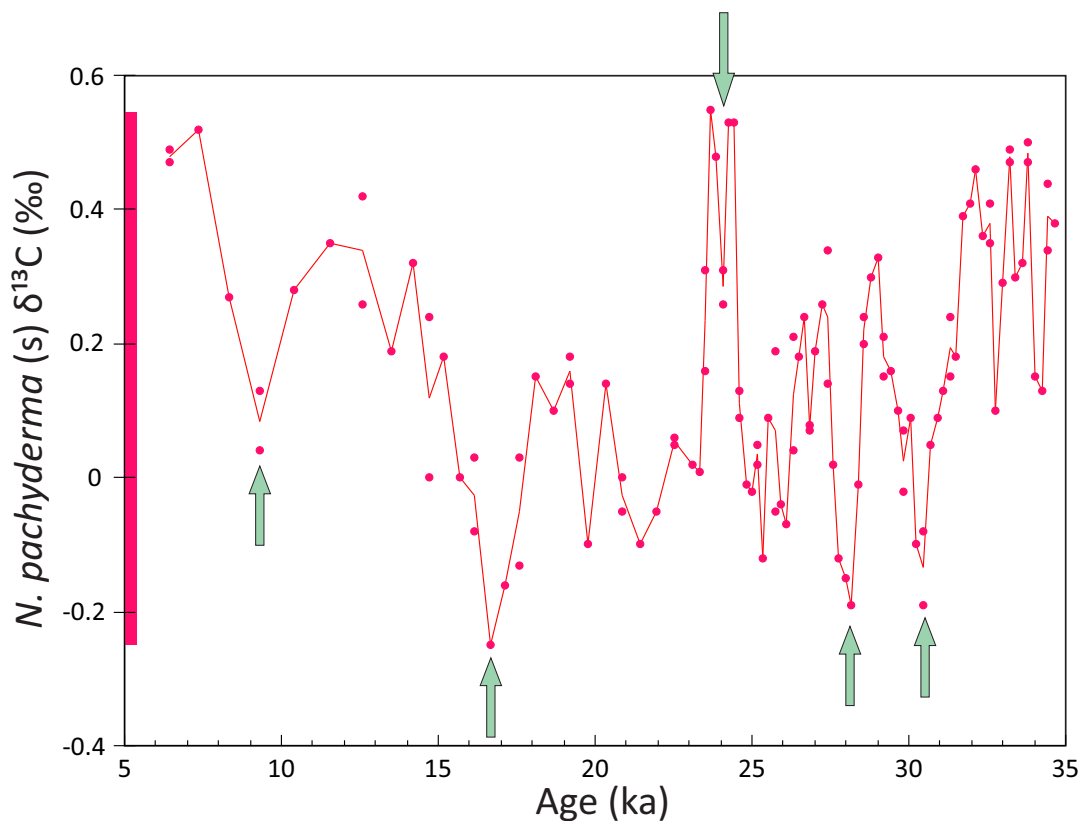


Figure 6.10: The planktonic $\delta^{13}\text{C}$ record (*N. pachyderma* (s)) from core GS15-196-02GC relative to VPDB plotted against age (ka BP). All measurements are shown (pink markers) with the solid red line tracing the average $\delta^{13}\text{C}$ values at every 4 cm core depth interval. The arrows denote the events described in greater detail in the text. The pink bar illustrates the full range of variability.

6.4.2 Deep water (benthonic)

Duplicate measurements of *C. wuellerstorfi* $\delta^{13}\text{C}$ were carried out when possible and a pooled standard deviation from the mean of $\pm 0.12\text{‰}$ was calculated (Figure 6.11). This value is higher than the precision of the mass spectrometer ($\pm 0.03\text{‰}$), however, it still indicates that the samples reproduce well and give reliable results. In addition, a SEM of $\pm 0.08\text{‰}$ for intervals with two replicates was calculated.

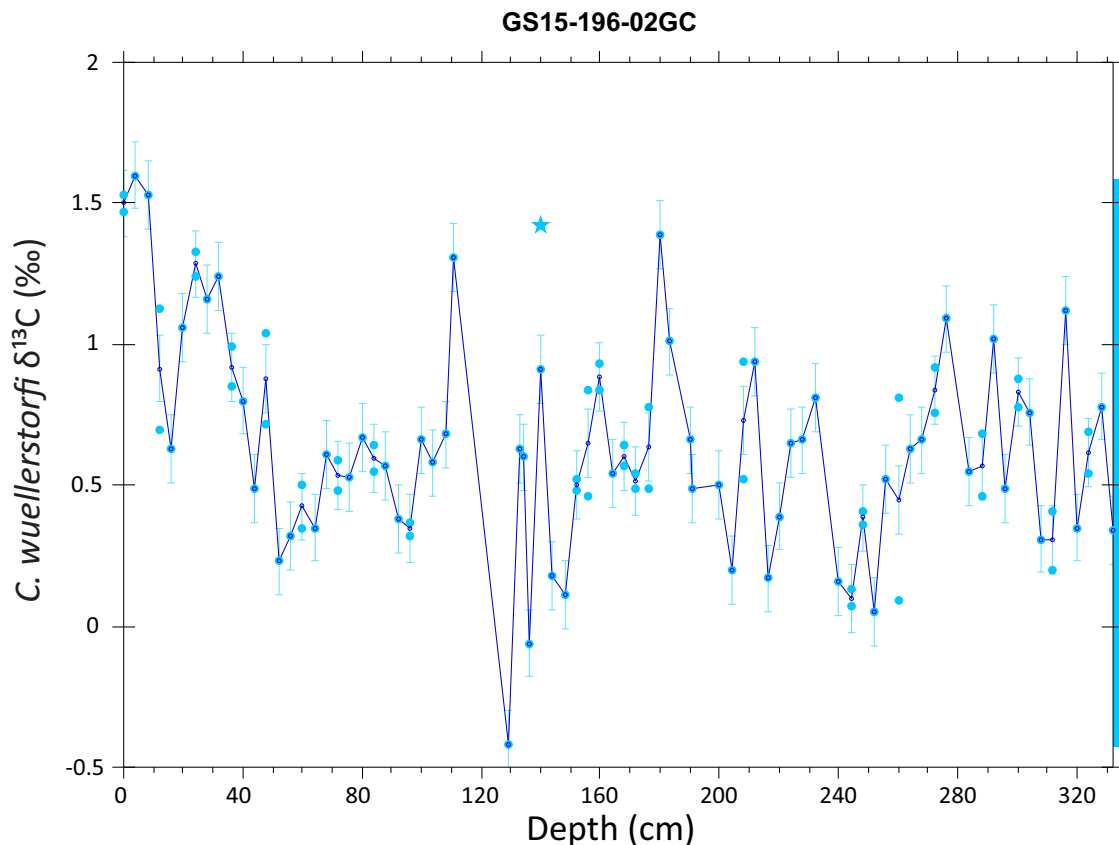


Figure 6.11: The benthonic $\delta^{13}\text{C}$ record (*C. wuellerstorfi*) from core GS15-196-02GC relative to VPDB plotted against age (ka BP). All measurements are shown (light blue) with the solid blue line tracing the average $\delta^{13}\text{C}$ values at every 4cm core depth interval (when possible). Blue bar show the variability. Error bars represents a standard deviation from the mean of $\pm 0.12\text{‰}$. Further, the blue star represents $\delta^{13}\text{C}$ measurements that are believed to be incorrect due to incomplete reaction and/or insufficient removal of contaminants, and was not included in the calculations of the average $\delta^{13}\text{C}$ values or the standard deviation.

The *C. wuellerstorfi* $\delta^{13}\text{C}$ record (Figure 6.12) oscillates between -0.42‰ and 1.6‰ . The record identifies four main events of low $\delta^{13}\text{C}$ occurring at 16 cm ($\delta^{13}\text{C}$ value of 0.63‰), 52 cm-56 cm ($\delta^{13}\text{C}$ minimum value of 0.23‰), 129 cm ($\delta^{13}\text{C}$ value of -0.42‰) and 252 cm ($\delta^{13}\text{C}$ value of 0.05‰), approximately at 10.3 ka, 16.6 ka-17.1 ka (associated with H1), 24.4 ka (associated with H2) and 30.4 ka (associated with H3), respectively. In general, the events of low $\delta^{13}\text{C}$

correlates to decreases in $\delta^{18}\text{O}$ (*C. wuellerstorfi* and *N. pachyderma* (s)) and increased percentage of IRD. In addition, the record identifies three events of high $\delta^{13}\text{C}$ values occurring at 20 cm–32 cm, 111 cm and 180 cm, near 11.5 ka–14.2 ka ($\delta^{13}\text{C}$ minimum value of 1.28‰), 23.6 ka ($\delta^{13}\text{C}$ value of 1.31‰) and 26.8 ka ($\delta^{13}\text{C}$ value of 1.39‰), respectively. High $\delta^{13}\text{C}$ values indicate that deep water ventilation was strong at these times, and especially interesting is the apparent abrupt recovery of deep water ventilation around 23.6 ka, after $\delta^{13}\text{C}$ minimum and weak ventilation just ~800 years earlier.

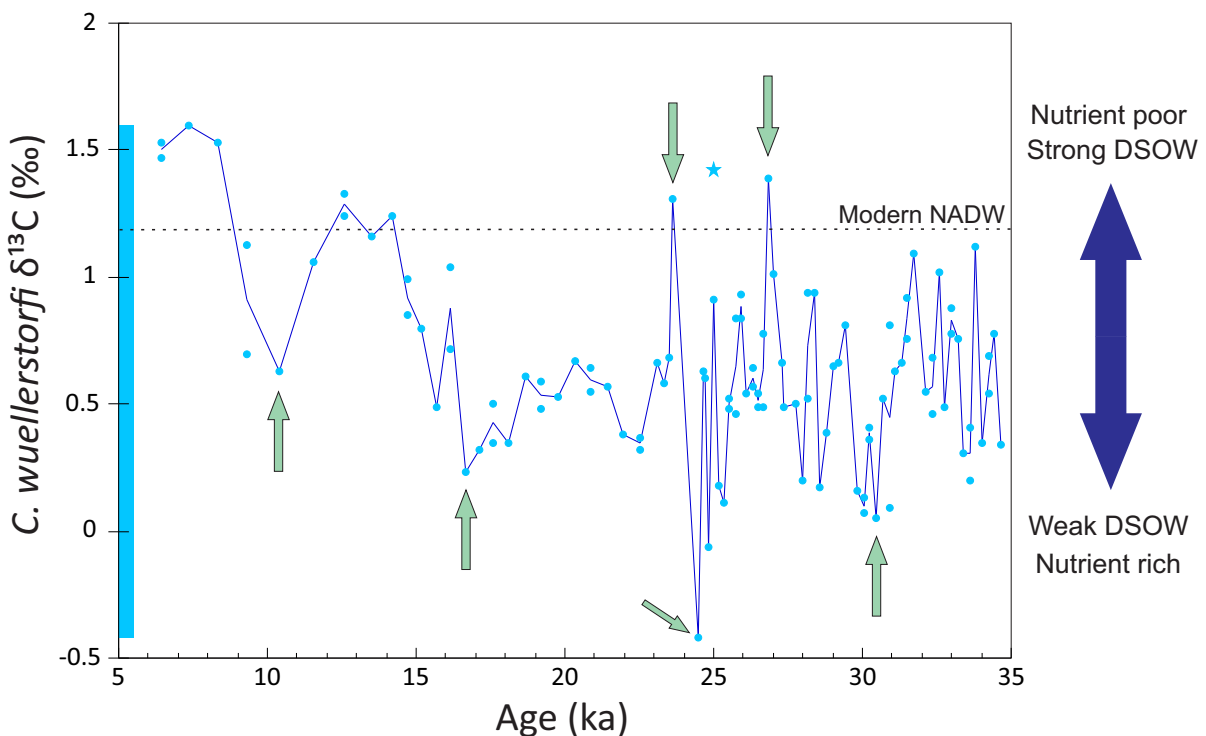


Figure 6.12: The benthonic $\delta^{13}\text{C}$ record (*C. wuellerstorfi*) from core GS15-196-02GC relative to VPDB plotted against age (ka BP). All measurements are shown (light blue) with the solid blue line tracing the average $\delta^{13}\text{C}$ values at every 4 cm core depth interval (when possible). The green arrows denote the events described in the text. Note that the interval from 23.6 ka–24.4 ka (111 cm–129 cm) only contains two data points. The blue bar represents the total range of variability. Further, the blue star represents $\delta^{13}\text{C}$ measurements believed to be incorrect due to incomplete reaction and/or insufficient removal of contaminants, and were not included in the calculations of the SD and average $\delta^{13}\text{C}$ values. The blue arrow represents the relative weakening and strengthening of ventilated deep water influences (DSOW), associated with lower and higher $\delta^{13}\text{C}$ values. Modern NADW (dashed horizontal line) value of 1.2‰ from Eide et al. (2017).

In general, the record shows similar trends as those observed in other deep Atlantic cores (e.g. (Labeyrie and Duplessy, 1985)), with glacial values around -0.5‰ to 0‰ and interglacial/Holocene values above 1‰. However, the record shows high amplitude variability during last the glacial period (between 25 ka-34 ka) and reaches values both associated with interglacial times (~1‰) and glacial times (<0‰) - indicating large and abrupt shifts in deep water ventilation in the Irminger Basin during that time.

7. DISCUSSION

It is commonly postulated that ice sheet dynamics and freshwater perturbations in the North Atlantic were linked to disruptions in deep water circulation and North Atlantic cooling in the past (e.g. (Rahmstorf, 1995; Clark et al., 2001; McManus et al., 2004)). However, the exact nature of climate-ocean-ice sheet coupling remains unclear and iceberg input and freshwater pulses have been hypothesized as both the trigger for (e.g. (Bond et al., 1993; Manabe and Stouffer, 1997)), and response to (e.g. (Marcott et al., 2011)), reduced AMOC. Differentiating between these hypotheses requires high-resolution records constraining the relative timing of ice sheet calving, freshwater perturbations and ocean circulation changes.

Particularly prominent in the North Atlantic IRD records are the Heinrich events. The origin and distribution of Heinrich layers, deposited in a large belt across the North Atlantic (40°N-55°N, (Ruddiman, 1977)), suggest that they are related to the abrupt collapse of the Laurentide Ice Sheet (Bond et al., 1993; Broecker, 1994) during cold Heinrich stadials. However, IRD derived from European (FIS and BIS) and Icelandic ice sheets have also been found in IRD rich layers associated with the Heinrich events, suggesting that other ice sheets were also actively calving at that time. In fact, “precursor” events of IRD derived from Europe and/or Iceland (Bond and Lotti, 1995; Grousset et al., 2000) have been found to be deposited prior to Heinrich events 1 and 2, suggesting that these ice sheets shared a similar timing to the LIS and may have preceded and even triggered LIS surging (Grousset et al., 2001). However, sediment cores co-registering Heinrich and non-Heinrich IRD as well as deep water circulation changes have not yet been available, hampering efforts to resolve their temporal and causal relationship.

Here I use my newly generated proxy records from core GS15-196-02GC, located in the Irminger Basin to constrain the relative timing and potential mechanistic relationship between IRD, freshwater input and ocean circulation disruptions. Evaluating the phasing relationship within the same sediment sequence allows for determination of the relative timing of events and avoids uncertainties inherent to core-to-core dating and correlation. The relative percentage of IRD together with magnetic susceptibility and XRF-records are used to monitor the occurrence of icebergs and differentiate between the potential sources of ice rafting, while planktonic oxygen isotopes provide insights into the physical properties (freshening) of the surface waters in the northern subpolar gyre region. Taken together with benthonic carbon

isotopes, the nature of bottom water ventilation/circulation changes and the timing relative to ice sheet calving and near-surface water freshening is evaluated.

7.1 Near-surface water properties

The near-surface water properties in the Irminger Sea during the last glaciation and subsequent deglaciation are derived from IRD counts and planktonic and benthonic $\delta^{18}\text{O}$ measurements from core GS15-196-02GC.

7.1.1 Ice rafted debris events

Core GS15-196-02GC from the Irminger Basin is situated along the main pathway for icebergs drifting from the Greenland, Nordic and Arctic Seas towards the North Atlantic Ocean and thus, is well positioned to sensitively monitor the glacial iceberg flux from circum-Nordic Seas sources (hereinafter including the entire GIS). Lithic grains documented in the core will therefore most likely originate from Greenland, Iceland, the Faroes Islands, Fennoscandia and/or the British Isles with an additional input possible from the Hudson Strait during large ice rafting events (Elliot et al., 1998). Comparison of the IRD record from core GS15-196-02GC with other IRD records from the North Atlantic, located both in (core MD95-2040) and outside (core GIK23415-9) of the Ruddiman IRD belt (Figure 7.1 and Table 7.1), shows that large IRD events found in core GS15-196-02GC occur with similar timing to IRD peaks associated with Heinrich events 1-3. These similarities suggest a connection between some of the largest IRD events in the Irminger Basin and the recognized H-event sequence. The IRD event around 16.6 ka - 17.1 ka corresponds to H1. However, there is a broad and split IRD peak in core GS15-196-02GC with only the first peak associated clearly in timing with H1. It is possible that the local IRD input outlasted the H-event, with greater input after the major ice rafting surge related to H1 had concluded, possibly related to the deglaciation occurring across the North Atlantic region. The IRD event corresponding to H2 occurred at 23.5 ka-24.6 ka and is the clearest IRD event in the Irminger Basin record. There is a third large IRD event between 30.4 ka and 30.6 ka, approximately coincident with H3. Notably, the scale of this IRD peak does not exceed some of the other non-Heinrich timed IRD peaks in the record, suggesting that locally, ice rafting during this period was not anomalously high relative to other non-Heinrich IRD events. This conforms to previous observations that, in the northern North Atlantic, IRD peaks are more common than in the Ruddiman IRD belt and IRD peaks are found for most cold intervals, not just Heinrich events (Hemming, 2004).

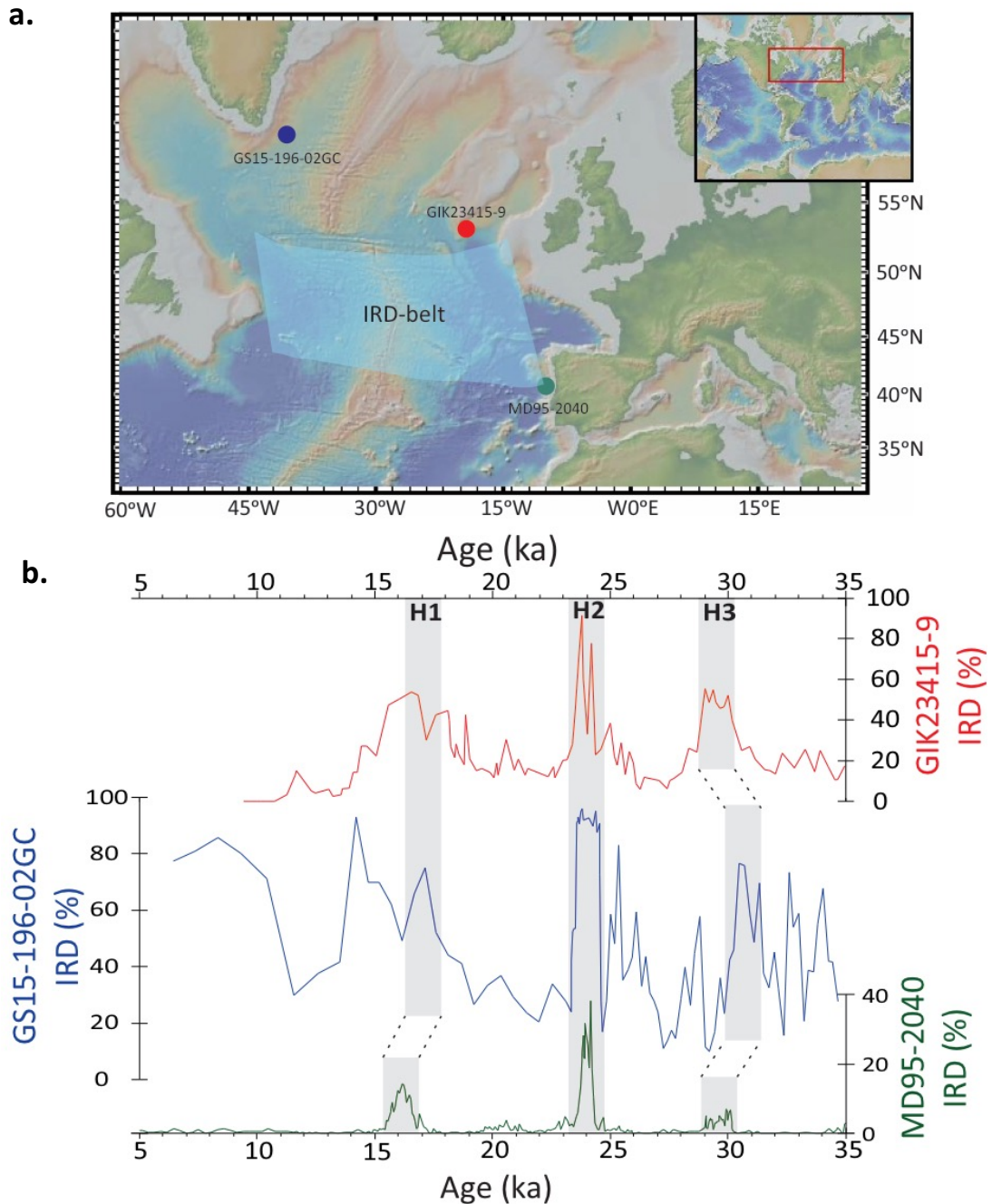


Figure 7.1: a. Map of cores used for comparison of the timing of IRD events in the North Atlantic. Blue shaded box represents the IRD belt defined by Ruddiman (1977). Modified from GeoMapApp (<http://www.geomapapp.org>) and Ryan et al. (2009). b. IRD record from core GS15-196-02GC (blue curve) compared to core MD95-2040 (green curve) and core GIK23415-9 (red curve). Grey shaded areas denote Heinrich events 1-3. The offset in timing for some of the H-events are marked by dotted lines. This offset is probably related to uncertainties in the different age models. See Table 7.1 for additional information about the different cores.

Table 7.1: North Atlantic sediment cores used for IRD (%) comparison.

Core	Location	Water depth	Proxy	Reference
GIK23415-9	53°17' N 19°14' W	2472 m	IRD (%)	(Weinelt, 2004)
MD95-2040	40°58' N 9°86' W	2465 m	IRD (%)	(de Abreu et al., 2003)

In order to further assess the possible influence of Hudson Strait vs. circum-Nordic Seas IRD sources in the Irminger Basin, the presence of detrital carbonate within the IRD rich layers were analysed. Increased amounts of Ca/Sr, reflecting layers rich in detrital carbonate and poor in biogenic carbonate are a characteristic of IRD sourced from the Laurentide Ice Sheet (Hudson Strait region) during Heinrich events (Hodell et al., 2008b). In core GS15-196-02GC, only minor increases in detrital carbonate (Ca/Sr) are found during the IRD events corresponding to Heinrich event 1-3 (Figure 7.2). Instead, increases in Si/Sr, reflecting layers that are poor in biogenic carbonate and rich in detrital silicate minerals (Hodell et al., 2008b) are found, conflicting with the idea that these IRD events represent Heinrich events sourced from the Hudson Strait and LIS. These findings indicate that large amounts of LIS derived IRD did not drift into the Irminger Basin during H-events. Thus, during the time of H1-H3 another region was the dominant source of icebergs and IRD in the Irminger Basin. In addition, low planktonic $\delta^{13}\text{C}$, at least during H1 and H3 (Figure 6.10 in Chapter 6), is consistent with an increased presence of polar-like water (Johannessen, 1992) conditions at the site; most likely due to advection of Nordic Seas icebergs and polar waters along the East Greenland current. Furthermore, peaks in magnetic susceptibility have commonly been used for identifying Heinrich layers in North Atlantic sediment cores (Hemming, 2004). However, there is no consistent increase in magnetic susceptibility (ms) during the major IRD peaks in core GS15-196-02GC (Figure 7.2), and only a short-lived (1 cm) increase during the IRD event associated with H2 is observed. Taken together, the absence of detrital carbonate, increases in detrital silicate and lack of clear magnetic susceptibility peaks in GS15-196-02GC suggest that the Laurentide Ice Sheet (Hudson Strait) was not the dominant source of icebergs to the Irminger Basin during H1-H3.

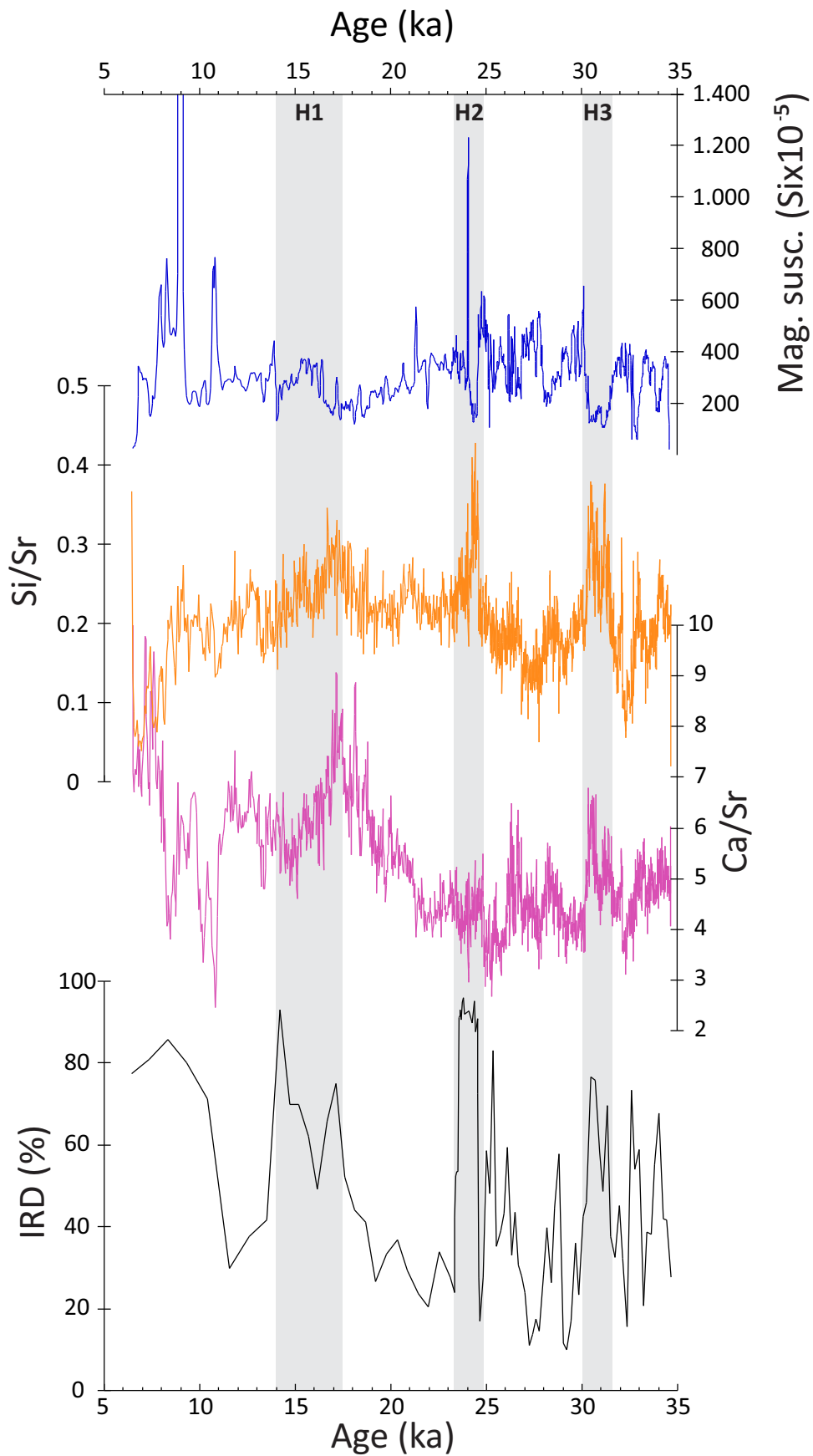


Figure 7.2: Magnetic susceptibility (blue curve), Si/Sr (orange curve), Ca/Sr (pink curve) and Ice rafted debris (%) (black curve) from GS15-196-02GC plotted against age (ka BP). Grey shaded boxes represent IRD H-events 1-3 discussed in the text.

Still, the coincidence in timing of local IRD events with Heinrich events 1-3 points towards a possible connection. Sedimentological proxies (ms, Ca/Sr, Si/Sr) suggest that the IRD-layers associated with H1-H3 in the Irminger Basin do not have the signature of Hudson Strait/LIS sourced Heinrich layers. The proximity of the core to southeast Greenland and the East Greenland Current points toward an IRD origin either from east Greenland or other circum-Nordic Seas sources such as the Fennoscandian, British or Icelandic ice sheets. Indeed, IRD sourced from the Icelandic (Bond and Lotti, 1995) and European ice sheets (Grousset et al., 2000; Knutz et al., 2007) have been found in IRD rich layers associated with Heinrich events, suggesting that active calving also occurred in other regions at that time. Furthermore, during Heinrich events 1 and 2, “precursor” events delivering IRD from Europe and Iceland, preceding IRD derived from the Hudson Strait have been identified (Grousset et al., 2001). Consequently, the European, Icelandic and Greenland ice sheets could have released icebergs prior to the massive iceberg discharges from the Laurentide Ice Sheet, identifying Greenland/Europe/Iceland as a possible starting point for the ice sheet destabilization in the North Atlantic region during Heinrich events (Grousset et al., 2001). However, given that the magnetic susceptibility record shows no consistent increase during the Heinrich events an Icelandic source seems less likely than FIS/BIS and/or GIS. Although the results of this study are consistent with this picture, they also document numerous IRD events that do not coincide with Heinrich events, suggesting that if iceberg calving from other ice sheets is a trigger, it is not the only precondition for a Heinrich event. Other factors such as the size/instability of the Laurentide Ice Sheet (MacAyeal, 1993) or feedbacks/forcings such as decreased overturning circulation and increased subglacial melt (Marcott et al., 2011) might also be critical.

7.1.2 Low planktonic $\delta^{18}\text{O}$ anomalies

Further assessment of the temporal relationship between potential IRD “precursors” recorded in the Irminger Basin and major H-event iceberg discharges requires a local proxy for H-events. Here I use planktonic $\delta^{18}\text{O}$ as an indicator of large freshwater input to the subpolar North Atlantic. Similar to the IRD belt to the south, the Heinrich related IRD peaks in GS15-196-02GC coincide with low planktonic (*N. pachyderma* (s)) $\delta^{18}\text{O}$, indicating clear changes in the subpolar gyre near-surface water hydrography (temperature and salinity) (Figure 7.3) during these events. Other studies on foraminifera assemblages (Cortijo et al., 1997), dinoflagellate cyst assemblages (de Vernal and Hillaire-Marcel, 2000) and planktonic $\delta^{18}\text{O}$ (Maslin et al., 1995) in the subpolar gyre region reveal a dramatic reduction in both temperature and salinity

at the ocean surface during Heinrich events, and attribute this cooling and freshening to large delivery and subsequent melting of icebergs. In planktonic $\delta^{18}\text{O}$ the cooling (increases the $\delta^{18}\text{O}$) and freshening (decreases the $\delta^{18}\text{O}$) drive opposing changes with the low $\delta^{18}\text{O}$ freshwater signal dominating over the cooling during Heinrich events, resulting in clear anomalies with amplitudes of -1‰ or more in the North Atlantic (Cortijo et al., 1997; Hemming, 2004) and the subpolar gyre (de Vernal and Hillaire-Marcel, 2000). Hence, the low planktonic $\delta^{18}\text{O}$ anomalies in GS15-196-02GC associated with H1-H3 likely represent the local expression of this large near-surface freshening (and $\delta^{18}\text{O}$ decrease) observed previously in relation to H-events.

It is notable that there are a number of IRD peaks nearly equivalent to the scale of the IRD-events associated with H1-H3 that occur without accompanying planktonic $\delta^{18}\text{O}$ decreases (e.g. events a-e in Figure 7.3). The absence of low $\delta^{18}\text{O}$ anomalies during these ice rafting events suggest that little or no surface water property (temperature and salinity) changes occurred in association with non-Heinrich timed IRD peaks, consistent with findings by Elliot et al. (1998). The stable $\delta^{18}\text{O}$ values during these IRD events can be explained by any of the following mechanisms. The SSTs in the Irminger Basin were sufficiently low at the time of increased iceberg discharge so that only a small portion of the icebergs melted, introducing less meltwater locally and perhaps leading to weaker $\delta^{18}\text{O}$ anomalies. In addition, $\delta^{18}\text{O}$ values of iceberg meltwater reflect the ice sheet of origin. Snow deposited centrally and at high altitude on large continental ice sheets (e.g. Laurentide Ice cap) far away from the ocean would have lower $\delta^{18}\text{O}$ values (\sim -40‰ SMOW) than snow deposited on smaller, coastal ice sheets (e.g. ice sheets bordering the Nordic Sea region) (\sim -20‰ SMOW) (Dansgaard and Tauber, 1969). Hence, the effect of a less isotopically depleted iceberg source might explain the absence of clear negative $\delta^{18}\text{O}$ anomalies during non-Heinrich ice rafting events. Finally, and perhaps most significant, the total amount of freshwater released during non-Heinrich IRD peaks was likely much less, and although IRD was routed past the site, the overall subpolar gyre freshening was simply too small to be observed in planktonic $\delta^{18}\text{O}$.

Regardless of why, large $\delta^{18}\text{O}$ anomalies appear to only occur during large Heinrich-related freshwater inputs, consistent with previous findings. Thus, large $\delta^{18}\text{O}$ anomalies can be used as a proxy for the timing of Heinrich related freshwater fluxes and subpolar gyre freshening. One possible scenario is that during H-events the LIS icebergs melted further south in the subpolar gyre within the Ruddiman IRD-belt. The associated IRD would be deposited there, whereas the

freshwater signal could be advected within the surface waters in the subpolar gyre - influencing the core site and producing the large, low $\delta^{18}\text{O}$ anomalies observed there. This would explain why the low planktonic $\delta^{18}\text{O}$ anomaly is observed more broadly throughout the subpolar region than the Heinrich related IRD signal derived from LIS.

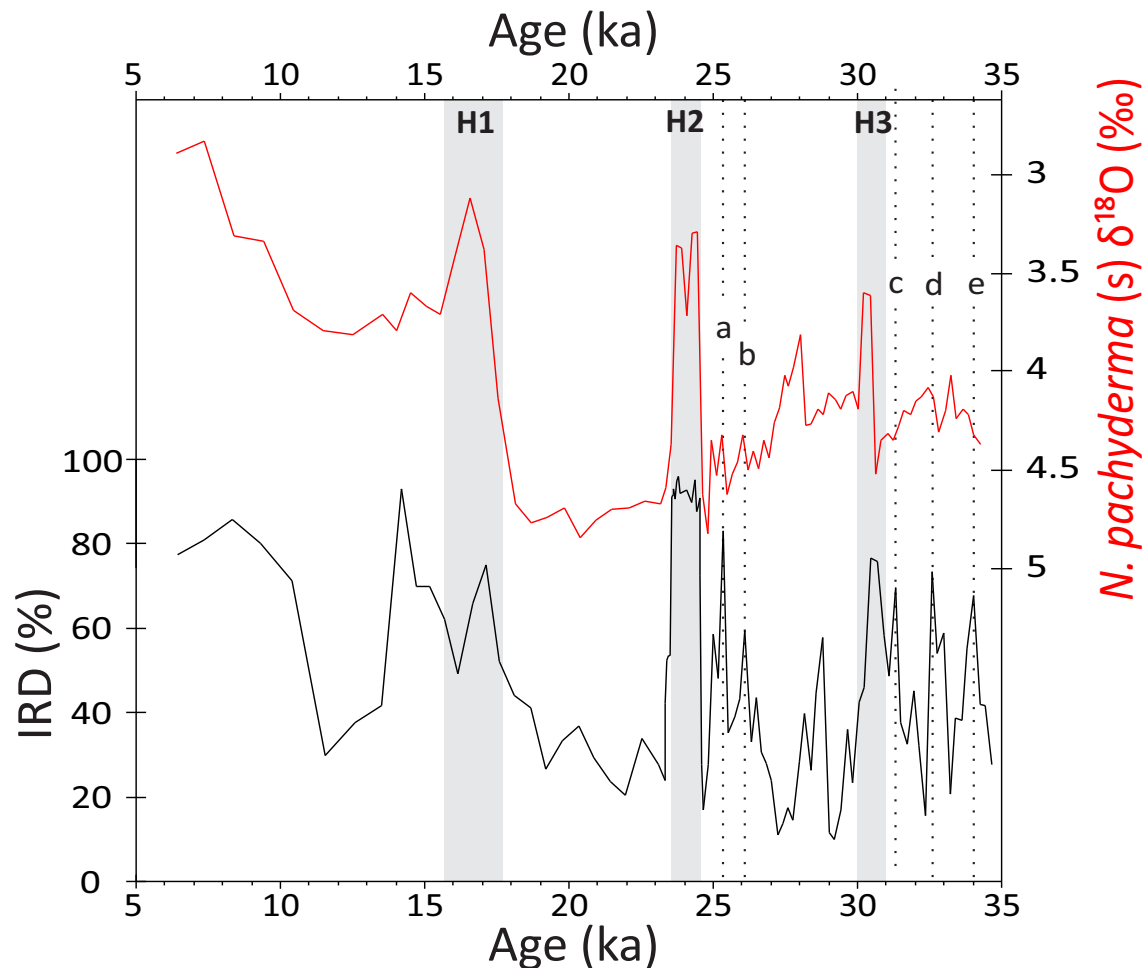


Figure 7.3: GS15-196-02GC ice rafting events (%) (nr.1-3) and *N. pachyderma* (s) $\delta^{18}\text{O}$ values relative to VPDB plotted against age (ka BP). Grey shaded boxes denote IRD events 1-3 described in the text, dotted line denotes detrital events (a-e) without accompanying low $\delta^{18}\text{O}$ anomalies.

For the IRD events associated with H1 and H3 the IRD increase and $\delta^{18}\text{O}$ decrease appears to occur near simultaneously, indicating that the local iceberg fluxes and near-surface water freshening driven by the LIS are closely coupled. However, close inspection shows that during the H2 related IRD event, the planktonic $\delta^{18}\text{O}$ decrease is delayed relative to the IRD increase by 4 cm (~200 years). This suggests that the freshening at this location may have occurred after iceberg input had started to peak. In addition, smaller IRD peaks and/or a trend of increasing IRD, without accompanying $\delta^{18}\text{O}$ reductions (labelled as events a to e in Figure 7.3) occur prior

to the low $\delta^{18}\text{O}$ anomalies associated with H2-H3. These IRD peaks could represent “precursor” events, which were not large enough to trigger LIS collapse and were simply too small to produce an associated low $\delta^{18}\text{O}$ anomaly in the subpolar gyre. If this inference is correct, and the main source of freshwater (low planktonic $\delta^{18}\text{O}$ anomalies) to the subpolar region was the LIS (due to its large ice volume and low $\delta^{18}\text{O}$ ice values), then some offsets between local IRD (non-LIS sourced) and planktonic $\delta^{18}\text{O}$ are possible. Seen in this way, the slight lead of IRD over $\delta^{18}\text{O}$ during H-events would suggest calving of various ice sheets in the North Atlantic region, with perhaps the circum-Nordic Seas ice sheets calving first.

In summary, if the massive iceberg discharges from the LIS during Heinrich events 1-3 occurred as a response to some external climatic forcing, it is likely that other nearby ice sheets such as the Fennoscandian, British or Greenland ice sheets may have had a similar response, delivering IRD to the core site during H1-H3. If all ice sheets surrounding the North Atlantic released armadas of icebergs in near synchrony, rapid interaction between the ice sheets or a more global forcing must have caused the events (e.g. changes in ice shelf dynamics, sea level or basal melt rates). Thus, a major issue in understanding the dynamics of Heinrich events relies on whether or not the Northern Hemisphere ice sheets underwent synchronous iceberg discharge. Previous findings of “precursor” events (e.g. (Grousset et al., 2001)) from Europe/Fennoscandia, deposited prior to large Hudson strait Heinrich events, are in agreement with the IRD-event sequence identified in this study. Increased “precursor” iceberg discharge from the ice sheets in the circum-Nordic Seas region could cause a small sea level rise (Bond and Lotti, 1995) perhaps enough to trigger a collapse of the LIS, releasing large amounts of IRD and freshwater (and producing low $\delta^{18}\text{O}$ anomalies), during Heinrich events. A second possible mechanism that may cause and explain near-ice sheet synchronicity involves changes in ocean circulation. Reduced overturning circulation (AMOC) has been hypothesized as a trigger for ice shelf collapse because it increases the sea level and subsurface ocean warming, which in turn increases the rate of basal melting underneath ice shelves (Marcott et al., 2011). If “precursor” IRD events were associated with changes in ocean circulation, this might explain widespread coherence between different ice sheets as ice sheets across the North Atlantic would experience a common forcing.

7.2 Deep water mass geometry in the North Atlantic during the last glaciation

Here I assess whether changes in ocean circulation occurred together with ice sheet variability using benthonic foraminifera $\delta^{13}\text{C}$. Benthonic $\delta^{13}\text{C}$ is generally used as an indicator for past changes in bottom water nutrient content and ultimately ventilation (Eide et al., 2017). Downcore benthonic $\delta^{13}\text{C}$ changes commonly reflect the geometry and redistribution of low and high $\delta^{13}\text{C}$ water masses in the ocean interior and thus, provide information about the influence and circulation of these water masses in the past (e.g. (Curry et al., 1988; Curry and Oppo, 2005)).

The highly oscillating GS15-196-02GC benthonic (*C. wuellerstorfi*) $\delta^{13}\text{C}$ record indicates that substantial changes in bottom water nutrient chemistry and ventilation occurred between 35 ka-5 ka ago (Figure 7.4). There are three low $\delta^{13}\text{C}$ events occurring together with light $\delta^{18}\text{O}$ values, whose age coincide with Heinrich events 1-3. For the low $\delta^{13}\text{C}$ event associated with H1, minimum $\delta^{13}\text{C}$ value is 0.23‰. The second low $\delta^{13}\text{C}$, associated with H2, show a minimum value of -0.42‰. This event has a maximum duration of ~800 years, after which the $\delta^{13}\text{C}$ values recover to values of 1.31‰. Lastly, the low $\delta^{13}\text{C}$ event associated with H3 show minimum values of 0.05‰.

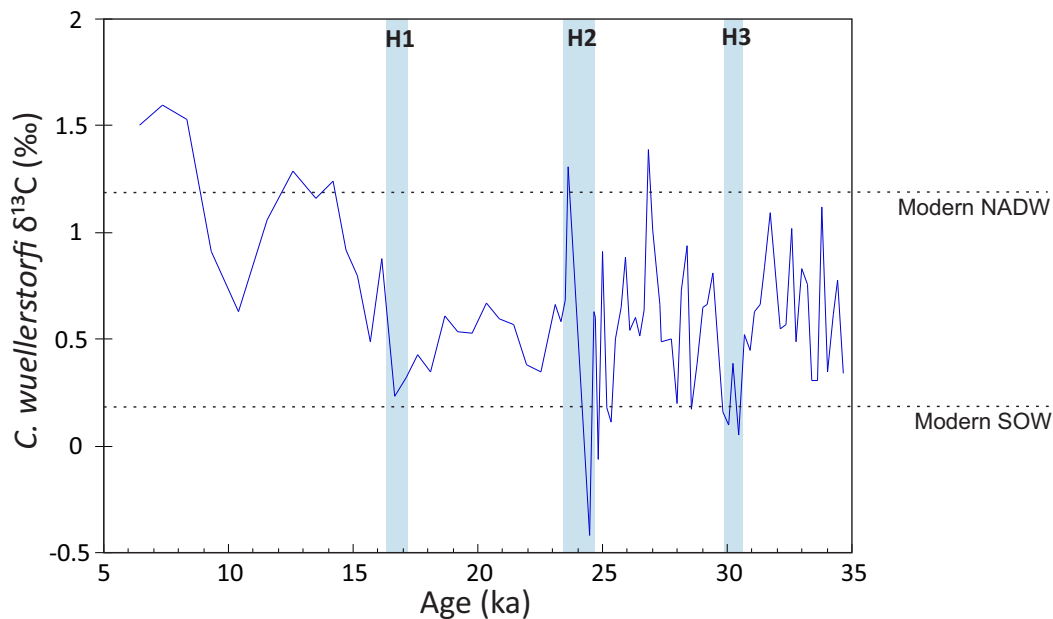


Figure 7.4: GS15-196-02GC benthonic $\delta^{13}\text{C}$ relative to VPBD plotted against age (ka BP). Dotted lines indicate modern NADW (preindustrial) in the North Atlantic (Eide et al., 2017) at depths of ~2500m and modern SOW (preindustrial) (Eide et al., 2017) values. H-events are marked according to the HE-chronology from the GS15-196-02GC core.

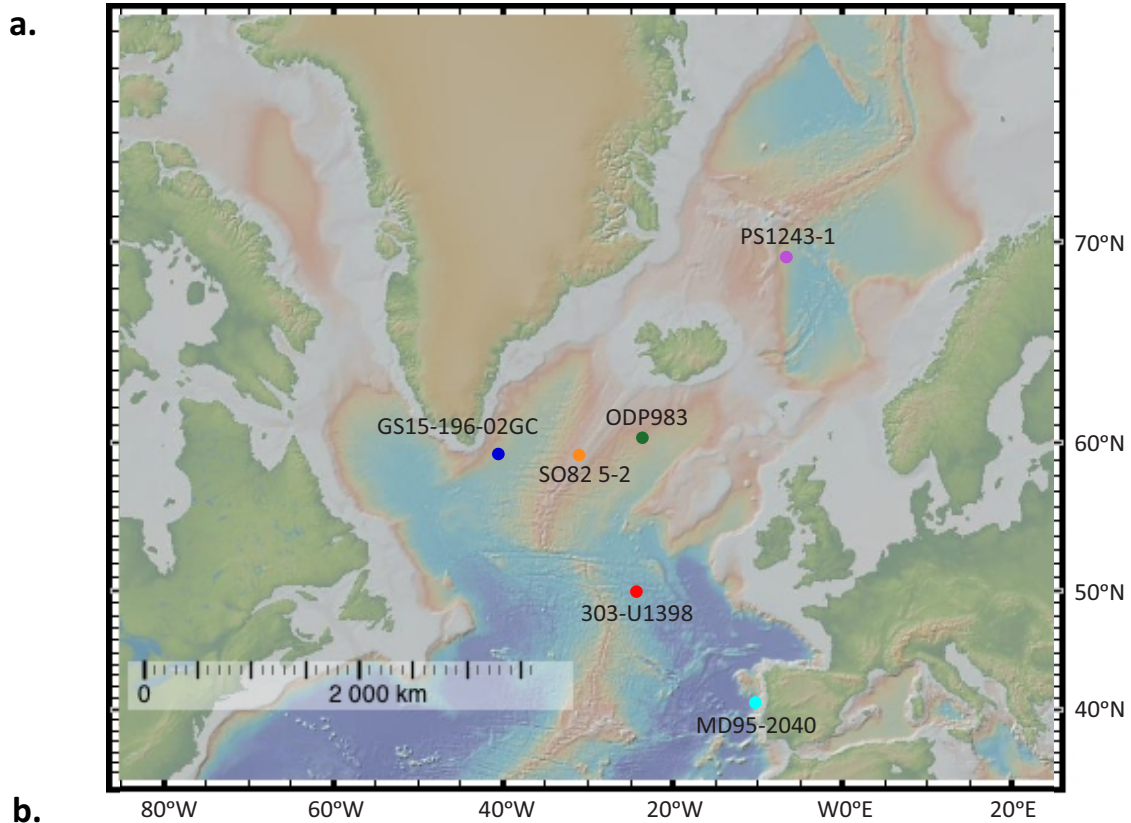
During the last glaciation, benthonic (*C. wuellerstorfi*) $\delta^{13}\text{C}$ values decrease relative to both modern NADW (Eide et al., 2017) and Holocene (Figure 7.4) values. However, several abrupt jumps to near-modern NADW values indicate that the bottom water at the core site experienced short-term increases in the influence of “NADW-like” water masses. There are two possible explanations for the reductions in benthonic $\delta^{13}\text{C}$: (1) A southward shift in the location (to south of Iceland) of open convection and formation of NADW, where the surface waters did not become dense enough to sink to similar depths as today, reaching only intermediate depths, perhaps to depths as shallow as 1500 m. Thus, allowing for a stronger influence of Southern Ocean Source Waters (SOW) (containing lower $\delta^{13}\text{C}$ values) in the deep North Atlantic (Curry and Oppo, 2005). This could cause a substantial cooling across the northern North Atlantic and southward expansion of sea ice (Rahmstorf, 2006). In general, the mixing zone of Northern Source Waters (NSW) and SOW during glacial times has been defined to be between 2000-2500 m water depth in the North Atlantic (Curry et al., 1988; Duplessy et al., 1988; Curry and Oppo, 2005). Hence, the proximity of this study site (2468 m) to the proposed mixing zone of NSW and SOW, could explain the high variability in the benthonic $\delta^{13}\text{C}$ during the last glacial period. (2) Alternatively, Thornalley and colleagues (2010) postulated that increasing sea ice formation in the Nordic Seas, leading to brine rejection, could produce a low $\delta^{13}\text{C}$ water mass that mixed with Glacial North Atlantic Intermediate water (GNAIW) and was transported out of the Nordic Seas across the GSR and potentially into the Irminger Basin. Thus, the low $\delta^{13}\text{C}$ values would be attributed to the Nordic Seas and not the Southern Ocean.

In order to further characterize the distribution of low $\delta^{13}\text{C}$ bottom water and identify its origin, the *C. wuellerstorfi* $\delta^{13}\text{C}$ record from GS15-196-02GC was compared to *C. wuellerstorfi* $\delta^{13}\text{C}$ records from four other North Atlantic sediment cores (Figure 7.5). The cores are located to the north and south of the Irminger Basin core (GS15-196-02GC, 2468 m water depth), as well as deeper (e.g. 3871 m water depth) and shallower (e.g. 1495 m water depth) (Table 7.2). The shallower cores (SO82 5-2 and ODP983) and the core in the Nordic Sea (PS1243-1) have higher $\delta^{13}\text{C}$ values relative to GS15-196-02GC during the last glaciation, demonstrating that deep water in the Irminger Sea is less like the deep water in the Nordic Seas and the shallower water masses at that time. Meanwhile, the Iberian margin core (MD95-2040 (south of core GS15-196-02GC and similar depth (2465 m)) and 303-U1308 core (south of core GS15-196-02GC and deeper (3871 m)), show similar $\delta^{13}\text{C}$ values to GS15-196-02GC, especially during the last glaciation. Hence, during the last glaciation, benthonic $\delta^{13}\text{C}$ values from the Irminger Basin at

a water depth of 2468 m show similar deep water $\delta^{13}\text{C}$ values as southern and deeper sites, and are distinctly lower than values from northern and shallower sites. This is consistent with the global ocean $\delta^{13}\text{C}$ gradient (Kroopnick, 1985), as well as the glacial Atlantic $\delta^{13}\text{C}$ distribution (Curry and Oppo, 2005), where deeper and southern sites are expected to have lower $\delta^{13}\text{C}$ values. Further, the $\delta^{13}\text{C}$ dissimilarity between the Irminger Basin (low $\delta^{13}\text{C}$) and the Nordic Sea (higher $\delta^{13}\text{C}$) is inconsistent with the hypothesis that the low $\delta^{13}\text{C}$ bottom water originated from Nordic Seas sources e.g. via brine rejection and subsequent transport across the GSR. In addition, near simultaneous benthonic $\delta^{13}\text{C}$ lows during H2 and H3 in cores GS15-196-02GC, 303-U1308 and MD95-2040 suggests major reorganization of the deep water masses during Heinrich events.

Table 7.2: North Atlantic cores used for comparison of benthonic (*C. wuellerstorfi*) $\delta^{13}\text{C}$.

Core	Location	Water depth	Proxy	Reference
PS1243-1	69°37' N 6°55' W	2711 m	<i>C. wuellerstorfi</i> $\delta^{13}\text{C}$	(Bauch et al., 2001)
ODP983	60°24' N 23°38' W	1983 m	<i>C. wuellerstorfi</i> $\delta^{13}\text{C}$	(Channell et al., 1997)
303-U1308	49°87' N 24°23' W	3871 m	<i>C. wuellerstorfi</i> $\delta^{13}\text{C}$	(Hodell et al., 2008a; Hodell et al., 2008b)
SO82 5-2	59°18' N 30°90' W	1416 m	<i>C. wuellerstorfi</i> $\delta^{13}\text{C}$	(van Kreveld et al., 2000a; van Kreveld et al., 2000b)
MD95-2040	40°58' N 9°86' W	2465 m	<i>C. wuellerstorfi</i> $\delta^{13}\text{C}$	(de Abreu et al., 2003)



- b.
- Legend
- PS1243-1 (2711 m)
 - SO82 5-2 (1415 m)
 - ODP983 (1983 m)
 - GS15-196-02GC (2468 m)
 - 303-U1398 (3871 m)
 - MD95-2040 (2465 m)

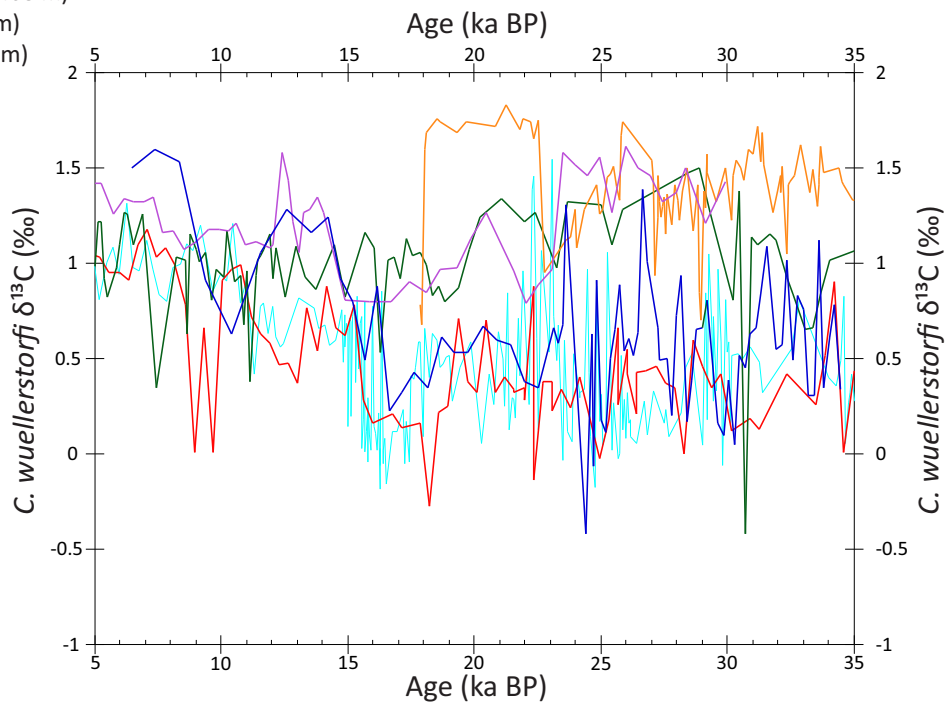


Figure 7.5: b. Comparison of benthonic (*C. wuellerstorfi*) $\delta^{13}\text{C}$ relative to VPDB plotted against age (ka BP). See legend for core depths and map (a.) for core locations. Additional information about the cores can be found in Table 7.2. The map is generated using GeoMapApp (<http://www.geomapapp.org>) (Ryan et al., 2009).

7.3 Timing of ice sheet calving, freshwater perturbations and ocean circulation

The low $\delta^{13}\text{C}$ anomalies in the Irminger Basin most likely indicate reductions in the formation/presence of NADW. In model simulations, reduced density or formation of NADW is often driven by surface freshening (Stouffer et al., 2006) and is associated with a slowdown of the AMOC. Both the initial decreases in benthonic $\delta^{13}\text{C}$ and small “precursor” IRD events started 500-2000 years before the major IRD and freshening peaks associated with H2 and H3 (Figure 7.6), suggesting that circum-Nordic Seas ice sheets released icebergs coinciding with the start of AMOC slow down and prior to LIS derived Heinrich events. However, decreases in benthonic $\delta^{13}\text{C}$ of similar scale as during Heinrich events occur without accompanying peaks in IRD and $\delta^{18}\text{O}$, suggesting that circulation changes are not always linked to increased iceberg activity. The abrupt increases in benthonic $\delta^{13}\text{C}$ after Heinrich events 1 and 3, and during the final stage of H2, suggests that the AMOC resumes to its full strength quickly after (400-800 years for H1 and H3, or during for H2) the Heinrich events, possibly related to a cessation/reduction of freshwater fluxes.

Initial decreases in benthonic $\delta^{13}\text{C}$ associated with reduced deep water formation in the northern North Atlantic are closely coupled to increases in non-LIS sourced IRD (Figure 7.7). There are a number of potential mechanisms by which IRD and freshwater delivery in the circum-Nordic Seas and deep water formation could be linked. (1) Increased non-LIS IRD delivered to key deep water formation regions (e.g. the Nordic Seas) could decrease buoyancy and reduce the density and/or the rate of deep water formation. A persistent input of freshwater and reduced deep water formation would cause subsurface warming and basal melting of circum-North Atlantic marine terminating ice sheets (Marcott et al., 2011). This in turn would act as a feedback, further destabilizing circum-North Atlantic ice sheets, increasing the freshwater fluxes and eventually triggering LIS collapse. Alternatively, (2) any initial reduction of deep water formation is likely to warm the subsurface ocean. Smaller ice sheets (e.g. circum-Nordic Seas) may react more sensitively to the subsurface warming and increased basal melt, potentially explaining “precursor” IRD in the Irminger Basin (with no corresponding planktonic low $\delta^{18}\text{O}$ anomaly due to “small” events). The ongoing ice sheet decay would then help to sustain and strengthen the initial reduction in deep water formation through increased freshwater fluxes. If persisted long enough, the basal melt would eventually trigger collapse of larger ice sheet systems such as the LIS, producing the major low $\delta^{18}\text{O}$ anomaly and freshening

of the subpolar gyre. Both of these closely related models are based on the idea that reduced convection may cause the subsurface oceanic layer to warm, increasing the basal melting under the Laurentide ice sheet (and other ice sheets surrounding the North Atlantic) and, after crossing a certain (but unknown) threshold, sudden ice shelf collapse occurs (Marcott et al., 2011).

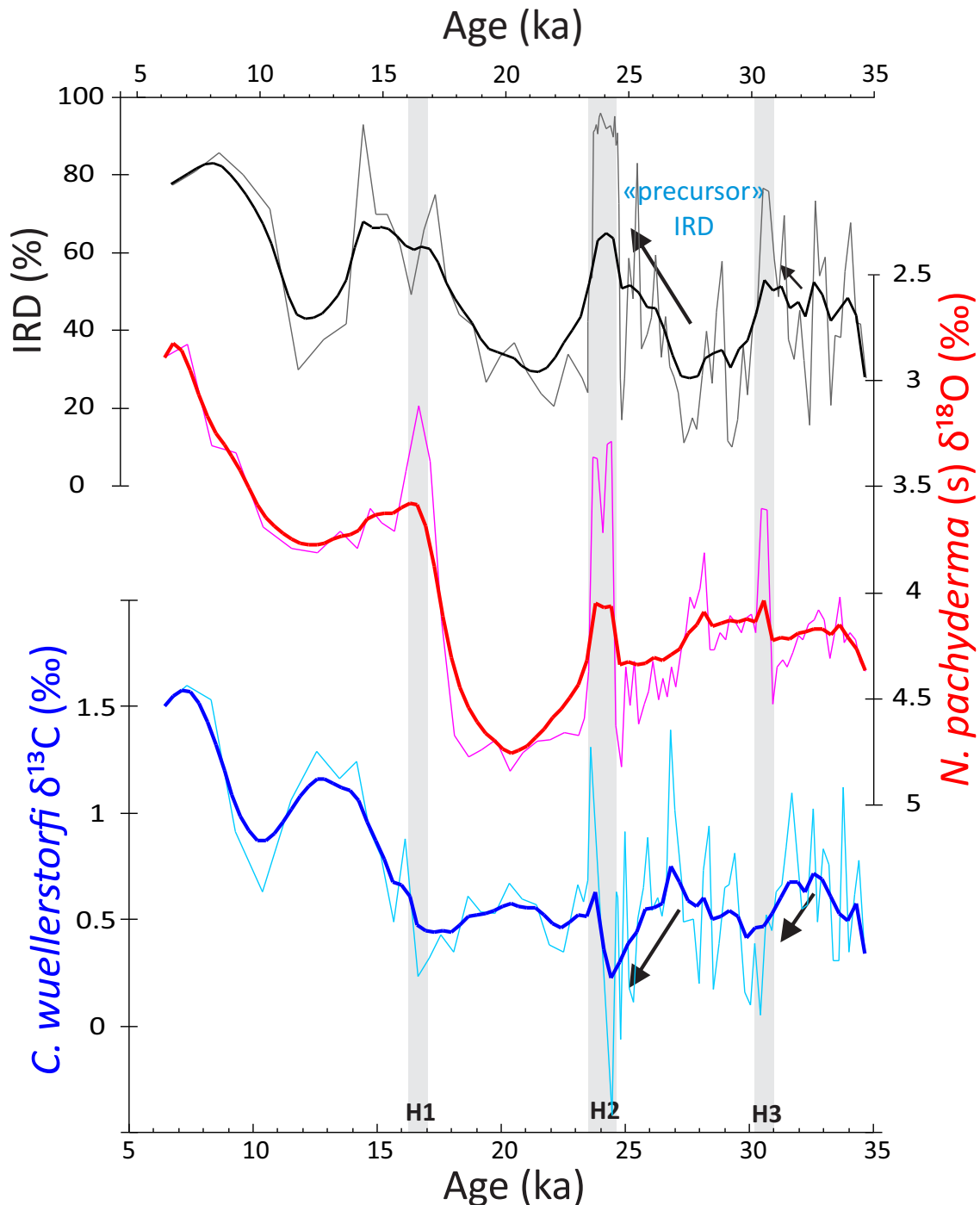


Figure 7.6: GS15-196-02GC Smoothed (dark blue) and average (bright blue) *C. wuellerstorfi* $\delta^{13}\text{C}$ and smoothed (red) and average (pink) *N. pachyderma* (s) $\delta^{18}\text{O}$ relative to VPDB, compared to smoothed IRD% (black) and average IRD% (grey) plotted against age (ka). Arrows denote trend of decreasing benthonic $\delta^{13}\text{C}$ and increasing IRD prior to H3 and H2. Prior to H2 a trend of increasing IRD% is clear.

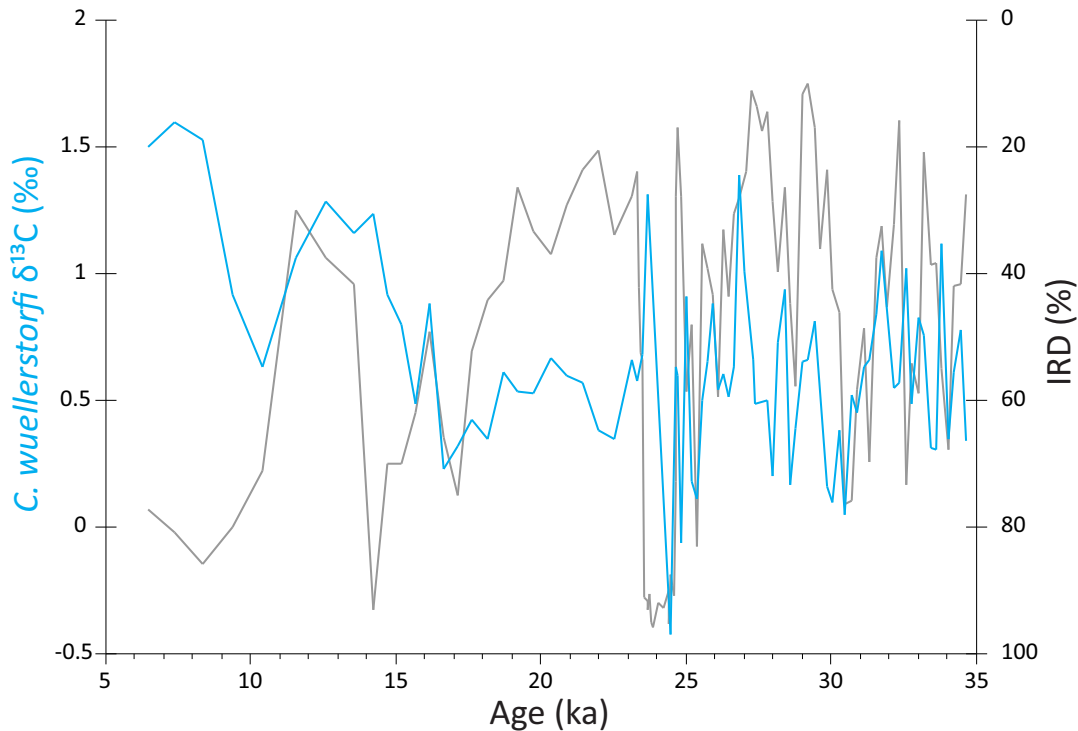


Figure 7.7: Flipped GS15-196-02GC IRD (%) record (grey) superimposed on benthonic (*C. wuellerstorfi*) $\delta^{13}\text{C}$ (blue) relative to VPDB plotted against age (ka BP). For the most part the records are closely coupled with increasing IRD occurring together with decreasing benthonic $\delta^{13}\text{C}$.

Indeed, models show that when AMOC is strongly reduced in response to freshwater forcing, the subsurface North Atlantic warms. The warming is stronger when freshwater is added in the high-latitude North Atlantic (e.g. the Nordic Seas) (Mignot et al., 2007) (see Figure 7.8). However, in order to better quantify this possible sequence of events, temperature reconstructions (Mg/Ca) on benthonic foraminifera (at intermediate depths) are needed to assess whether the subsurface waters in the Irminger Sea actually warmed prior to or during H-events. Such reconstructions have been done in NW Atlantic sites, showing basin-wide subsurface warming (Rasmussen et al., 2003) coupled with AMOC reductions occurring 1-2 kyr prior to H-events (Marcott et al., 2011).

Regardless of how the ocean-ice feedback is initiated, the IRD and benthonic $\delta^{13}\text{C}$ records from the Irminger Basin indicate a close coupling. For H2-H3, initial reductions in deep water formation and increased deliverance of IRD occurs prior to H-events related to massive surges of the Laurentide Ice sheet (seen as peak freshening in the planktonic $\delta^{18}\text{O}$ record). The IRD record suggests that ice sheets in the circum-Nordic Seas, responding prior to the LIS (leading H-events as recorded by planktonic $\delta^{18}\text{O}$), could be involved in triggering Hudson Strait H-

events. Conversely, the new record clearly indicates that LIS freshwater delivery related to H-events was not the initial trigger for reductions in deep water ventilation since deep water changes precede the H-events.

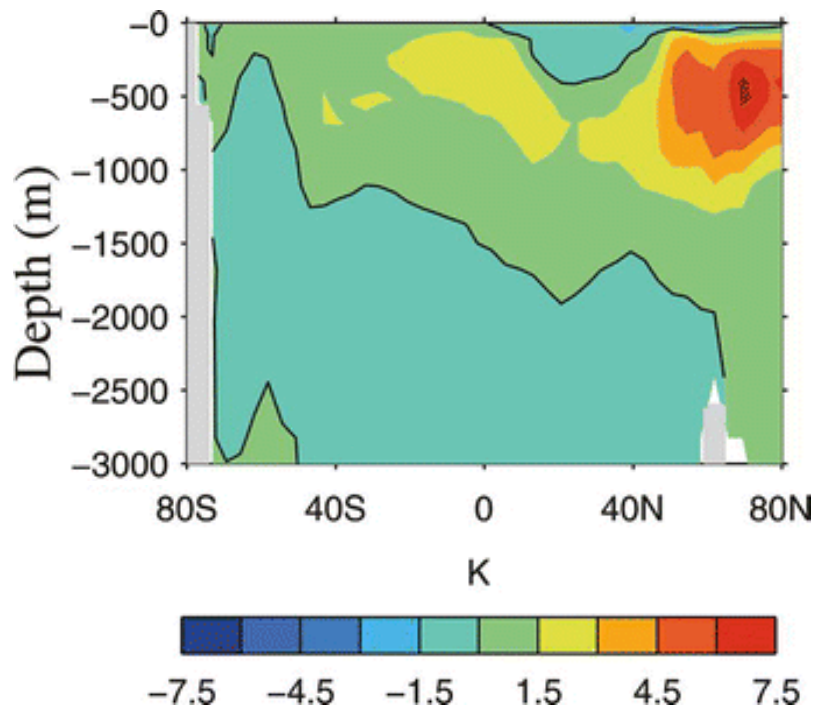


Figure 7.8: Modelled subsurface warming in the North Atlantic after 100 years of freshwater forcing in the high-latitude North Atlantic (50°-80°N), where AMOC gets strongly reduced. The scale bar show the temperature anomalies in K. Black line = 0K (modified from Mignot et al. (2007)). Note the anomalous warming in the subsurface water masses in the northern North Atlantic/Nordic Seas.

The abrupt recovery of deep water ventilation either, immediately after LIS collapse, or during in the case of H2, is revealing. This suggests that deep water is able to recover immediately following, or even prior to, the end of the low $\delta^{18}\text{O}$ anomaly and IRD peak, when the subpolar gyre is anomalously fresh. This further suggests that the deep water ventilation at the site may not be controlled solely by subpolar gyre freshwater forcing. Instead, the freshwater budget in the Nordic Seas may be more important than in the subpolar gyre, since recovery occurs when the subpolar gyre is fresh (low $\delta^{18}\text{O}$). Today, the bottom water flow at the site is DSOW. As the densest overflow emanating from the Nordic Seas, situated near the interface between northern and southern sourced deep water, this overflow might be particularly sensitive to density changes in the Nordic Seas source region.

7.3.1 Perspective on North Atlantic climate oscillations during the last glaciation

Having resolved the relative timing of ice sheet (IRD) and deep water circulation (benthonic $\delta^{13}\text{C}$) changes, it is interesting to consider how this relates to the North Atlantic climate during the last glaciation. Henry et al. (2016) found that AMOC is reduced during every cold Greenland stadial, suggesting that overturning circulation was systematically involved in D-O climate variability during Marine Isotope Stage 3 (MIS3). However, their study did not provide an IRD record, making it difficult to assess how millennial changes in the AMOC are related to ice sheet dynamics and freshwater forcing. When comparing the GS15-196-02GC IRD and benthonic $\delta^{13}\text{C}$ with the $\delta^{18}\text{O}$ record from the Greenland Ice core NGRIP, cold stadial conditions approximately coincide with IRD increases and smaller benthonic $\delta^{13}\text{C}$ decreases (Figure 7.9). This is similar to findings by Lekens et al. (2006) who found increasing IRD at the end of every D-O cold stadial in the Nordic Seas. Thus, each D-O event not only shows a decrease in deep water ventilation (Henry et al., 2016), but there is also growing evidence (Lekens et al., 2006; this thesis) for increases in circum-Nordic Seas sourced IRD. Given that the deepest constituents of NADW (e.g. DSOW) may be particularly sensitive to freshwater forcing within the Nordic Seas it is plausible that this smaller freshwater forcing proximal to deep water convection sites played a role in modulating circulation patterns on millennial timescales. Indeed, models suggest that the freshwater forcing proximal to convection sites is at least, if not more, important than the amount of freshwater applied (e.g. (Mignot et al., 2007; Morrill et al., 2014)).

If circum-Nordic Seas IRD (freshwater) is critical in modulating deep ocean circulation patterns over D-O cycles, a systematic relationship between benthonic $\delta^{13}\text{C}$ and IRD is to be expected from my record; similar to what is observed during H-events. However, the GS15-196-02GC record, does not show as convincing and systematic decreases in benthonic $\delta^{13}\text{C}$ during D-O stadials as those recorded in the Henry et al. (2016) study. It might be that the GS15-196-02GC core is too shallow (2468 m water depth, near the upper lobe of DSOW) to record smaller fluctuations (shoaling) in the water mass boundaries during D-O events and only registers the largest perturbations in deep ventilation (e.g. during Heinrich events). This is consistent with the Henry et al. (2016) study which found that the largest deep circulation anomalies occur associated with H-events. In addition, the Henry et al. (2016) study found only relatively modest deep water reductions during D-O stadials in the interval spanned by my core, making these events particularly difficult to record unless the core is close to the water mass boundary. The

core used in Henry et al. (2016) is substantially deeper (4541 m water depth) and might be more ideally located to record smaller deep water variability coupled with D-O events. Similar records from a deeper core near the core location of GS15-196-02GC, portraying both the Nordic Seas freshwater forcing (IRD) and fluctuations in the lower limit of DSOW would be able to test this hypothesis, and should be a for priority future studies.

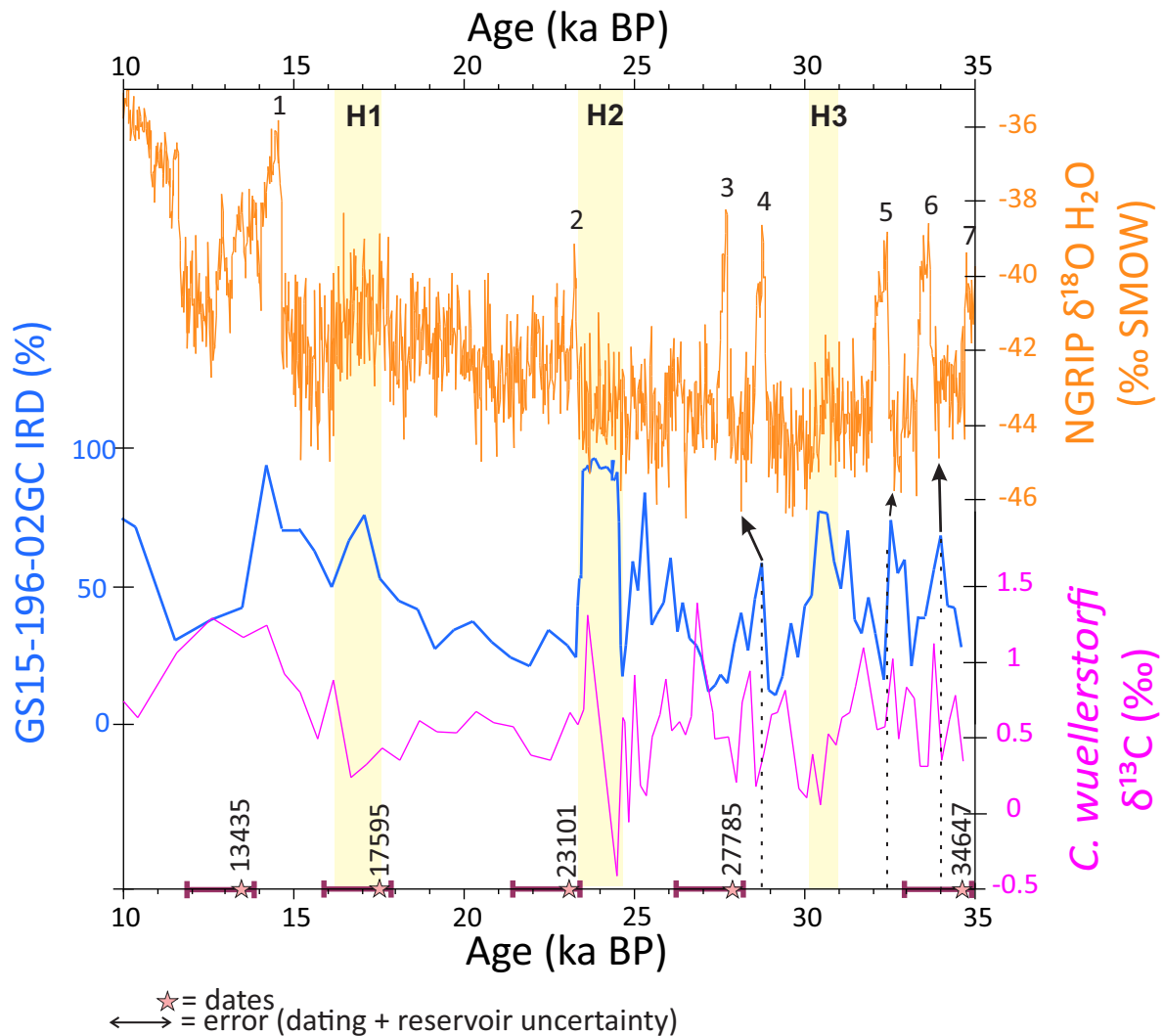


Figure 7.9: IRD (%) (blue) and *C. wuellerstorfi* $\delta^{13}\text{C}$ (VPDB ‰) (pink) from core GS15-196-02GC plotted against age (ka BP), stars denote dated ages, double-sided arrow the dating uncertainties (including the reservoir uncertainties during North Atlantic stadials (up to 2000 years) (see subchapter 5.2.1)). NGRIP (North Greenland Ice core project) (75.1°N, 42.32°W) $\delta^{18}\text{O}_{\text{ice}}$ (‰ SMOW) record (NGRIP members, 2004) in orange plotted against age (ka BP). Numbers (2-7) denote DO-warming events. Yellow shaded boxes note H1-H3 defined from core GS15-196-02GC. Arrows note the NGRIP cold events that may correspond to IRD peaks in GS15-196-02GC.

Taken together, the new multi-proxy record from GS15-196-02GC presented in this thesis add importantly to the ongoing debate regarding the coupling of deep water ventilation, ice rafting and freshwater fluxes. The new records clearly document that during the last glaciation, in the Irminger Sea, reduced deep water ventilation and increased iceberg deliverance occurred prior to large (likely LIS sourced) freshwater input (planktonic $\delta^{18}\text{O}$ decreases) to the subpolar gyre, consistent with a role for “precursor” IRD and AMOC changes in triggering H-events. In addition, this thesis builds on to previous studies linking abrupt millennial scale climate oscillations during D-O cycles with AMOC reductions (e.g. (Henry et al., 2016)), by providing preliminary evidence for increased iceberg deliverance as a potential forcing or feedback mechanism. If correct, these findings provide some of the first empirical evidence for a continual freshwater (IRD) modulation of AMOC over D-O cycles used by models to generate D-O climate variability (Menviel et al., 2014). However, delineating the ultimate triggering mechanism and synchronicity of these IRD events with AMOC response requires additional work; ideally with a nearby, but deeper core spanning the stronger D-O cycles occurring in MIS 3.

7.4 Summary of conclusions

- Major IRD events in the Irminger Basin occur approximately coevally with H-events. Sedimentological proxies indicate that these IRD events are derived from GIS/FIS/BIS and not LIS (Hudson Strait). The record indicates that circum-Nordic Seas ice sheets release IRD synchronous/or prior to LIS.
- The major IRD events in GS15-196-02GC, associated with Heinrich events, are closely coupled to low $\delta^{18}\text{O}$ anomalies corresponding to near-surface water freshening in the subpolar gyre.
- Initial increases in the IRD input to the Irminger Basin occurs prior to peak freshening, these IRD “precursors” are most likely derived from GIS/FIS/BIS. These events were not large enough to trigger LIS collapse and simply too small to produce an associated low $\delta^{18}\text{O}$ anomaly in the subpolar gyre; consistent with the LIS as the main source of freshwater to the region.
- Deep water ventilation reductions (*C. wuellerstorfi* $\delta^{13}\text{C}$) are related to increased presence of Southern Ocean water and reduced density and/or amount of deep water formation in the Nordic Seas. The greatest reductions in deep water ventilation occurs during climate cold periods (Heinrich events).

- Initial reductions in deep water ventilation, related to a weaker AMOC, occur prior to peak freshening and are closely coupled to increased delivery of non-LIS “precursor” IRD to the site. These results support AMOC as a potential trigger of H-events, and more generally, as a synchronizing influence on ice sheet melting/decay.
- There is preliminary evidence that D-O stadials, not just H-events, experienced increased iceberg calving and reduced AMOC, pointing towards a systematic coupling between ocean circulation and ice sheets during millennial scale climate changes.

Taken together, the proxy records from core GS15-196-02GC indicate a two-way coupling between ice sheets and deep water circulation. “Precursor” IRD increases and reduced deep water ventilation in the Irminger Basin prior to Heinrich related freshening support the hypothesis that reduced AMOC is important for triggering LIS melting/collapse (Marcott et al., 2011). Likewise, the lowest ventilation during Heinrich events suggests that LIS collapse acted as a feedback, further reducing AMOC as theorized and simulated in models (e.g. (Manabe and Stouffer, 1997; Stouffer et al., 2006)). The close coupling between deep water and IRD changes, both inferred to reflect input from circum-Nordic Seas sources, highlights the potential importance of the Nordic Seas region, (likely) due to it being a key location for deep water formation.

REFERENCES

- Alvarez-Solas, J. & Ramstein, G. 2011. On the triggering mechanism of Heinrich events. *PNAS*, 108, 1359-1360.
- Andrews, J. T. 1985. Grain-size characteristics of Quaternary sediments, Baffin Island region. *In: Andrews, J. T. (ed.) Quaternary environments: Eastern Canadian Arctic, Baffin Bay and western Greenland*. Boston: Allen and Unwin.
- Andrews, J. T. 2000. Icebergs and iceberg rafted detritus (IRD) in the North Atlantic; facts and assumptions. *Oceanography*, 13, 100-108.
- Armstrong, H. & Brasier, M. 2009. *Microfossils*, Hoboken, Wiley.
- Bacon, S., Reverdin, G., Rigor, I. G. & Snaith, H. M. 2002. A freshwater jet on the east Greenland shelf. *Journal of Geophysical Research*, 107.
- Bacon, S., Marshall, A., Holliday, N. P., Aksenov, Y. & Dye, S. R. 2014. Seasonal variability of the East Greenland Coastal Current. *Journal of Geophysical Research*, 119, 3967-3987.
- Bard, E., Arnold, M. & Duplessy, J.-C. 1991. Reconciling the sea level record of the last deglaciation with ^{18}O spectra from deep sea cores. *In: Lowe, J. J. (ed.) Radiocarbon dating: recent applications and future potential. Quaternary proceedings*. London: Quaternary Research Association.
- Bauch, D., Carstens, J. & Wefer, G. 1997. Oxygen isotope composition of living *Neogloboquadrina pachyderma* (sin.) in the Arctic Ocean. *Earth and Planetary Science Letters*, 146, 47-58.
- Bauch, D., Darling, K., Simstich, J., Bauch, H. A., Erlenkeuser, H. & Kroon, D. 2003. Palaeoceanographic implications of genetic variation in living North Atlantic *Neogloboquadrina pachyderma*. *Nature*, 424, 299-302.
- Bauch, H. A., Erlenkeuser, H., Spielhagen, R. F., Struck, U., Matthiessen, J., Thiede, J. & Heinemeier, J. 2001. A multiproxy reconstruction of the evolution of deep and surface waters in the subarctic Nordic seas over the last 30,000 yr. *Quaternary Science Reviews*, 20, 659-678.
- Beck, J. W., Richards, D. A., Edwards, R. L., Silverman, B. W., Smart, P. L., Donahue, D. J., Herrera-Osterheld, S., Burr, G. S., Calsoyas, L., Jull, A. J. T. & Biddulph, D. 2001. Extremely large variations of atmospheric ^{14}C concentration during the last glacial period. *Science*, 292, 2453-2458.
- Berger, W. H., Bé, A. W. H. & Vincent, E. 1981. Oxygen and carbon isotopes in foraminifera. *Palaeogeography, Palaeoclimatology, Palaeoecology*, 33.

- Berger, W. H. & Jansen, E. 1994. Fourier stratigraphy: Spectral gain adjustment of orbital ice mass models as an aid in dating Late Neogene deep-sea sediments. *Paleoceanography*, 9, 693-703.
- Bianchi, G. G. & Mccave, I. N. 1999. Holocene periodicity in North Atlantic climate and deep-ocean flow south of Iceland. *Nature*, 397, 515-517.
- Bigg, G. R. & Rohling, E. J. 2000. An oxygen isotope data set for marine waters. *Journal of Geophysical Research: Oceans*, 105, 8527-8535.
- Blaauw, M. & Christen, J. A. 2011. Flexible Paleoclimate Age-Depth Models Using an Autoregressive Gamma Process. *Bayesian Anal.*, 6, 457-474.
- Blaauw, M. & Christen, J. A. 2013. *Bacon Manual - v2.2* [Online]. Available: <http://www.chrono.qub.ac.uk/blaauw/bacon.html> [Accessed 27.02 2017].
- Bond, G. C., Heinrich, H., Broecker, W. S., Labeyrie, L., McManus, J. F., Andrews, J. T., Huon, S., Jantschik, R., Clasen, S., Simet, C., Tedesco, K., Mieczyslawa, K., Georges, B. & Susan, I. 1992. Evidence for massive discharges of icebergs into the North Atlantic ocean during the last glacial period. *Nature*, 360, 245-249.
- Bond, G. C., Broecker, W., B, Johnsen, S., McManus, J. F., Labeyrie, L., Jouzel, J. & Bonani, G. 1993. Correlations between climate records from North Atlantic sediments and Greenland ice. *Nature*, 365, 143-147.
- Bond, G. C. & Lotti, R. 1995. Iceberg discharges into the North Atlantic on millennial time scales during the last glaciation. *Science*, 267, 1005-1010.
- Boyle, E. A. & Keigwin, L. D. 1985. Comparison of Atlantic and Pacific paleochemical records for the last 215,000 years: changes in deep ocean circulation and chemical inventories. *Earth and Planetary Science Letters*, 76, 135-150.
- Boyle, E. A. 1992. Cadmium and $\delta^{13}\text{C}$ Paleochemical Ocean Distributions During the Stage 2 Glacial Maximum. *Annu. Rev. Earth Planet. Sci.* 20, 245-287.
- Broecker, W. S. 1991. The Great Ocean Conveyor. *Oceanography*, 4.
- Broecker, W. S., Bond, G. C., Klas, M., Clark, E. & Mcmanus, J. F. 1992. Origin of the northern Atlantic's Heinrich events. *Climate Dynamics*, 6, 265-273.
- Broecker, W. S. 1994. Massive iceberg discharges as triggers for global climate change. *Nature*, 372, 421-424.
- Broecker, W. S., Mcgee, D., Adams, K. D., Cheng, H., Edwards, R. L., Oviatt, C. G. & Quade, J. 2009. A Great Basin-wide dry episode during the first half of the Mystery Interval? *Quaternary Science Reviews*, 28, 2557-2563.
- Channell, J. E. T., Hodell, D. A. & Lehman, B. 1997. Relative geomagnetic paleointensity and $\delta^{18}\text{O}$ at ODP Site 983 (Gardar Drift, North Atlantic) since 350ka. *Earth and Planetary Science Letters*, 153, 103-118.

- Chapman, M. R. & Shackleton, N. J. 1998. Millennial-scale fluctuations in North Atlantic heat flux during the last 150,000 years. *Earth and Planetary Science Letters*, 159, 57-70.
- Chi, J. & Mienert, J. 1996. Linking physical property records of Quaternary sediments to Heinrich events. *Marine Geology*, 131, 57-73.
- Clark, I. D. & Fritz, P. 1997. *Environmental isotopes in hydrogeology*, Boca Raton, FL, Lewis Publishers.
- Clark, P. U., Marshall, S. J., Clarke, G. K. C., Hostetler, S. W., Licciardi, J. M. & Teller, J. T. 2001. Freshwater forcing of abrupt climate change during the last glaciation. *Science*, 293, 283-287.
- CLIMAP Members 1976. The subsurface of the Ice-Age Earth. *Science*, 191, 1131-1137.
- Cohen, K. M., Finney, S. C., Gibbard, P. L. & Fan, J.-X. 2013. The ICS International Chronostratigraphic Chart. *Episodes* 36, 119-204.
- Corliss, B. H. 1991. Morphology and microhabitat preferences of benthic foraminifera from the northwest Atlantic Ocean. *Marine Micropaleontology*, 17, 195-236.
- Cortijo, E., Labeyrie, L., Vidal, L., Vautravers, M., Chapman, M., Duplessy, J.-C., Elliot, M., Arnold, M., Turon, J.-L. & Auffret, G. 1997. Changes in sea surface hydrology associated with Heinrich event 4 in the North Atlantic Ocean between 40° and 60°N. *Earth and Planetary Science Letters*, 146, 29-45.
- Cronin, T. M. 2010. *Paleoclimates : understanding climate change past and present*, N.Y, Columbia University Press.
- Croudace, I. W., Rindby, A. & Rothwell, R. G. 2006. ITRAX; description and evaluation of a new multi-function X-ray core scanner. *Geological Society Special Publications*, 267, 51-63.
- Cuny, J., Rhines, P., Niiler, P. & Bacon, S. 2002. Labrador Sea Boundary Currents and the Fate of the Irminger Sea Water. *Journal of Physical Oceanography*, 32, 627-647.
- Curry, W. B., Duplessy, J.-C., Labeyrie, L. D. & Shackleton, N. J. 1988. Changes in the distribution of $\delta^{13}\text{C}$ of deep water ΣCO_2 between the Last Glaciation and the Holocene. *Paleoceanography*, 3, 317-341.
- Curry, W. B. & Oppo, D. W. 2005. Glacial water mass geometry and the distribution of $\delta^{13}\text{C}$ of ΣCO_2 in the western Atlantic Ocean. *Paleoceanography*, 20.
- Dansgaard, W. & Tauber, H. 1969. Glacier oxygen-18 content and Pleistocene ocean temperatures. *Science*, 166, 499-502.

- Dansgaard, W. & Oeschger, H. 1989. Past environmental long-term records from the Arctic. In: Oeschger, H. & Langway Jr, C. C. (eds.) *The Environmental Record in Glaciers and Ice Sheets*. Chichester, UK: John Wiley & Sons.
- Dansgaard, W., Johnsen, S. J., Clausen, H. B., Dahl-Jensen, D., Gundestrup, N. S., Hammer, C. U., Hvidberg, C. S., Steffensen, J. P., Sveinbjörnsdóttir, A. E., Jouzel, J. & Bond, G. C. 1993. Evidence for general instability of past climate from a 250-kyr ice-core record. *Nature*, 364, 218-220.
- Darby, D. A., Bischof, J. F., Spielhagen, R. F., Marshall, S. A. & Herman, S. W. 2002. Arctic ice export events and their potential impact on global climate during the late Pleistocene. *Paleoceanography*, 17.
- Darling, K. F., Kucera, M., Kroon, D. & Wade, C. M. 2006. A resolution for the coiling direction paradox in *Neogloboquadrina pachyderma*. *Paleoceanography*, 21.
- De Abreu, L., Shackleton, N. J., Schönfeld, J., Hall, M. A. & Chapman, M. R. 2003. Planktonic foraminifera, stable isotope record and temperature reconstruction of sediment core MD95-2040.
- De Vernal, A. & Hillaire-Marcel, C. 2000. Sea-ice cover, sea-surface salinity and halothermocline structure of the northwest North Atlantic: modern versus full glacial conditions. *Quaternary Science Reviews*, 19, 65-85.
- Dearing, J. 1994. Environmental Magnetic Susceptibility, Using the Bartington MS2 system. Kenilworth, England: Chi Publishing.
- Dickson, R. R. & Brown, J. 1994. The production of North Atlantic Deep Water: Sources, rates, and pathways. *Journal of Geophysical Research: Oceans*, 99, 12319-12341.
- Dunn, S. 2016. *Gas Source Mass Spectrometry: Stable Isotope Geochemistry* [Online]. Available: http://serc.carleton.edu/research_education/geochemsheets/techniques/gassourcemasspec.html [Accessed 20.03 2017].
- Duplessy, J.-C., Shackleton, N. J., Matthews, R. K., Prell, W., Ruddiman, W. F., Caralp, M. & Hendy, C. H. 1984. ¹³C Record of benthic foraminifera in the last interglacial ocean: Implications for the carbon cycle and the global deep water circulation. *Quaternary Research*, 21, 225-243.
- Duplessy, J.-C., Shackleton, N. J., Fairbanks, R. G., Labeyrie, L., Oppo, D. W. & Kallel, N. 1988. Deepwater source variations during the last climatic cycle and their impact on the global deepwater circulation. *Paleoceanography*, 3, 343-360.
- Dyke, L. 2016. *Cartography* [Online]. Available: <http://www.laurencedyke.com/cartography.html> [Accessed 05.05 2017].
- Eide, M., Olsen, A., Ninnemann, U. & Johannessen, T. 2017. A global ocean climatology of preindustrial and modern ocean $\delta^{13}\text{C}$. *Global Biogeochemical Cycles*, 31, 515-534.

- Elliot, M., Labeyrie, L., Bond, G., Cortijo, E., Turon, J. L., Tisnerat, N. & Duplessy, J.-C. 1998. Millennial-scale iceberg discharges in the Irminger Basin during the Last Glacial Period: Relationship with the Heinrich events and environmental settings. *Paleoceanography*, 13, 433-446.
- Emiliani, C. 1955. Pleistocene Temperatures. *The Journal of Geology*, 63, 538-578.
- Epstein, S., Buchsbaum, R., Lowenstam, H. A. & Urey, H. C. 1953. Revised carbonate-water isotopic temperature scale. *Geological Society of America Bulletin*, 64.
- Fairbanks, R. G. 1989. A 17,000-year glacio-eustatic sea level record: influence of glacial melting rates on the Younger Dryas event and deep-ocean circulation. *Nature*, 342, 637-647.
- Fer, I. 2012. *WEDDEL* [Online]. UiB/GFI. Available: <http://www.uib.no/node/57577> [Accessed 05.05 2017].
- Godwin, H. 1962. Half-life of Radiocarbon. *Nature*, 195, 984.
- Gooday, A. J. & Rathburn, A. E. 1999. Temporal variability in living deep-sea benthic foraminifera: a review. *Earth Science Reviews*, 46, 187-212.
- Grootes, P. M., Stuiver, M., White, J. W. C., Johnsen, S. & Jouzel, J. 1993. Comparison of oxygen isotope records from the GISP2 and GRIP Greenland ice cores. *Nature*, 366, 552-554.
- Grousset, F. E., Labeyrie, L., Sinko, J. A., Cremer, M., Bond, G., Duprat, J., Cortijo, E. & Huon, S. 1993. Patterns of ice-rafted detritus in the glacial North Atlantic (40°-55°N). *Paleoceanography*, 175-192.
- Grousset, F. E., Pujol, C., Labeyrie, L., Auffret, G. & Boelaert, A. 2000. Were the North Atlantic Heinrich events triggered by the behavior of the European ice sheets? *Geology*, 28, 123-126.
- Grousset, F. E., Cortijo, E., Huon, S., Hervé, L., Richter, T. O., Burdloff, D., Duprat, J. & Weber, O. 2001. Zooming in on Heinrich layers. *Paleoceanography*, 16, 240-259.
- Gunn, D. E. & Best, A. I. 1998. A new automated nondestructive system for high resolution multi-sensor core logging of open sediment cores. *Geo-Marine Letters*, 18, 70-77.
- Haine, T., Böning, C., Brandt, P., Fischer, J., Funk, A., Dagmar, K., Kvaleberg, E., Rhein, M. & Visbeck, M. 2008. North Atlantic Deep Water Formation in the Labrador Sea, Recirculation Through the Subpolar Gyre and Discharge to the Subtropics. In: Dickson, R. R., Meincke, J. & Rhines, P. (eds.) *Arctic-Subarctic Ocean Fluxes: Defining the Role of the Northern Seas in Climate*. Netherlands, Dordrecht: Springer.
- Hansen, B. & Østerhus, S. 2000. North Atlantic-Nordic Seas exchanges. *Progress in Oceanography*, 45, 109-208.

- Hays, J. D., Imbrie, J. & Shackleton, N. J. 1976. Variations in the earth's orbit: pacemaker of the ice ages. *Science*, 194, 1121-1132.
- Heinrich, H. 1988. Origin and consequences of cyclic ice rafting in the Northeast Atlantic Ocean during the past 130,000 years. *Quaternary Research*, 29, 142-152.
- Hemleben, C., Spindler, M. & Anderson, O. R. 1989. *Modern planktonic foraminifera*, New York, Springer.
- Hemming, S. R. 2004. Heinrich events: Massive late Pleistocene detritus layers of the North Atlantic and their global climate imprint. *Reviews of Geophysics*, 42.
- Henry, L. G., Mcmanus, J. F., Curry, W. B., Roberts, N. L., Piotrowski, A. M. & Keigwin, L. D. 2016. North Atlantic ocean circulation and abrupt climate change during the last glaciation. *Science*, 353.
- Hillaire-Marcel, C., De Vernal, A., Bilodeau, G. & Wu, G. 1994. Isotope stratigraphy, sedimentation rates, deep circulation and carbonate events in the Labrador Sea during the last 200 ka. *Canadian Journal of Earth Sciences*, 31, 63-89.
- Hillaire-Marcel, C. & Ravelo, A. C. 2007. The use of Oxygen and Carbon isotopes of Foraminifera in Paleoceanography. In: Hillaire-Marcel, C. & De Vernal, A. (eds.) *Developments in Marine Geology: Proxies in Late Cenozoic Paleoceanography*. Burlington: Elsevier Science.
- Hodell, D. A., Channell, J. E., Curtis, J. H., Romero, O. E. & Röhl, U. 2008a. North Atlantic IODP Site 303-U1308 Middle Pleistocene Heinrich Events record.
- Hodell, D. A., Channell, J. E. T., Curtis, J. H., Romero, O. E. & Röhl, U. 2008b. Onset of "Hudson Strait" Heinrich events in the eastern North Atlantic at the end of the middle Pleistocene transition (~640 ka)? *Paleoceanography*, 23.
- Holliday, N. P., Meyer, A., Bacon, S., Alderson, S. G. & De Cuevas, B. 2007. Retroflexion of part of the east Greenland current at Cape Farewell. *Geophysical Research Letters*, 34.
- Hughen, K., Lehman, S., Southon, J., Overpeck, J., Marchal, O., Herring, C. & Turnbull, J. 2004. ^{14}C activity and global carbon cycle changes over the past 50,000 years. *Science*, 303, 202-207.
- Hunter, S., Wilkinson, D., Louarn, E., Nick Mccave, I., Rohling, E., Stow, D. a. V. & Bacon, S. 2007. Deep western boundary current dynamics and associated sedimentation on the Eirik Drift, Southern Greenland Margin. *Deep-Sea Research Part I: Oceanographic Research Papers*, 54, 2036-2066.
- IAEA. 2009. *NBS18, Calcite* [Online]. Available: https://nucleus.iaea.org/rpst/referenceproducts/referencematerials/Stable_Isotopes/13C18and7Li/NBS_18.htm [Accessed 05.02 2017].

- Imbrie, J., Berger, A., Boyle, E. A., Clemens, S. C., Duffy, A., Howard, W. R., Kukla, G., Kutzbach, J., Martinson, D. G., McIntyre, A., Mix, A. C., Molfino, B., Morley, J. J., Peterson, L. C., Pisias, N. G., Prell, W. L., Raymo, M. E., Shackleton, N. J. & Toggweiler, J. R. 1993. On the structure and origin of major glaciation cycles 2. The 100,000-year cycle. *Paleoceanography*, 8, 699-735.
- IPCC 2013. Climate Change 2013: The Physical Science Basis. Contribution of Working Group I to the Fifth Assessment Report of the Intergovernmental Panel on Climate Change. *In*: Stocker, T. F., Qin, D., Plattner, G.-K., Tignor, M., Allen, S. K., Boschung, J., Nauels, A., Xia, Y., Bex, V. & Midgley, P. M. (eds.). Cambridge, United Kingdom and New York, NY, USA.
- Irvali, N., Ninnemann, U., Galaasen, E., Rosenthal, Y., Kroon, D., Oppo, D., Kleiven, H., Darling, K. & Kissel, C. 2012. Rapid switches in subpolar North Atlantic hydrography and climate during the Last Interglacial (MIS 5e). *Paleoceanography*, 27.
- Isachsen, P. E., Sørlie, S. R., Mauritzen, C., Lydersen, C., Dodd, P. & Kovacs, K. M. 2014. Upper-ocean hydrography of the Nordic Seas during the International Polar Year (2007–2008) as observed by instrumented seals and Argo floats. *Deep-Sea Research Part I*, 93, 41-59.
- Jakobsen, P. K., Ribergaard, M. H., Quadfasel, D., Schmith, T. & Hughes, C. W. 2003. Near-surface circulation in the northern North Atlantic as inferred from Lagrangian drifters: Variability from the mesoscale to interannual. *Journal of Geophysical Research*, 108.
- Jakobsson, M., Mayer, L., Coakley, B., Dowdeswell, J. A., Forbes, S., Fridman, B., Hodnesdal, H., Noormets, R., Pedersen, R., Rebesco, M., Schenke, H. W., Zarayskaya, Y., Accettella, D., Armstrong, A., Anderson, R. M., Bienhoff, P., Camerlenghi, A., Church, I., Edwards, M., Gardner, J. V., Hall, J. K., Hell, B., Hestvik, O., Kristoffersen, Y., Marcussen, C., Mohammad, R., Mosher, D., Nghiem, S. V., Pedrosa, M. T., Travaglini, P. G. & Weatherall, P. 2012. The International Bathymetric Chart of the Arctic Ocean (IBCAO) Version 3.0. *Geophysical Research Letters*, 39.
- Johannessen, T. 1992. *Stable Isotopes as Climate Indicators in Ocean and Lake sediments*. Dr. Scient, University of Bergen.
- Jonkers, L., Brummer, G. J. A., Peeters, F. J. C., Van Aken, H. M. & De Jong, M. F. 2010. Seasonal stratification, shell flux, and oxygen isotope dynamics of left-coiling *N. pachyderma* and *T. quinqueloba* in the western subpolar North Atlantic. *Paleoceanography*, 25.
- Jorissen, F. J. & Wittling, I. 1999. Ecological evidence from live–dead comparisons of benthic foraminiferal faunas off Cape Blanc (Northwest Africa). *Palaeogeography, Palaeoclimatology, Palaeoecology*, 149, 151-170.
- Kawasaki, T. & Hasumi, H. 2014. Effect of freshwater from the West Greenland Current on the winter deep convection in the Labrador Sea. *Ocean Modelling*, 75, 51-64.

- Keigwin, L. D. & Lehman, S. J. 1994. Deep circulation change linked to Heinrich Event 1 and Younger Dryas in a middepth North Atlantic Core. *Paleoceanography*, 9, 185-194.
- Kipp, N. G. 1976. New transfer function for estimating past sea-surface conditions from seabed distribution of planktonic foraminiferal assemblages in the North Atlantic. *Mem. Geol. Soc. Am.*, 145, 3-41.
- Kissel, C., Laj, C., Labeyrie, L., Dokken, T., Voelker, A. & Blamart, D. 1999. Rapid climatic variations during marine isotopic stage 3: magnetic analysis of sediments from Nordic Seas and North Atlantic. *Earth and Planetary Science Letters*, 171, 489-502.
- Kleiven, H. K. F., Kissel, C., Laj, C., Ninnemann, U. S., Richter, T. O. & Cortijo, E. 2008. Reduced North Atlantic deep water coeval with the glacial Lake Agassiz freshwater outburst. *Science*, 319, 60-64.
- Knutz, P. C., Zahn, R. & Hall, I. R. 2007. Centennial-scale variability of the British Ice Sheet: Implications for climate forcing and Atlantic meridional overturning circulation during the last deglaciation. *Paleoceanography*, 22.
- Kohfeld, K. E., Fairbanks, R. G., Smith, S. L. & Walsh, I. D. 1996. Neogloboquadrina pachyderma (sinistral coiling) as paleoceanographic tracers in polar oceans; evidence from Northeast Water Polynya plankton tows, sediment traps, and surface sediments. *Paleoceanography*, 11, 679-699.
- Krauss, W. 1995. Currents and mixing in the Irminger Sea and in the Iceland Basin. *Journal of Geophysical Research: Oceans*, 100, 10851-10871.
- Kretschmer, K., Kucera, M. & Schulz, M. 2016. Modeling the distribution and seasonality of Neogloboquadrina pachyderma in the North Atlantic Ocean during Heinrich Stadial 1. *Paleoceanography*, 31, 986-1010.
- Kroopnick, P. M. 1985. The distribution of ^{13}C of ΣCO_2 in the world oceans. *Deep Sea Research Part A, Oceanographic Research Papers*, 32, 57-84.
- Kuhlbrodt, T., Griesel, A., Montoya, M., Levermann, A., Hofmann, M. & Rahmstorf, S. 2007. On the driving processes of the Atlantic meridional overturning circulation. *Reviews of Geophysics*, 45.
- Kuijpers, A., Troelstra, S. R., Prins, M. A., Linthout, K., Akhmetzhanov, A., Bouryak, S., Bachmann, M. F., Lassen, S., Rasmussen, S. & Jensen, J. B. 2003. Late Quaternary sedimentary processes and ocean circulation changes at the Southeast Greenland margin. *Marine Geology*, 195, 109-129.
- Labeyrie, L. D. & Duplessy, J.-C. 1985. Changes in the oceanic $^{13}\text{C}/^{12}\text{C}$ ratio during the last 140 000 years: High-latitude surface water records. *Palaeogeography, Palaeoclimatology, Palaeoecology*, 50, 217-240.

- Labeyrie, L. D., Duplessy, J.-C., Duprat, J., Juillet-Leclerc, A., Moyes, J., Michel, E., Kallel, N. & Shackleton, N. J. 1992. Changes in the vertical structure of the North Atlantic Ocean between glacial and modern times. *Quaternary Science Reviews*, 11, 401-413.
- Lambeck, K., Rouby, H., Purcell, A., Sun, Y. & Sambridge, M. 2014. Sea level and global ice volumes from the Last Glacial Maximum to the Holocene. *PNAS*, 111, 15296-15303.
- Lekens, W. A. H., Sejrup, H. P., Haflidason, H., Knies, J. & Richter, T. 2006. Meltwater and ice rafting in the southern Norwegian Sea between 20 and 40 calendar kyr B.P.: Implications for Fennoscandian Heinrich events. *Paleoceanography*, 21.
- Levermann, A., Griesel, A., Hofmann, M., Montoya, M. & Rahmstorf, S. 2005. Dynamic sea level changes following changes in the thermohaline circulation. *Climate Dynamics*, 24, 347-354.
- Linke, P. & Lutze, G. F. 1993. Microhabitat preferences of benthic foraminifera—a static concept or a dynamic adaptation to optimize food acquisition? *Marine Micropaleontology*, 20, 215-234.
- Lisiecki, L. E. & Raymo, M. E. 2005. A Pliocene-Pleistocene stack of 57 globally distributed benthic $\delta^{18}\text{O}$ records. *Paleoceanography*, 20.
- Lutze, G. F. & Thiel, H. 1989. Epibenthic foraminifera from elevated microhabitats; *Cibicidoides wuellerstorfi* and *Planulina ariminensis*. *Journal of Foraminiferal Research*, 19, 153-158.
- Lynch-Stieglitz, J., Adkins, J., Curry, W., Dokken, T., Hall, I. R., Herguera, J., Hirschi, J., Ivanova, E., Kissel, C., Marchal, O., Marchitto, T. M., Mccave, I., Mcmanus, J., Mulitza, S., Ninnemann, U., Peeters, F., Yu, E. & Zahn, R. 2007. Atlantic meridional overturning circulation during the Last Glacial Maximum. *Science*, 316, 66-69.
- Macayeal, D. R. 1993. Binge/purge oscillations of the Laurentide ice sheet as a cause of the North Atlantic's Heinrich events. *Paleoceanography*, 8, 775-784.
- Mackensen, A., Hubberten, H.-W., Bickert, T., Fisher, G. & Fütterer, D. K. 1993. The $\delta^{13}\text{C}$ in benthic foraminiferal tests of *Fontbotia wuellerstorfi* (Schwager) Relative to the $\delta^{13}\text{C}$ of dissolved inorganic carbon in Southern Ocean Deep Water: Implications for glacial ocean circulation models. *Paleoceanography*, 8, 587-610.
- Manabe, S. & Stouffer, R. J. 1995. Simulation of abrupt climate change induced by freshwater input to the North Atlantic Ocean. *Nature*, 378, 165-167.
- Manabe, S. & Stouffer, R. J. 1997. Coupled ocean-atmosphere model response to freshwater input: Comparison to Younger Dryas Event. *Paleoceanography*, 12, 321-336.
- Marcott, S. A., Clark, P. U., Padman, L., Klinkhammer, G. P., Springer, S. R., Liu, Z., Otto-Bliesner, B. L., Carlson, A. E., Ungerer, A., Padman, J., He, F., Cheng, J. & Schmittner, A. 2011. Ice-shelf collapse from subsurface warming as a trigger for Heinrich events. *PNAS*, 108.

- Maslin, M. A., Shackleton, N. J. & Pflaumann, U. 1995. Surface water temperature, salinity, and density changes in the northeast Atlantic during the last 45,000 years: Heinrich events, deep water formation, and climatic rebounds. *Paleoceanography*, 10, 527-544.
- Mauritzen, C. 1996. Production of dense overflow waters feeding the North Atlantic across the Greenland-Scotland Ridge. Part 1: Evidence for a revised circulation scheme. *Deep-Sea Research Part I: Oceanographic Research Papers*, 43, 769-806.
- McCartney, M. S. 1992. Recirculating components to the deep boundary current of the northern North Atlantic. *Progress in Oceanography*, 29, 283-383.
- McCorkle, D. C. & Keigwin, L. 1994. Depth profiles of δ C-13 in bottom water and core top *C. Wuellerstorfi* on the Ontong Java Plateau and Emperor Seamounts. *Paleoceanography*, 9, 197-208.
- McCorkle, D. C., Corliss, B. H. & Farnham, C. A. 1997. Vertical distributions and stable isotopic compositions of live (stained) benthic foraminifera from the North Carolina and California continental margins. *Deep-Sea Research Part I*, 44, 983-1024.
- McCrea, J. M. 1950. On the Isotopic Chemistry of Carbonates and a Paleotemperature Scale. *The Journal of Chemical Physics*, 18, 849-857.
- McManus, J. F., Bond, G. C., Broecker, W. S., Johnsen, S., Labeyrie, L. & Higgins, S. 1994. High-resolution climate records from the North Atlantic during the last interglacial. *Nature*, 371, 326-329.
- McManus, J. F., Francois, R., Gherardi, J. M., Keigwin, L. D. & Brown-Leger, S. 2004. Collapse and rapid resumption of Atlantic meridional circulation linked to deglacial climate changes. *Nature*, 428, 834-837.
- Meese, D. A., Gow, A. J., Alley, R. B., Zielinski, G. A., Grootes, P. M., Ram, M., Taylor, K. C., Mayewski, P. A. & Bolzan, J. F. 1997. The Greenland Ice Sheet Project 2 depth-age scale: Methods and results. *Journal of Geophysical Research: Oceans*, 102, 26411-26423.
- Menviel, L., Timmermann, A., Friedrich, T. & England, M. H. 2014. Hindcasting the continuum of Dansgaard-Oeschger variability: mechanisms, patterns and timing. *Climate of the Past*, 10, 63-77.
- Mignot, J., Ganopolski, A. & Levermann, A. 2007. Atlantic subsurface temperatures: Response to a shutdown of the overturning circulation and consequences for its recovery. *Journal of Climate*, 20, 4884-4898.
- Mix, A. C., Bard, E. & Schneider, R. 2001. Environmental processes of the ice age: land, oceans, glaciers (EPILOG). *Quaternary Science Reviews*, 20, 627-657.
- Morrill, C., Ward, E. M., Wagner, A. J., Otto-Bliesner, B. L. & Rosenbloom, N. 2014. Large sensitivity to freshwater forcing location in 8.2 ka simulations. *Paleoceanography*, 29, 930-945.

- Munsell, A. H. 1976. *Munsell book of color: glossy finish collection (2.5R-10G)*, Maryland, Munsell Color.
- Müller-Michaelis, A. & Uenzelmann-Neben, G. 2014. Development of the Western Boundary Undercurrent at Eirik Drift related to changing climate since the early Miocene. *Deep-Sea Research Part I: Oceanographic Research Papers*, 93, 21-34.
- National Academies of Sciences Engineering and Medicine 2015. A Strategic Vision for NSF Investments in Antarctic and Southern Ocean Research. Washington, DC: The National Academies Press.
- NGRIP Members 2004. High-resolution record of Northern Hemisphere climate extending into the last interglacial period. *Nature*, 431, 147-151.
- Naafs, B. D. A., Hefter, J. & Stein, R. 2013. Millennial-scale ice rafting events and Hudson Strait Heinrich(-like) Events during the late Pliocene and Pleistocene: a review. *Quaternary Science Reviews*, 80, 1-28.
- O'neil, J. R., Clayton, R. N. & Mayeda, T. K. 1969. Oxygen Isotope Fractionation in Divalent Metal Carbonates. *The Journal of Chemical Physics*, 51, 5547-5558.
- Olsen, A. & Ninnemann, U. 2010. Large delta ¹³C gradients in the preindustrial North Atlantic revealed. *Science*, 330, 658-659.
- Oppo, D. W. & Lehman, S. J. 1993. Mid-depth circulation of the subpolar North Atlantic during the last glacial maximum. *Science*, 259, 1148-1152.
- Oppo, D. W. & Lehman, S. J. 1995. Suborbital timescale variability of North Atlantic Deep Water during the past 200,000 years. *Palaeoceanography*, 10, 901-910.
- Orvik, K. A. & Niiler, P. 2002. Major pathways of Atlantic water in the northern North Atlantic and Nordic Seas toward Arctic. *Geophysical Research Letters*, 29.
- Pflaumann, U., Duprat, J., Pujol, C. & Labeyrie, L. D. 1996. SIMMAX: A modern analog technique to deduce Atlantic sea surface temperatures from planktonic foraminifera in deep-sea sediments. *Paleoceanography*, 11, 15-36.
- Pickart, R. S., Straneo, F. & Moore, G. W. K. 2003. Is Labrador Sea Water formed in the Irminger basin? *Deep-Sea Research Part I*, 50, 23-52.
- Pinet, P. R. 2013. *Invitation to oceanography*, Burlington, Mass, Jones & Bartlett Learning.
- Poulain, P. M., Warn-Varnas, A., Niiler, P. & Poulain, P. M. 1996. Near-surface circulation of the Nordic seas as measured by Lagrangian drifters. *Journal of Geophysical Research*, 101, 18237-18258.
- Rahmstorf, S. 1995. Bifurcations of the Atlantic thermohaline circulation in response to changes in the hydrological cycle. *Nature*, 378, 145-149.

- Rahmstorf, S. 2002. Ocean circulation and climate during the past 120,000 years. *Nature*, 419, 207-214.
- Rahmstorf, S. 2006. Thermohaline Ocean Circulation. *Encyclopedia of Quaternary Sciences*, Amsterdam.
- Rasmussen, T. L., Thomsen, E., Labeyrie, L. & Van Weering, T. C. E. 1996. Circulation changes in the Faeroe-Shetland Channel correlating with cold events during the last glacial period (58-10 ka). *Geology* 24, 937-940.
- Rasmussen, T. L., Oppo, D. W., Thomsen, E. & Lehman, S. J. 2003. Deep sea records from the southeast Labrador Sea: Ocean circulation changes and ice-rafting events during the last 160,000 years. *Paleoceanography*, 18.
- Ravelo, A. C. & Fairbanks, R. G. 1992. Oxygen Isotopic Composition of Multiple Species of Planktonic Foraminifera: Recorders of the Modern Photic Zone Temperature Gradient. *Paleoceanography*, 7, 815-831.
- Ravelo, A. C. & Fairbanks, R. G. 1995. Carbon isotopic fractionation in multiple species of planktonic foraminifera from core-tops in the tropical Atlantic. *The Journal of Foraminiferal Research*, 25, 53-74.
- Raymo, M. E. 1992. Global climate change: a three million year perspective. In: Kukla, G. & Went, W. (eds.) *Start of a glacial*. Berlin: Springer-Verlag.
- Reimer, P. J., Bard, E., Bayliss, A., Beck, J. W., Blackwell, P. G., Ramsey, C. B., Buck, C. E., Cheng, H., Edwards, R. L., Friedrich, M., Grootes, P. M., Guilderson, T. P., Hafliðason, H., Hajdas, I., Hatté, C., Heaton, T. J., Hoffmann, D. L., Hogg, A. G., Hughen, K. A., Kaiser, K. F., Kromer, B., Manning, S. W., Niu, M., Reimer, R. W., Richards, D. A., Scott, E. M., Southon, J. R., Staff, R. A., Turney, C. S. M. & Van Der Plicht, J. 2013. IntCal13 and Marine13 Radiocarbon Age Calibration Curves 0–50,000 Years cal BP. *Radiocarbon*, 55, 1869-1887.
- Rhein, M., Rintoul, S. R., Aoki, S., Campos, E., Chambers, D., Feely, R. A., Gulev, S., Johnson, G. C., Josey, S. A., Kostianoy, A., Mauritzen, C., Roemmich, D., Talley, L. D. & Wang, F. 2013. Observations: Ocean. In: Stocker, T. F., Qin, D., Plattner, G.-K., Tignor, M., Allen, S. K., Boschung, J., Nauels, A., Xia, Y., Bex, V. & Midgley, P. M. (eds.) *Climate Change 2013: The Physical Science Basis. Contribution of Working Group I to the Fifth Assessment Report of the Intergovernmental Panel on Climate Change*. Cambridge University Press, Cambridge, United Kingdom and New York, NY, USA.
- Rohling, E. J. & Cooke, S. 1999. Stable oxygen and carbon isotopes in foraminiferal carbonate shells. In: Sen Gupta, B. K. (ed.) *Modern foraminifera*. Dordrecht: Kluwer.
- Rignot, E., Velicogna, I., van Den Broeke, M. R., Monaghan, A. & Lenaerts, J. T. M. 2011. Acceleration of the contribution of the Greenland and Antarctic ice. *Geophysical Research Letters*, 38.

- Rosby, T. 1996. The North Atlantic Current and surrounding waters: At the crossroads. *Reviews of Geophysics*, 34, 463-481.
- Rothwell, R. G. & Croudace, I. W. 2015. Twenty Years of XRF Core Scanning Marine Sediments: What do Geochemical Proxies Tell Us? In: Croudace, I. W. & Rothwell, R. G. (eds.) *Micro-XRF Studies of Sediment Cores : Applications of a non-destructive tool for the environmental sciences*. Springer.
- Ruddiman, W. F. 1977. Late Quaternary deposition of ice-rafted sand in the subpolar North Atlantic (lat 40 degrees to 65 degrees N). *Geological Society of America Bulletin*, 88, 1813-1827.
- Ruddiman, W. F. 2014. *Earth's climate: past and future*, New York, W.H. Freeman.
- Rudels, B., Eriksson, P., Grönvall, H., Hietala, R. & Launiainen, J. 1999. Hydrographic observations in Denmark Strait in fall 1997, and their implications for the entrainment into the overflow plume. *Geophysical Research Letters*, 26, 1325-1328.
- Rudels, B., Fahrbach, E., Meincke, J., Budéus, G. & Eriksson, P. 2002. The East Greenland Current and its contribution to the Denmark Strait overflow. *ICES Journal of Marine Science*, 59, 1133-1154.
- Rudels, B., Eriksson, P., Buch, E., Budéus, G., Fahrbach, E., Malmberg, S. A., Meincke, J. & Mälkki, P. 2003. Temporal switching between sources of the Denmark Strait overflow water. *ICES Marine Science Symposia*, 219, 319-325.
- Ryan, W. B. F., Carbotte, S. M., Coplan, J. O., O' Hara, S., Melkonian, A., Arko, R., Weissel, R. A., Ferrini, V., Goodwillie, A., Nitsche, F., Bonczkowski, J. & Zemsky, R. 2009. Global Multi-Resolution Topography synthesis. *Geochemistry, Geophysics, Geosystems*, 10.
- Sachs, J. P. & Lehman, S. J. 1999. Subtropical North Atlantic temperatures 60,000 to 30,000 years ago. *Science*, 286, 756-759.
- Sarnthein, M., Winn, K., Jung, S. J. A., Duplessy, J.-C., Labeyrie, L., Erlenkeuser, H. & Ganssen, G. 1994. Changes in East Atlantic Deepwater Circulation over the last 30,000 years: Eight time slice reconstructions. *Paleoceanography*, 9, 209-267.
- Schiebel, R. & Hemleben, C. 2005. Modern planktic foraminifera. *Paläontologische Zeitschrift*, 79, 135-148.
- Schmidt, G. A. 1999. Forward modeling of carbonate proxy data from planktonic foraminifera using oxygen isotope tracers in a global ocean model. *Paleoceanography*, 14, 482-497.
- Schmidt, G. A., Bigg, G. R. & Rohling, E. J. 1999. *Global Seawater Oxygen-18 Database – v1.21* [Online]. Available: <http://data.giss.nasa.gov/o18data/> [Accessed 02.02 2017].

- Schmiedl, G. & Mackensen, A. 1997. Late Quaternary paleoproductivity and deep water circulation in the eastern South Atlantic Ocean: Evidence from benthic foraminifera. *Palaeogeography, Palaeoclimatology, Palaeoecology*, 130, 43-80.
- Schmittner, A. 2005. Decline of the marine ecosystem caused by a reduction in the Atlantic overturning circulation. *Nature*, 434, 628-633.
- Schrama, E. J. O. & Wouters, B. 2011. Revisiting Greenland ice sheet mass loss observed by GRACE. *Journal of Geophysical Research*, 116.
- Sen Gupta, B. K. 1999. Introduction to modern Foraminifera. In: Sen Gupta, B. K. (ed.) *Modern foraminifera*. Dordrecht: Kluwer.
- Shackleton, N. J. & Opdyke, N. D. 1973. Oxygen isotope and palaeomagnetic stratigraphy of Equatorial Pacific core V28-238: Oxygen isotope temperatures and ice volumes on a 10^5 year and 10^6 year scale. *Quaternary Research*, 3, 39-55.
- Shackleton, N. J. 1974. Attainment of isotopic equilibrium between ocean water and the benthonic foraminifera genus *Uvigerina*: isotopic changes in the ocean during the last glacial. *Cent. Nat. Rech., Sci. Colloq. Int.*, 219, 203-209.
- Shackleton, N. J. 1977. ^{13}C in *Uvigerina*: Tropical rain forest history and the equatorial Pacific carbonate dissolution cycle. In: Andersen, N. R. & Malahoff, A. (eds.) *The Fate of Fossil Fuel in the Oceans*. New York: Plenum.
- Simstich, J., Sarnthein, M. & Erlenkeuser, H. 2003. Paired $\delta^{18}\text{O}$ signals of *Neogloboquadrina pachyderma* (s) and *Turborotalita quinqueloba* show thermal stratification structure in Nordic Seas. *Marine Micropaleontology*, 48, 107-125.
- Smethie, W. M., Jr., Fine, R. A., Putzka, A. & Jones, E. P. 2000. Tracing the flow of North Atlantic Deep Water using chlorofluorocarbons. *Journal of Geophysical Research*, 105, 14297-14323.
- Smith, W. H. F. & Sandwell, D. T. 1997. Global sea floor topography from satellite altimetry and ship depth soundings. *Science*, 277, 1956-1962.
- Stanford, J. D., Rohling, E. J., Bacon, S. & Holliday, N. P. 2011. A review of the deep and surface currents around Eirik Drift, south of Greenland: Comparison of the past with the present. *Global and Planetary Change*, 79, 244-254.
- Stouffer, R., Yin, J., Gregory, J. & Dixon, K. 2006. Investigating the Causes of the Response of the Thermohaline Circulation to Past and Future Climate Changes. *Journal of Climate*, 19, 1365-1387.
- Stow, D. A. V., Faugeres, J.-C., Howe, J. A., Pudsey, C. J., Viana, A. R., Stow, D. a. V., Pudsey, C. J., Howe, J. A., Faugeres, J.-C. & Viana, A. R. 2002. Bottom currents, contourites and deep-sea sediment drifts; current state-of-the-art. *Memoirs of the Geological Society of London*, 22, 7-20.

- Straneo, F., Sutherland, D. A., Holland, D., Gladish, C., Hamilton, G. S., Johnson, H. L., Rignot, E., Xu, Y. & Koppes, M. 2012. Characteristics of ocean waters reaching Greenland's glaciers. *Annals of Glaciology*, 53, 202-210.
- Talley, L. & McCartney, L. 1982. Distribution and circulation of Labrador Sea Water. *Journal of Physical Oceanography*, 12, 1189-1205.
- Tanhua, T., Olsson, A. K. & Jeansson, E. 2008. Tracer Evidence of the Origin and Variability of Denmark Strait Overflow Water. In: Dickson, R. R., Meincke, J. & Rhines, P. (eds.) *Arctic-Subarctic ocean fluxes : defining the role of the Northern Seas in climate*. Dordrecht: Springer.
- Thornalley, D. J. R., Elderfield, H. & Mccave, I. N. 2010. Intermediate and deep water paleoceanography of the northern North Atlantic over the past 21,000 years. *Paleoceanography*, 25.
- Thornalley, D. J. R., Mccave, I. N. & Elderfield, H. 2011. Tephra in deglacial ocean sediments south of Iceland; stratigraphy, geochemistry and oceanic reservoir ages. *Journal of Quaternary Science*, 26, 190-198.
- Timmermann, A., An, S., Krebs, U. & Goosse, H. 2005. ENSO suppression due to weakening of the North Atlantic thermohaline circulation. *Journal of Climate*, 18, 3122-3139.
- Urey, H. C. 1947. The thermodynamic properties of isotopic substances. *Journal of the Chemical Society*, 562-581.
- Urey, H. C., Lowenstam, H., Epstein, S., & Mckinney, C. 1951. Measurement of Paleotemperatures and temperatures of the upper Cretaceous of England, Denmark, and the southeastern United States. *Bulletin of the Geological Society of America*, 62, 399-416.
- van Kreveld, S. A., Sarnthein, M., Erlenkeuser, H., Grootes, P. M., Jung, S., Nadeau, M. J., Pflaumann, U. & Voelker, A. 2000a. Potential links between surging ice sheets, circulation changes, and the Dansgaard-Oeschger Cycles in the Irminger Sea, 60–18 Kyr. *Paleoceanography*, 15, 425-442.
- van Kreveld, S. A., Sarnthein, M., Erlenkeuser, H., Grootes, P. M., Jung, S. J. A., Pflaumann, U. & Voelker, A. H. L. 2000b. Foraminifera, sedimentological parameters and sea surface temperature and salinity calculated on core SO82_5-2.
- Vellinga, M. & Wood, R. 2002. Global Climatic Impacts of a Collapse of the Atlantic Thermohaline Circulation. *Climatic Change*, 54, 251-267.
- Waelbroeck, C., Duplessy, J. C., Michel, E., Labeyrie, L., Paillard, D. & Duprat, J. 2001. The timing of the last deglaciation in North Atlantic climate records. *Nature*, 412, 724-727.
- Walker, M. J. C. 2005. Radiometric dating 1: Radiocarbon dating. In: Walker, M. J. C. (ed.) *Quaternary dating methods*. Chichester: John Wiley.

- Wang, X., Auler, A. S., Edwards, R. L., Cheng, H., Ito, E. & Solheid, M. 2006. Interhemispheric anti-phasing of rainfall during the last glacial period. *Quaternary Science Reviews*, 25, 3391-3403.
- Weinelt, M. 2004. Paleoproductivity of sediment core GIK23415-9.
- Wold, C. N. 1994. Cenozoic sediment accumulation on drifts in the northern North Atlantic. *Paleoceanography*, 9, 917-941.
- Yashayaev, I., Holliday, N. P., Bersch, M. & Van Aken, H. M. 2008. The history of the Labrador Sea Water: Production, Spreading, Transformation and Loss. *In*: Dickson, R. R., Meincke, J. & Rhines, P. (eds.) *Arctic-Subarctic Ocean Fluxes : Defining the Role of Northern Seas in Climate*. Netherlands, Dordrecht: Springer.
- Zeebe, R. E. 1999. An explanation of the effect of seawater carbonate concentration on foraminiferal oxygen isotopes. *Geochimica et Cosmochimica Acta*, 63, 2001-2007.

APPENDIX

Appendix A: **Statistics**

Appendix B: **AMS ^{14}C dates**

Table A.1: AMS ^{14}C dates received from ETH, Zûrich December 2016

Appendix A: Statistics

The standard deviations from the mean (STD) have been calculated for the complete dataset using Equation A.1.

$$STD = \sqrt{\frac{\sum(\bar{x}-x)^2}{n-k}} \quad \text{Equation A.1}$$

STD = standard deviation

\bar{x} = mean value of all replicates

x = value of single measurement

n = number of replicates

k = number of depth intervals with replicates

Standard error of the mean was calculated for each interval with replicates using Equation A.2

$$SEM = \frac{STD}{\sqrt{n}} \quad \text{Equation A.2}$$

N. pachyderma (s)

STD: n=52, k=26

SEM: n=2

Duplicate measurements of *N. pachyderma* (s) were carried out at approximately every third sample depth interval. The distribution of deviation from the mean for replicates show a normal and expected distribution (Figure A.1). For $\delta^{18}\text{O}$ a pooled standard deviation for all replicates of $\pm 0.076\text{‰}$ was calculated. This is slightly lower than the precision of the mass spectrometer ($\pm 0.08\text{‰}$), indicating reproducible and reliable results. Standard error of the mean for intervals with two replicates is $\pm 0.05\text{‰}$.

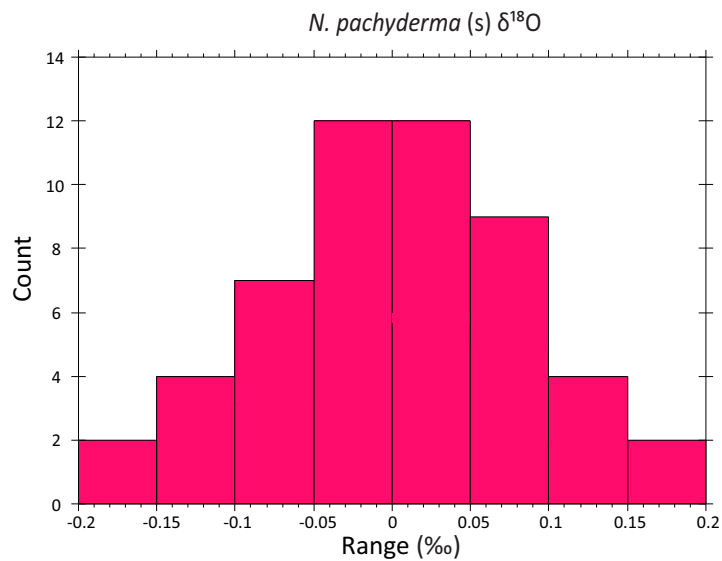


Figure A.1: Deviations from the mean of replicate *N. pachyderma (s)* stable oxygen isotope analysis. The number of deviations (count, y-axis) in per mil (range, x-axis)

For $\delta^{13}\text{C}$ the distribution of deviation from the mean for replicates show a normal and expected distribution (Figure A2). An average standard deviation for all replicates of $\pm 0.056\text{‰}$ was calculated. This is slightly higher than the precision of the mass spectrometer ($\pm 0.03\text{‰}$), but

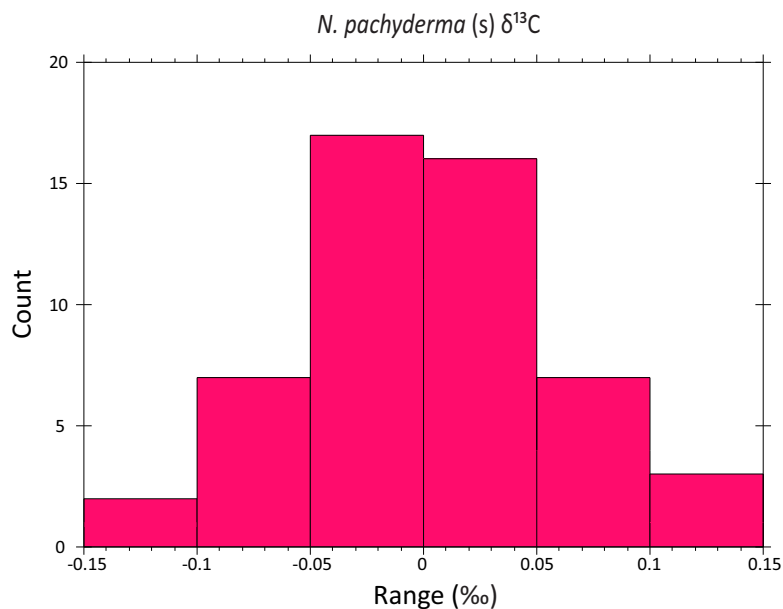


Figure A.2: Deviation from the mean of replicate *N. pachyderma (s)* stable carbon isotope analysis. The number of deviations (count, y-axis) in per mil (range, x-axis)

still indicating reproducible and reliable results. Standard error of the mean for intervals with two replicates is $\pm 0.04\text{‰}$.

C. wuellerstorfi

STD: n=46, k=23

SEM: n=2

Duplicate measurements of *C. wuellerstorfi* were carried out when possible and for $\delta^{18}\text{O}$ a pooled standard deviation from the mean of $\pm 0.08\text{‰}$ was calculated. This value is the same as the precision of the mass spectrometer ($\pm 0.08\text{‰}$), indicating that the samples reproduce well and give reliable results. Standard error of the mean for intervals with two replicates is $\pm 0.06\text{‰}$. The distribution of deviation from the mean for replicates show a normal and expected distribution (Figure A.3)

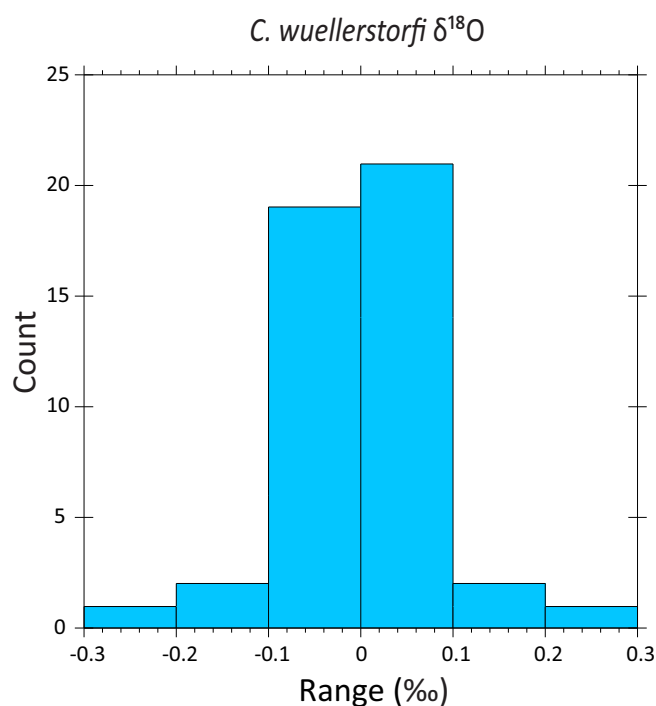


Figure A.3: Deviation from the mean of replicate *C. wuellerstorfi* stable oxygen isotope analysis. The number of deviations (count, y-axis) in per mil (range, x-axis)

For $\delta^{13}\text{C}$ (*C. wuellerstorfi*) a pooled standard deviation from the mean of $\pm 0.12\text{‰}$ was calculated. This value is higher than the precision of the mass spectrometer ($\pm 0.03\text{‰}$), but still indicating that the samples reproduce well and give reliable results. Standard error of the mean

for intervals with two replicates is $\pm 0.08\%$. The distribution of deviation from the mean for replicates show a normal and expected distribution (Figure A.4)

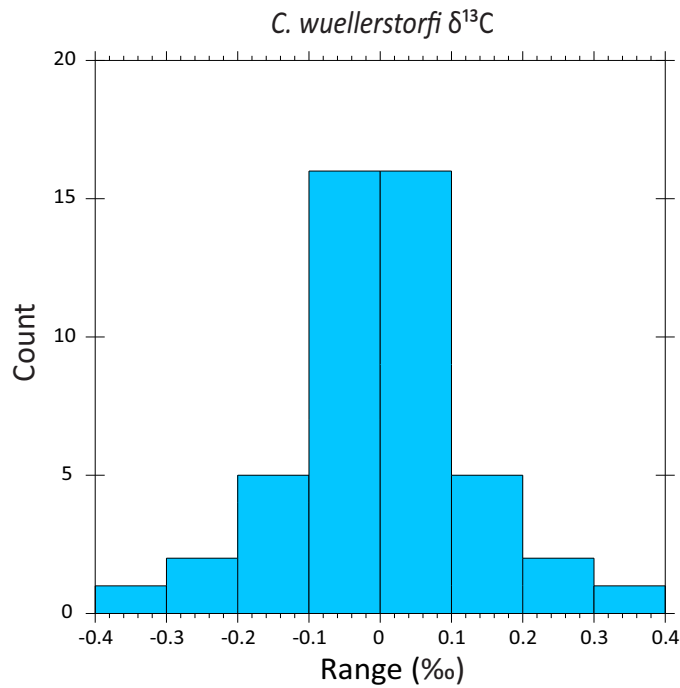


Figure A.4: Deviations from the mean of replicate *C. wuellerstorfi* stable carbon isotope analysis. The number of deviations (count, y-axis) in per mil (range, x-axis).

Ice Rafted Debris

STD: $n=14$, $k=7$

SEM: $n=2$

For IRD (%) an average standard deviation for all replicates of $\pm 2.52\%$ was calculated. Standard error of the mean for intervals with two replicates is $\pm 1.78\%$

Appendix B: AMS ¹⁴C dates

AMS ¹⁴C dating of samples from core GS15-196-02GC presented as received from the ETH Zürich laboratory, Switzerland.

Table B1: AMS ¹⁴C dates received from ETH, Zürich December 2016.

Sample ID	C14 age BP	±1σ	Depth	Reservoir correction	δ ¹³ C (‰)	±1σ	mg C
ETH-73712	6110	27	0	129+/-74	1,5	1	0.5
ETH-73713	6969	28	4	129+/-74	1,1	1	0.49
ETH-73714	12217	36	28	129+/-74	1,2	1	0.56
ETH-73715	14957	43	60	129+/-74	-0,9	1	0.51
ETH-73716	19788	63	100	129+/-74	-2,1	1	0.45
ETH-73717	24293	92	204	129+/-74	0,2	1	0.5
ETH-73718	30768	181	332	129+/-74	2,5	1	0.54

The reservoir correction factor was calculated (by ETH, Zürich) using the following values:

MapNo	Lat	Lon	ΔR	σ
670	63.2700	-41.1200	158	51
669	65.6500	-36.8800	168	69
34	64.2000	-51.7500	129	84
35	69.2200	-51.1300	-32	99
667	68.3500	-28.7300	27	51
671	68.4200	-28.5200	60	45
987	69.0000	-52.0000	260	40
990	69.0000	-52.0000	140	25
665	69.5000	-52.0000	75	51
37	69.6800	-52.0000	79	84

npts: 10

Weighted Mean ΔR= 129

Standard Deviation (square root of variance)= 74

[Explanation of calculation](#)

Figure B.1: Location of cores and their delta R values, used for calculating the average delta R, later used when calibrating the dates. Calculations done by ETH Zürich.

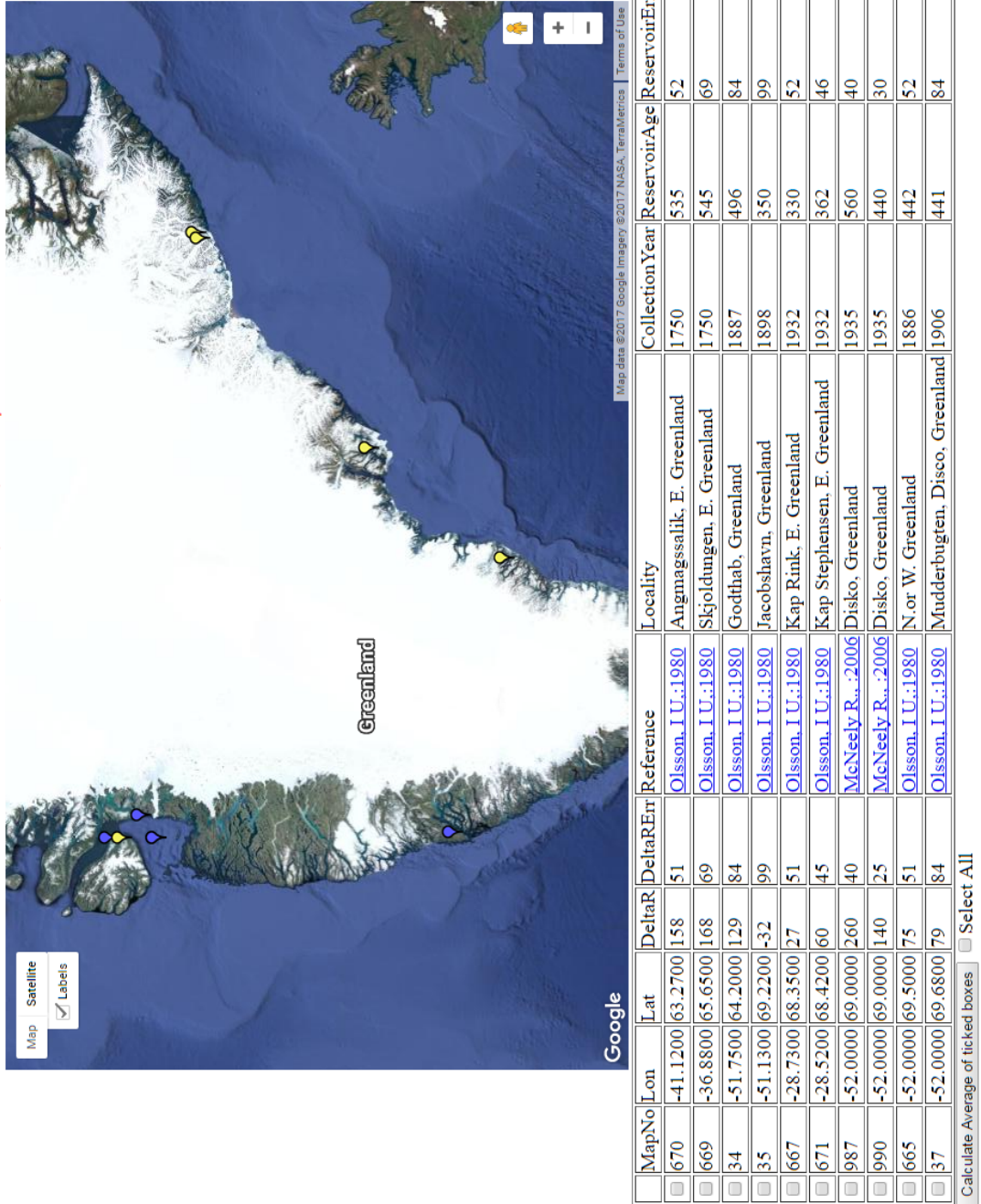


Figure B.2: Location of cores used for calculating the reservoir effect (delta R).